Topological and Unconventional States of Matter

Callum William Duncan

Submitted for the degree of Doctor of Philosophy

School of Engineering and Physical Sciences
Heriot-Watt University

August 2019

Abstract

Topology is the study of geometrical objects which are equivalent under continuous deformations. The concept of topology can be relevant to the physics of condensed matter systems. For example, a potentially significant phase of matter for future technologies is that of a topological insulator. Topological insulators have conducting edge modes but an insulating bulk due to the topology of the continuum energy bands. Topological edge states are not the only form of topology that can appear in a condensed matter setting. An alternative is for there to be linked or knotted structures in the properties of a system, for example in the form of the magnetic field lines or vortices.

We begin by considering one-dimensional non-interacting lattice models of condensed matter physics. We will derive their exact wave functions and use them to study the robustness of edge states in topological insulators against impurities. We will then consider a periodically driven two-dimensional model which exhibits edge states and investigate the robustness of the edge transport against interactions. For this model, we will discuss a classical limit, which is equivalent at special points to the quantum dynamics of the model.

We also consider the realisation of artificial linked and knotted magnetic fields for ultracold atoms. One of the usual techniques of realising synthetic magnetic fields, the Λ-scheme, is found to have an equivalent magnetic field to the natural geometrical construction of linked and knotted magnetic fields. Utilising the Λ-scheme we then propose a method of realising synthetic linked and knotted magnetic fields which involves driving internal atomic transitions by superposition of Laguerre-Gaussian modes.

Together, the three projects discussed in this thesis show the possible diversity of systems that exhibit physics due to their topology. Furthermore, the study of the formation and robustness of topological states of matter is essential for their possible future applications.

Disce pati (Learn to suffer)
Clan Duncan motto

Acknowledgements

First, I would like to thank my advisors during the last four years, Prof. Patrik Öhberg and Dr Manuel Valiente.

Prof. Patrik Öhberg deserves thanks for many things. Most importantly, for creating the research environment in which I have conducted my research career so far. His support and calming influence have been vital during the sometimes intense experience of doctoral studies.

Dr Manuel Valiente has been key to my development as a scientist. At the start of my PhD, I was a little overwhelmed and unsure of how to progress through academia and research. It was at this time that Manuel stepped in and helped me to develop as a scientist. I will forever be grateful to Manuel for his continuous guidance in both research and academic life. I am also indebted to Manuel for opening up his network of collaborators to myself, especially for introducing me to Prof. Nikolaj T. Zinner.

At this point, it only seems natural to thank all of my collaborators on all projects during my doctoral studies. I want to say a special thanks to Nikolaj and Prof. Adolfo del Campo. I want to thank Nikolaj for his kind invitations to host me at Aarhus on several occasions and for his constant willingness to collaborate. I am grateful to Adolfo for hosting me for three months at the University of Massachusetts Boston, in which time he introduced me to a variety of new topics which have been influential on my research direction ever since. I would also like to thank, in no particular order, Niels J. S. Loft, Dr Filipe F. Bellotti, Dr Kali E. Wilson, and Prof. Daniele Faccio.

During my three month trip to Boston, I was lucky enough to meet and become friends with Dr Luis Pedro García-Pintos, who made Boston feel like a second home. I also thank Luis Pedro for convincing me to open my eyes to some other topics in quantum physics.

The final chapter of this thesis is about linked and knotted magnetic fields. This project was in collaboration with Dr Calum Ross and Prof. Bernd J. Schroers. I want to thank them both for guiding the way on many of the more mathematical concepts of differential geometry and for instigating this collaboration.

I have been lucky enough to be part of the Scottish Doctoral Training Centre in Condensed Matter Physics, which has provided me with a stimulating environment in which to conduct my studies. They have also offered courses and workshops to help with skills development during my PhD. I would like to in particular thank Dr Chris Hooley, Prof. Ian Galbraith and, perhaps most importantly, all the secretaries from the doctoral training centre.

I want to thank my fellow PhD students at Heriot-Watt for their valuable dis-

cussions at various points in all projects. In particular, I would like to thank William Brown, Niclas Westerberg, Calum Maitland, Gerard Valent-Rojas and Dean Johnstone. I thank Dr Alexander Spracklen for his valuable guidance through the quantum band structures of the driven quantum model discussed in this thesis. Niclas and I have gone through most of the hurdles and milestones in our PhDs together, and I think it is fair to say, it is difficult to think of how these years would have progressed without this simple support network.

I want to take this chance to thank my Mum for the hard work and sacrifices in her life, which allowed me to reach this point. I want to thank my Dad for keeping me well-grounded and keeping many old cars on the road over the years. I would also like to thank my sister for our years of competition when growing up that built the foundations for my work ethic today.

Of course, I would not have reached this point without the support of my fantastic fiancée, Lyndsay McIntosh. In our wonderful almost 11 years together, Lyndsay has encouraged me to pursue lofty goals (including to attend university in the first place), supported me in all my decisions, and been at my side through all the good and bad times. Lyndsay has been continuously understanding and supportive of all aspects of working in academia. Lyndsay has also encouraged me to travel and build my network of collaborators even when it meant we spent long periods apart.

I think I can truthfully say that I did not have any crisis during my PhD, but not for lack of my effort to generate one. The lack of a crisis I think is entirely down to the influence of two people. On the academic side was Manuel, who was supportive and available to chat at all times, even when he was going through big moves himself. On the other hand, was Lyndsay, who was always there to put a smile on my face and ensure I relaxed, even when I refused to make those tasks simple.

As always, I am sure there will be someone I have missed out. To those I have missed, I can only apologise and acknowledge my ineffective memory and gratitude.

Financial support is acknowledged from EPSRC CM-CDT Grant No. EP/L015110/1 and SUPA under the Postdoctoral and Early Career Researcher Exchange Program.

ACADEMIC REGISTRY

Research Thesis Submission

Please note this form should be bound into the submitted thesis.

Name*:*			
School:			
Version: *(i.e. First, Resubmission, Final)*		Degree Sought:	

Declaration

In accordance with the appropriate regulations I hereby submit my thesis and I declare that:

1. The thesis embodies the results of my own work and has been composed by myself
2. Where appropriate, I have made acknowledgement of the work of others
3. Where the thesis contains published outputs under Regulation 6 (9.1.2) these are accompanied by a critical review which accurately describes my contribution to the research and, for multi-author outputs, a signed declaration indicating the contribution of each author (complete Inclusion of Published Works Form – see below)
4. The thesis is the correct version for submission and is the same version as any electronic versions submitted*.
5. My thesis for the award referred to, deposited in the Heriot-Watt University Library, should be made available for loan or photocopying and be available via the Institutional Repository, subject to such conditions as the Librarian may require
6. I understand that as a student of the University I am required to abide by the Regulations of the University and to conform to its discipline.
7. Inclusion of published outputs under Regulation 6 (9.1.2) shall not constitute plagiarism.
8. I confirm that the thesis has been verified against plagiarism via an approved plagiarism detection application e.g. Turnitin.

* *Please note that it is the responsibility of the candidate to ensure that the correct version of the thesis is submitted.*

Signature of Candidate*:*		Date:	

Submission

Submitted By *(name in capitals):*	
Signature of Individual Submitting:	
Date Submitted:	

For Completion in the Student Service Centre (SSC)

Received in the SSC by *(name in capitals):*			
Method of Submission *(Handed in to SSC; posted through internal/external mail):*			
*E-thesis Submitted (**mandatory for final theses**)*			
Signature:		Date:	

List of Publications

Publications contained in this thesis:

1. Callum W. Duncan, Patrik Öhberg and Manuel Valiente, *Driven topological systems in the classical limit*, Phys. Rev. B **95**, 125104 (2017)

2. Callum W. Duncan, Patrik Öhberg and Manuel Valiente, *Exact edge, bulk and bound states of finite topological systems*, Phys. Rev. B **97**, 195439 (2018)

3. Callum W. Duncan, Calum Ross, Niclas Westerberg, Manuel Valiente, Bernd J. Schroers and Patrik Öhberg, *Linked and knotted synthetic magnetic fields*, Phys. Rev. A **99**, 063613 (2019)

Additional publications and preprints:

1. Callum W. Duncan, Neils J. S. Loft, Patrik Öhberg, Nikolaj T. Zinner and Manuel Valiente, *Spin Localization of a Fermi Polaron in a Quasirandom Optical Lattice*, Few-Body Systems **58**, 50 (2017)

2. Callum W. Duncan, Filipe F. Bellotti, Patrik Öhberg, Nikolaj T. Zinner and Manuel Valiente, *Mobile spin impurity in an optical lattice*, New J. Phys. **19**, 075001 (2017)

3. Callum W. Duncan and Adolfo del Campo, *Shortcuts to Adiabaticity Assisted by Counterdiabatic Born-Oppenheimer Dynamics*, New J. Phys. **20**, 085003 (2018)

4. Kali E. Wilson, Niclas Westerberg, Manuel Valiente, Callum W. Duncan, Ewan M. Wright, Patrik Öhberg and Daniele Faccio, *Observation of photon droplets and their dynamics*, Phys. Rev. Lett. **121**, 133903 (2018)

5. Niclas Westerberg, Kali E. Wilson, Callum W. Duncan, Daniele Faccio, Ewan M. Wright, Patrik Öhberg and Manuel Valiente, *Self-bound droplets of light with orbital angular momentum*, Phys. Rev. A **98**, 053835 (2018)

6. Dean Johnstone, Patrik Öhberg and Callum W. Duncan, *Phase transitions of an ultracold gas in a quasicrystalline potential*, arXiv:1904.12870

7. Dean Johnstone, Niclas Westerberg, Callum W. Duncan and Patrik Öhberg, *Staggered Ground States in an Optical Lattice*, arXiv:1905.00027

Contents

Chapter 1

Introduction

After the observation of Bose-Einstein condensation in 1995 [1–3], the field of quantum gases has been growing rapidly. This growth has included the development of ultracold Fermi gases [4], dipolar gases [5, 6], and molecules [7, 8] as new platforms for quantum gases. An advantage of ultracold atoms is that they provide clean systems with a high degree of controllability [9–14], meaning they can be used to simulate models of condensed matter physics.

The first atomic Bose-Einstein condensates realised were in the regime of weak interactions [15], which was well studied in condensed matter physics well before the realisation of Bose-Einstein condensates [16]. However, the physics of ultracold gases was brought into the regime of strong correlations with the introduction of artificial periodic potentials known as optical lattices [17]. Optical lattices are generated by interfering laser beams which form periodic standing waves. When loaded into an optical lattice, the ultracold gas is described by the Bose-Hubbard model, which describes interacting bosons on a lattice including tunnelling and interaction terms. This regime allowed for the investigation of a quantum phase transition between the Mott-insulator phase (a gapped phase with an integer number of atoms per site) and the superfluid phase (a conducting phase with a constant density) [18]. This led to the eventual experimental observation of the superfluid to Mott-insulator transition in a bosonic atomic ensemble loaded into an optical lattice [19]. Cold atoms in optical lattices can also realise non-standard Bose-Hubbard models [20], including the introduction of long-range interactions. These non-standard Bose-Hubbard models have allowed new phases to be predicted and observed [21–28].

Ultracold atoms in optical lattices offer a high degree of control over the system [10]. It is possible to obtain a variety of lattice geometries by engineering the direction, polarisation, intensity and phase of the lasers realising the optical lattice. This variety includes the spatial dimension of the lattice, with three-, two-, and one-dimensional systems being possible [13, 29]. There is also a large amount of control over the interactions between the atoms in the optical lattice. For example, it is possible to tune on-site interactions via magnetic Feshbach resonances [30, 31], and

long-range interactions can be introduced by having atoms with a significant dipole moment, such as Chromium [5, 21, 32], or by having interactions mediated by an optical cavity (an arrangement of mirrors that form a standing wave) [33–36]. The tunnelling of the atoms between lattice sites can be controlled, with two methods being either a tilting of the optical lattice potential (an energy offset between lattice sites) [37] or laser assisted tunnelling [38, 39].

A current field of interest in ultracold atoms is that of topological states of matter. Topology is a mathematical concept that refers to properties of geometrical objects that are preserved under smooth deformations. Ultracold atoms are a useful platform for probing the physical consequences of topology. These consequences include the consideration of topological insulators (and their edge states) [40, 41] and the intricate topological objects of knots [42–52]. Topological insulators behave as regular insulators in their interior (or bulk) but have conducting states along their surfaces (or edges). The integer quantum Hall effect is an example of a topological insulator. In the integer quantum Hall effect there are conducting edge states that are exhibited by charged particles in the presence of a magnetic field [53, 54]. The overarching theme of this thesis is the concept of topology in ultracold atoms. I will consider three different scenarios of topology, static low-dimensional topological insulators, driven topological insulators, and topologically non-trivial magnetic fields.

The simulation of condensed matter, or quantum systems, in magnetic fields, has been a topic of interest in ultracold atoms for a couple of decades. In ultracold gases, synthetic magnetic fields are required to mimic the behaviour of charged particles in magnetic fields, as the atoms are neutrally charged [10, 55, 56]. In lattices, artificial magnetic fields can be induced by either laser-induced tunnelling [57, 58] or lattice shaking [59, 60], and have been realised experimentally [39, 61–64]. Artificial magnetic fields can also be realised for ultracold gases that are not confined in lattices. For a trapped ultracold gas in free space, synthetic magnetic fields can be realised by rapidly rotating the trap [65, 66] or by using light-matter coupling [67–75].

I will now briefly outline the layout of this thesis. The next chapter will serve as a background to the broad range of concepts utilised, including ultracold gases in optical lattices, periodically driven systems, and topology. In Chapter 3, we will construct the exact analytical states of one-dimensional (and certain two-dimensional) lattices that are described by non-interacting Hubbard models. These models can either be topological or topologically trivial, which in this case relates to the existence of edge states. We then use this exact analytical technique to study the robustness of edge states in topological models, which is an essential topic of study in topological insulators. In Chapter 4, we consider a periodically driven two-dimensional lattice that exhibits topological edge states in its dynamics. We introduce interactions into this system by considering the classical limit of both hardcore bosons and

spinless fermions. This system is studied for the case of both classical and quantum evolution, and the robustness of the edge states is investigated. In the final part of this thesis, Chapter 5, we will study a different form of topology appearing in an ultracold atomic gas. In this model, the topology is contained in the form of a magnetic field, which has linked or knotted magnetic field lines. We propose a method of realising these topologically non-trivial structures in the synthetic magnetic field 'felt' by an ultracold atomic gas. The proposed method of realisation has a link to the geometrical construction of topological magnetic fields, allowing for the implementation of linked and knotted synthetic magnetic field lines.

Chapter 2

Background

In this chapter, we will review useful concepts and definitions for the topics discussed in this thesis. As already mentioned, this thesis focuses on topological phases in ultracold gas systems in three different settings. To tackle each problem, we need a basic level of understanding of quantum mechanics, many-body physics, crystal lattices, and topology, including topological insulators, and links and knots.

2.1 Quantum mechanics

In this section, I review essential quantum-mechanical concepts to establish the notation used throughout this thesis. Here, I follow the working of standard textbooks in quantum mechanics, see Refs [16, 76–80] and we point the reader to these works for further details on the topics discussed here.

The mathematical formalism of quantum mechanics relies on there being a function $\Psi(q)$ which describes the state of the system at any given time, with q being the set of parameters describing the system. This function is known as the wave function. The square modulus of this function, $|\Psi(q)|^2$, represents a probability density, whose normalisation is therefore given by

$$\int dq |\Psi(q)|^2 = 1. \tag{2.1}$$

The wave function is only determined up to a constant global phase factor. This indeterminacy of the wave function is irremovable but does not impact the physics of the state.

A proposition of quantum mechanics is the principle of the superposition of states. If there are two possible wave functions, $\Psi_1(q)$ and $\Psi_2(q)$, which lead to two independent results, then any linear combination of these states, $c_1\Psi_1(q) + c_2\Psi_2(q)$, must also be a possible wave function.

The selection of states possible for a quantum mechanical system is contained within the Hilbert space, which is a complete complex vector space possessing the

structure of an inner product. The inner product is a scalar quantity defined for each pair of vectors, and allows for the length of a vector and angles between vectors to be defined. Two vectors in this space can be defined as orthogonal if they have zero inner product. The Hilbert space can be defined as either having a finite dimensionality or being composed of an infinite set of states. An orthogonal basis for the Hilbert space is a set of vectors which are each orthogonal to each other.

We will also work in the bra and ket vector notation of the wave function. In this notation, the wave function is a column vector $|\Psi\rangle$, and its conjugate transpose a row vector $\langle\Psi|$. The wave function in position representation is then given by

$$\Psi(q) = \langle q|\Psi\rangle. \tag{2.2}$$

In this notation, the normalisation condition is written as

$$\langle\Psi|\Psi\rangle = 1. \tag{2.3}$$

Any wave function can be written as a summation over an orthonormal basis set $|\phi_n\rangle$, i.e.

$$|\Psi\rangle = \sum_n c_n|\phi_n\rangle, \tag{2.4}$$

with $c_n = \langle\phi_n|\Psi\rangle$. If a system is described by a normalised wave function $|\Psi\rangle$ then the probability that the system is in any state $|\phi\rangle$ is denoted by

$$P(\Psi \mapsto \phi) = |\langle\phi|\Psi\rangle|^2. \tag{2.5}$$

The second postulate of quantum mechanics states that self-adjoint operators on the Hilbert space represent observable physical quantities. An operator is a mapping of the Hilbert space on itself.

The time evolution of the wave function is fully described by the time dependent Schrödinger equation

$$i\hbar\partial_t\Psi(\mathbf{r}, t) = \hat{H}\Psi(\mathbf{r}, t), \tag{2.6}$$

where ∂_t is the partial time derivative, and $\hat{H}$ is the systems Hamiltonian. Note, we have defined the parameters of the system as space $\mathbf{r}$ and time t, and the Hamiltonian is the energy operator of the system. In general, a many-body system of N particles without a magnetic field but with interactions has a Hamiltonian of the form

$$\hat{H} = \sum_n^N \frac{\hat{p}_n^2}{2m_n} + U(\mathbf{r}_1, \mathbf{r}_2, \ldots, \mathbf{r}_N), \tag{2.7}$$

where $\hat{p}_n = -i\hbar\nabla_n$ is the momentum operator for the nth particle, m_n the nth particle mass, and $U(\mathbf{r}_1, \mathbf{r}_2, \ldots, \mathbf{r}_N)$ contains the potential energy and interactions.

For a single particle or non-interacting system, the Hamiltonian is given by

$$\hat{H} = \frac{\hat{p}^2}{2m} + U(\mathbf{r}), \tag{2.8}$$

with $U(\mathbf{r})$ the potential energy of the particle in some external field. If we take the wave function to be separable in time and space coordinates,

$$\Psi(\mathbf{r}, t) = \psi(\mathbf{r})T(t), \tag{2.9}$$

then we obtain the time-independent Schrödinger equation

$$\hat{H}\psi(\mathbf{r}) = E\psi(\mathbf{r}), \tag{2.10}$$

with the full time-dependent solution

$$\Psi(\mathbf{r}, t) = \psi(\mathbf{r})e^{-iEt/\hbar}. \tag{2.11}$$

The solutions to the time-independent Schrödinger equation are the eigenstates of the system, $\psi(\mathbf{r})$, and the corresponding eigenenergies E.

In the quantum theory of many-body physics, there are two main types of particles, bosons and fermions. We will not discuss in this thesis the interesting physics of anyonic quasiparticles [81–85]. Bosons are defined via wave functions that are symmetric under particle exchange,

$$\Psi(\cdots, x_i, \cdots, x_j, \cdots) = \Psi(\cdots, x_j, \cdots, x_i, \cdots). \tag{2.12}$$

For fermions the wave function is antisymmetric under particle exchange,

$$\Psi(\cdots, x_i, \cdots, x_j, \cdots) = -\Psi(\cdots, x_j, \cdots, x_i, \cdots). \tag{2.13}$$

For bosons we can define operators $\hat{b}_k$ and $\hat{b}_k^\dagger$ which satisfy the commutation rules

$$\begin{aligned} \left[\hat{b}_k, \hat{b}_{k'}^\dagger\right] &= \delta_{k,k'}, \\ \left[\hat{b}_k, \hat{b}_{k'}\right] = \left[\hat{b}_k^\dagger, \hat{b}_{k'}^\dagger\right] &= 0, \end{aligned} \tag{2.14}$$

which define the properties of the operators

$$\begin{aligned} \hat{b}_k^\dagger \hat{b}_k |n_k\rangle &= n_k |n_k\rangle, \\ \hat{b}_k |n_k\rangle &= \sqrt{n_k}|n_k - 1\rangle, \\ \hat{b}_k^\dagger |n_k\rangle &= \sqrt{n_k + 1}|n_k + 1\rangle, \end{aligned} \tag{2.15}$$

with $|n_k\rangle$ being the number state of n particles in the kth eigenstate. We can therefore define $\hat{b}_k$ as the destruction operator, and $\hat{b}_k^\dagger$ as the creation operator. We

can describe a similar set of operators for fermions, which obey the anticommutation relations

$$\begin{aligned} \{\hat{c}_k, \hat{c}_{k'}^\dagger\} &= \delta_{k,k'}, \\ \{\hat{c}_k, \hat{c}_{k'}\} = \{\hat{c}_k^\dagger, \hat{c}_{k'}^\dagger\} &= 0, \end{aligned} \tag{2.16}$$

which define the operators

$$\begin{aligned} \hat{c}_k^\dagger \hat{c}_k |n_k\rangle &= n_k |n_k\rangle, \\ \hat{c}_k^\dagger \hat{c}_k^\dagger |0\rangle &= 0, \end{aligned} \tag{2.17}$$

and

$$\begin{aligned} \hat{c}_k|1\rangle = |0\rangle \quad & \hat{c}_k|0\rangle = 0, \\ \hat{c}_k^\dagger|1\rangle = 0 \quad & \hat{c}_k^\dagger|0\rangle = |1\rangle. \end{aligned} \tag{2.18}$$

Due to the statistics of the fermions defined from the anticommutation relations, the occupation of any state by more than one particle is prohibited.

To construct physical models of many-body quantum systems it is sometimes necessary to consider the Hamiltonian in terms of creation and annihilation field operators. The field operators are utilised for combining quantum mechanics with special relativity, as the usual creation and annihilation operators defined above are multiplied by a matrix with a momentum dependence upon a Lorentz transformation [86]. These field operators are defined as

$$\begin{aligned} \hat{\Psi}(\mathbf{r}) &= \sum_m \psi_m(\mathbf{r}) \hat{a}_m, \\ \hat{\Psi}^\dagger(\mathbf{r}) &= \sum_m \psi_m^*(\mathbf{r}) \hat{a}_m^\dagger, \end{aligned} \tag{2.19}$$

where $\hat{a}_m$ ($\hat{a}_m^\dagger$) are the creation (annihilation) operators of generic particles in mode m and the $\psi_m(\mathbf{r})$ being position dependent coefficients which are wave functions. The creation and annihilation operators considered previously are defined for particles with a specific position, whereas the field operators are defined over every point in space. For bosonic particles, the creation and annihilation operators in the field operators are given by the bosonic $\hat{b}_m$ and $\hat{b}_m^\dagger$ and follow the commutation relations

$$\begin{aligned} \left[\hat{\Psi}(\mathbf{r}), \hat{\Psi}^\dagger(\mathbf{r}')\right] &= \delta(\mathbf{r}, \mathbf{r}'), \\ \left[\hat{\Psi}(\mathbf{r}), \hat{\Psi}(\mathbf{r}')\right] = \left[\hat{\Psi}^\dagger(\mathbf{r}), \hat{\Psi}^\dagger(\mathbf{r}')\right] &= 0. \end{aligned} \tag{2.20}$$

2.2 Ultracold gases in optical lattices

We now move on to discuss the basic theory of ultracold gases. We will briefly review Bose gases in free space and then discuss the description of ultracold gases in optical lattices. In this section, we will follow Refs. [9, 10, 15] for the basic concepts of Bose gases and their description in optical lattices.

2.2.1 Theoretical description of a Bose gas

Bose-Einstein condensates are usually described by the theory of trapped dilute Bose gases. This dilute quantum gas has a far smaller density of particles ($\sim 10^{14}\text{cm}^{-3}$) compared to usual gases at room temperature ($\sim 10^{19}\text{cm}^{-3}$). The dilute nature of the gas allows the study of the weakly interacting regime [15]. Even if there is no external potential with interesting details, the Bose gas still needs to be trapped and will, therefore, be nonuniform.

The field operator of the Bose gas, $\hat{\Psi}(\mathbf{r}, t)$ will fulfil the equation

$$i\hbar\partial_t\hat{\Psi}(\mathbf{r},t) = \left[\frac{\hat{p}^2}{2m} + V_{\text{ext}}(\mathbf{r},t) + \int d\mathbf{r}'\hat{\Psi}^\dagger(\mathbf{r}',t)V(\mathbf{r}',\mathbf{r})\hat{\Psi}(\mathbf{r}',t)\right]\hat{\Psi}(\mathbf{r},t), \tag{2.21}$$

with V_{ext} giving an external single-particle potential, and $V(\mathbf{r}', \mathbf{r})$ denoting the two-body interaction. Note, that the two-body interaction here is considered to be a contact interaction, i.e. $V(\mathbf{r}', \mathbf{r}) \propto \delta(\mathbf{r}' - \mathbf{r})$.

The Bogoliubov prescription for the field operator implies that to the lowest-order approximation the operator $\hat{\Psi}(\mathbf{r}, t)$ can be replaced by a classical field $\psi(\mathbf{r}, t)$. This approximation is valid for an ultracold Bose gas as the temperatures are low and there are a large number of atoms present in the Bose-Einstein condensate state. While the field operator described all particles in the Bose gas, this classical field describes the behaviour of many particles. This approximation then gives the famed Gross-Pitaevskii equation [87, 88]

$$i\hbar\partial_t\psi(\mathbf{r},t) = \left[\frac{\hat{p}^2}{2m} + V_{\text{ext}}(\mathbf{r},t) + g|\psi(\mathbf{r},t)|^2\right]\psi(\mathbf{r},t), \tag{2.22}$$

with g being the interaction strength. This equation is the main workhorse for the theoretical description of ultracold weakly interacting Bose gases and must be solved in a self-consistent way.

2.2.2 Optical lattices

The interaction between an atom and an incident laser electric field under the dipole approximation is given by [11, 89, 90]

$$\hat{V}_d = -\mathbf{d}\cdot\mathbf{E}, \tag{2.23}$$

with $\mathbf{E}$ the electric field of the laser and $\mathbf{d}$ the dipole moment of the atom. Taking the electric field to be time-independent, the perturbative correction to the atoms ground state energy will be

$$\Delta = -\sum_e \frac{|\langle e|\hat{V}_d|g\rangle|^2}{\epsilon_e - \epsilon_g} \tag{2.24}$$

where the summation runs over the excited states e, g refers to the ground state, and $\epsilon_{g(e)}$ gives the respective energies of the unperturbed atom. We can write the electric field to be in the direction of the unit vector $\mathbf{u}$ so that $\mathbf{E} = E(\mathbf{r})\mathbf{u}$ and the perturbative correction is

$$\Delta = -\frac{1}{2}\alpha|E(\mathbf{r})|^2, \tag{2.25}$$

with the static polarizability of the atom defined as

$$\alpha = 2\sum_e \frac{|\langle e|\mathbf{d}\cdot\mathbf{u}|g\rangle|^2}{\epsilon_e - \epsilon_g}. \tag{2.26}$$

The perturbative correction to the ground state can be interpreted as a potential felt by the atom. Therefore, the atom effectively feels a potential of

$$V = -\frac{1}{2}\alpha|E(\mathbf{r})|^2. \tag{2.27}$$

If we consider the electric field to be produced by a pair of counter-propagating lasers, then the electric field is that of a standing wave in one dimension, and will be given by

$$E(x) = E_0\cos(kx), \tag{2.28}$$

with a strength of E_0 and $k = 2\pi/\lambda$ with λ the laser wavelength. The potential felt by the atom in this scenario will be given by

$$V_{\text{latt}} = -\frac{1}{2}\alpha E_0^2\cos^2(kx), \tag{2.29}$$

and is referred to as an optical lattice potential. By interfering more laser beams, it is possible to generate two- and three-dimensional lattices.

2.2.3 Bose-Hubbard model

The many-body Hamiltonian for an ultracold gas in second quantisation is

$$\begin{aligned}\hat{H} = &\int d\mathbf{r}\hat{\Psi}^\dagger(\mathbf{r})\left[-\frac{\hbar^2}{2m}\nabla^2 + V_{\text{ext}}(\mathbf{r})\right]\hat{\Psi}(\mathbf{r}) \\ &+\frac{1}{2}\int d\mathbf{r}d\mathbf{r}'\hat{\Psi}^\dagger(\mathbf{r})\hat{\Psi}^\dagger(\mathbf{r}')V(\mathbf{r},\mathbf{r}')\hat{\Psi}(\mathbf{r}')\hat{\Psi}(\mathbf{r}).\end{aligned} \tag{2.30}$$

We will consider the case of two-body interactions of contact-type, i.e.

$$V(\mathbf{r},\mathbf{r}') = g\delta(\mathbf{r}-\mathbf{r}'). \tag{2.31}$$

For a periodic external potential, e.g. that induced by two interfering lasers, the field operators may be written as discrete mode excitations via Bloch's theorem,

that are then given by

$$\begin{aligned}\hat{\Psi}(\mathbf{r}) &= \sum_{n,k} \psi_{n,k}(\mathbf{r})\hat{b}_{n,k}, \\ \hat{\Psi}^{\dagger}(\mathbf{r}) &= \sum_{n,k} \psi^{*}_{n,k}(\mathbf{r})\hat{b}^{\dagger}_{n,k},\end{aligned} \tag{2.32}$$

with n labelling the band and k the quasi-momentum. The state is then described in terms of the coefficients $\psi_{n,k}(\mathbf{r})$. In the tight-binding limit the delocalised $\psi_{n,k}(\mathbf{r})$ can be written in terms of a localised set of non-stationary states, which are called the Wannier functions. These Wannier functions are defined by

$$\psi_{n,k}(\mathbf{r}) = \sum_{\mathbf{R}} w_{n,\mathbf{R}}(\mathbf{r})e^{i\mathbf{k}\cdot\mathbf{R}}, \tag{2.33}$$

with $\mathbf{R}$ being the lattice translation vector and $w_{n,\mathbf{R}}(\mathbf{r})$ the Wannier functions. Note, this tight-binding limit is the same as that taken for electrons in a crystal lattice, where they are assumed to be closely associated with their corresponding ions [91, 92]. We can substitute the tight-binding limit into the discrete mode excitations from Bloch's theorem, Eq. (2.32), to obtain the field operators in terms of the Wannier functions as

$$\begin{aligned}\hat{\Psi}(\mathbf{r}) &= \sum_{n,\mathbf{R}} w_{n,\mathbf{R}}(\mathbf{r})\hat{b}_{n,\mathbf{R}}, \\ \hat{\Psi}^{\dagger}(\mathbf{r}) &= \sum_{n,\mathbf{R}} w^{*}_{n,\mathbf{R}}(\mathbf{r})\hat{b}^{\dagger}_{n,\mathbf{R}}.\end{aligned} \tag{2.34}$$

By inserting this form of the field operators into Hamiltonian (2.30), we can obtain the standard Bose-Hubbard model [17, 93]

$$\hat{H} = -\sum_{\langle i,j\rangle} J_{ij}\left(\hat{b}^{\dagger}_{i}\hat{b}_{j} + \hat{b}^{\dagger}_{j}\hat{b}_{i}\right) + \sum_{i}\frac{U_i}{2}\hat{n}_i(\hat{n}_i - 1) + \sum_{i}\epsilon_i\hat{n}_i, \tag{2.35}$$

where $\langle i,j\rangle$ denotes the summation over nearest-neighbours, $\hat{b}^{\dagger}_{i}$ ($\hat{b}_{i}$) creates (annihilates) an atom in the ith site, and $\hat{n}_i = \hat{b}^{\dagger}_{i}\hat{b}_{i}$ is the number operator. The limit of summing over only nearest-neighbours is valid as the Wannier functions decay exponentially [94] as a function of the distance between sites. Hence, the physics will be dominated by the nearest-neighbour terms. Each term of the standard Bose-Hubbard model has a physical interpretation; J_{ij} is the tunnelling between sites i and j, U_i the two-body on-site interaction, and ϵ_i the on-site energy due to the lattice structure. If the periodic potential has minima that are all equal, then ϵ_i will be constant across all lattice sites and will only contribute an energy offset. We will consider models in this thesis where ϵ_i can take an interesting structure and will dominate the physics of the states.

Each of the coefficients for the standard Bose-Hubbard Hamiltonian is defined in terms of an overlap integral of the corresponding Wannier functions and operator.

The tunnelling strength is given by

$$J_{ij} = \frac{\hbar^2}{2m} \int dr w_i^*(\mathbf{r}) \nabla^2 w_j(\mathbf{r}) - \int dr w_i^*(\mathbf{r}) w_j(\mathbf{r}) V_{ext}(\mathbf{r}), \tag{2.36}$$

the two-body on-site interaction strength by

$$U_i = g \int dr w_i^*(\mathbf{r}) w_i^*(\mathbf{r}) w_i(\mathbf{r}) w_i(\mathbf{r}) = g \int d\mathbf{r} |w_i(\mathbf{r})|^4, \tag{2.37}$$

and the on-site energy by

$$\epsilon_i = \int d\mathbf{r} |w_i(\mathbf{r})|^2 V_{\text{ext}}(\mathbf{r}) \approx V_{\text{ext}}(\mathbf{r}_i), \tag{2.38}$$

where $\mathbf{r}_i$ denotes the position of the ith lattice site. Above, we have defined $w_i(\mathbf{r})$ as the Wannier function centred on site i.

2.3 Periodic driving

Over the last decade, it has been shown that periodic driving can be a powerful technique in the manipulation and dynamics of many-body states [95]. This has included the realisation of artificial magnetic fields [59, 63, 64, 96, 97] and the investigation of topological band structures [98–104]. In this section, we will briefly review the fundamentals of Floquet theory which will appear in Chapter 4. In this section we will follow Refs. [95, 105].

A periodically driven model is described by a time-dependent Hamiltonian

$$\hat{H}(t) = \hat{H}(t+T), \tag{2.39}$$

and a time-dependent Schrödinger equation

$$i\hbar\partial_t \psi(t) = H(t)\psi(t). \tag{2.40}$$

Floquet theorem states that the solution to the time-dependent Schrödinger equation is given by

$$\psi(t) = \exp(-i\epsilon t/\hbar)\Phi(t), \tag{2.41}$$

with ϵ the quasienergies and $\Phi(t) = \Phi(t+T)$ a periodic function in time, known as the Floquet modes. By inserting Floquet's theorem into the time-dependent Schrödinger equation an eigenvalue equation can be obtained of the form

$$\left(H(t) - i\hbar\partial_t\right)\Phi(t) = \epsilon\Phi(t). \tag{2.42}$$

The time evolution of the state can be described by a unitary evolution operator

according to

$$\psi(t) = U(t, t_0)\psi(t_0), \tag{2.43}$$

with the unitary operator evolving the state from time t_0 to t. In general, the unitary evolution operator can be written as

$$U(t, t_0) = \mathcal{T} \exp\left(-\frac{i}{\hbar}\int_{t_0}^{t} dt' H(t')\right), \tag{2.44}$$

with $\mathcal{T}$ the time-ordering operator. We can derive an alternative eigenvalue equation using the unitary evolution operator. To do this, we start with the evolution of the state over one period

$$U(t + T, t)\psi(t) = \psi(t + T), \tag{2.45}$$

then insert Floquet's theorem and use the periodic nature of the Floquet modes to obtain the eigenvalue equation

$$U(t + T, t)\Phi(t) = \exp(-i\epsilon T/\hbar)\Phi(t). \tag{2.46}$$

Therefore, if we diagonalise the single period unitary evolution operator we can obtain the eigenenergies and the Floquet modes. This will be utilised in Chapter 4.

It is worth stopping here to consider the properties of the quasispectrum, as it has somewhat different properties from a standard spectrum. The main difference is that there is no energy conservation due to the time dependence of the problem. The eigenvalues are only defined up to an integer of the energy quantum $\hbar\omega$, with $\omega = 2\pi/T$. The eigenvalues then correspond to a quasienergy that does not exist on a linear space, but one that is defined as on a circle (it is periodic). The periodic nature of the quasienergy means that states that differ in energy by integer values of $\hbar\omega$ will be almost degenerate. These nearly degenerate states can cause heating issues in experiments that need to be suppressed [95, 106–108].

2.4 Topology

We will now briefly discuss the definition of topology and its manifestation in condensed matter and cold atom systems.

2.4.1 The concept of topology

Topology is concerned with the study of the properties and characteristics of space that are preserved under continuous deformations. Two spaces are said to be topologically equivalent if they can be mapped between each other by continuous transformations [109]. A space can have specific topological properties that are invariant upon transformation between topologically equivalent spaces [109, 110].

These properties are usually referred to as topological invariants.

An example of a topological invariant of a space is its connectedness. A space is called connected if a continuous path can connect any two points in the space. If a space is connected, then all topologically equivalent spaces will also be connected. All spaces can be separated into connected parts called connected components. If two points are in the same connected component, then they can be connected by a path. For each space, the number of connected components is a topological invariant [109].

The standard example of topology is that of a torus and a coffee mug, which are topologically equivalent shapes. However, the torus and coffee mug are not topologically equivalent to a sphere. It is possible to define a simple topological invariant for this example, the number of holes in the structure.

2.4.2 Topological insulators

Topological insulators are condensed matter systems which have bulk bands that cannot be continuously deformed into a trivial phase without the closing of the energy band gap [111]. A topological insulator has an energy gap between bulk bands, just like a standard insulator. A standard insulator is defined as a phase whereupon adiabatically turning off the tunnelling terms the phase will reproduce that of the atomic limit. However, in a topological insulator, there can be states in the energy gap which exist on the edge of the system. The term topological for the insulator refers to there being a bulk invariant that differentiates between phases of matter that possess the same symmetry. This bulk invariant can be the number of edge modes in the bulk band gap, i.e. changes in the bulk that preserve its topology will not change the number of edge modes.

The typical example of a topological insulator with an edge state is the integer quantum Hall effect [112–116]. In the quantum Hall effect, the Hall conductance and the number of edge states are invariant under continuous changes in the material parameters and can only change when the system goes through a phase transition which includes a closing of the band gap [117].

In this thesis, we are concerned with the study of non-interacting topological insulators, which are defined by a topological invariant of the bulk states [53, 111, 117]. The nature of topology in these phases of matter was first explained in Ref. [113].

2.4.3 Chern number

We can understand a two-dimensional band structure as the mapping between the crystal momentum $\mathbf{k}$ and the Bloch Hamiltonian $H(\mathbf{k})$. If there are a number of gaps in the band structure, then the equivalence classes of $H(\mathbf{k})$ can be continuously transformed between each other without closing any of the band gaps. An

equivalence class is defined as a subset of the form $\{x \in X : x\, R\, a\}$, with a being an element of X, and $x\, R\, y$ meaning there is an equivalence relation between x and y. These equivalence classes are distinguished by a topological invariant called the Chern number. The Chern number has its roots in the topic of differential geometry [109, 110]. However, in the context of topological insulators, it is perhaps easier understood in terms of the Berry phase [118–120].

The time evolution of a state, $|\psi_n(\mathbf{k}, t)\rangle$, when $\mathbf{k}$ is changed adiabatically over a path C will be given by

$$|\psi_n(\mathbf{k}, t)\rangle = \exp\left[-i\Theta(t)\right] |n(\mathbf{k}, t)\rangle \tag{2.47}$$

where

$$\Theta(t) = \frac{1}{\hbar}\int_0^t dt' E_n(\mathbf{k}, t') - i\int_C d\mathbf{k} \cdot \langle\psi_n(\mathbf{k}, t)|\nabla_{\mathbf{k}}\psi_n(\mathbf{k}, t)\rangle, \tag{2.48}$$

and

$$H|n(\mathbf{k}, t)\rangle = E_n(\mathbf{k}, t)|n(\mathbf{k}, t)\rangle. \tag{2.49}$$

The first term of the phase is the usual dynamical evolution and the second term is the Berry or geometrical phase. From this evolution we can define the Berry connection, which is analogous to a vector potential, to be

$$\mathbf{A}_n(\mathbf{k}) = i\langle\psi_n(\mathbf{k}, t)|\nabla_{\mathbf{k}}\psi_n(\mathbf{k}, t)\rangle, \tag{2.50}$$

and the corresponding Berry phase as

$$\gamma_n = \int_C \mathbf{A}_n(\mathbf{k}) \cdot d\mathbf{k}. \tag{2.51}$$

We can then use Stokes' theorem to write this integral over the path as a surface integral of a flux, i.e.

$$\int_C \mathbf{A}_n(\mathbf{k}) \cdot d\mathbf{k} = \int_S d\mathbf{S} \cdot \Big[\nabla_{\mathbf{k}} \times \mathbf{A}_n(\mathbf{k})\Big], \tag{2.52}$$

with the surface integral being over the Berry flux

$$\mathbf{F}_n(\mathbf{k}) = \nabla_{\mathbf{k}} \times \mathbf{A}_n(\mathbf{k}). \tag{2.53}$$

The Chern number is then defined as the total Berry flux in the Brillouin zone [111, 117, 120]

$$n_{\text{Chern}} = \frac{1}{2\pi}\int_S \mathbf{F}_n(\mathbf{k}) \cdot d\mathbf{S}, \tag{2.54}$$

and is known to be an integer quantity.

There is a simplistic picture to get a sense for the topological invariant nature of the Chern number by an analogy [121]. This analogous equation is Gauss' law

which is described by [122]

$$\frac{\varepsilon_0}{e}\int_S \mathbf{E}\cdot d\mathbf{S} = m, \tag{2.55}$$

where ε_0 is the permittivity, e the electric charge, and $m \in \mathbb{Z}$. Gauss' law tells us that the flux of an electric field through a closed surface is equal to the total charge inside that volume. The integral is independent of the shape of the surface or the configuration of the electrons as long as the number of electrons is conserved, and is, therefore, effectively a topological invariant. In our case, we do not have an electric field as the vector field inside the surface integral, but a field related to the structure of the eigenstate manifold. The Chern number then effectively counts the 'topological charge' within the surface, which will again be independent of the characteristics of the surface. The real picture of the integer nature of the Chern number involves a discussion that goes deeper into differential topology, including fibre bundles and twists of the space [109, 123, 124], which we will not discuss in this thesis.

So far, we have discussed the existence of edge states and the bulk topological invariant separately. However, the two can be linked by the bulk-boundary correspondence [117, 120]. In the quantum Hall effect, we have chiral edge states that can move either to the left or to the right, and in this system, the bulk-boundary correspondence is given by

$$N_R - N_L = \Delta n_{\text{Chern}}, \tag{2.56}$$

where N_R (N_L) is the number of right (left) moving states. So the difference of the number of right and left moving edge states in a band gap is equal to the difference of the Chern number across the interface. In general, the bulk-edge correspondence is established by relating the topological invariant to the number of edge states in the system. The bulk-edge correspondence is most easily shown by numerically testing the correspondence, i.e. calculating the Chern number and comparing this to the number of edge states. The bulk-edge correspondence can then only be shown to hold for individual models [116, 125–128]. The methods developed for topological insulators during this thesis directly avoid the bulk-edge correspondence, allowing the consideration of the introduction of impurities or interactions in topological insulators.

2.4.4 Zak phase

In this thesis, we will also consider one-dimensional models. In one dimension, the topological invariant is the Zak phase and is given by [120, 129, 130]

$$\mathcal{Z} = i\int dk \langle u_k|\partial_k u_k\rangle, \tag{2.57}$$

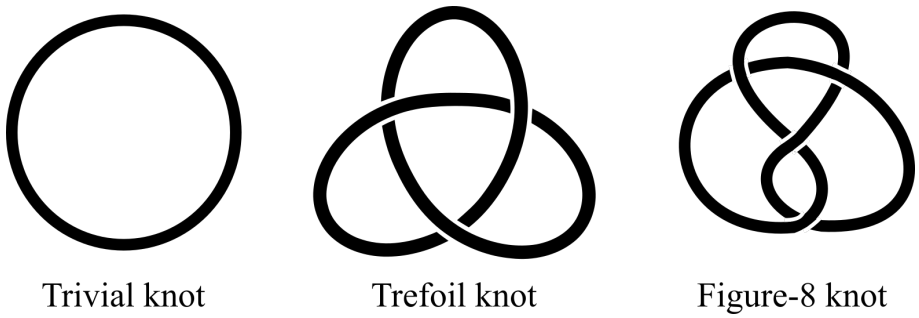

Figure 2.1: Illustrations of the three lowest order knots - the trivial, trefoil and figure-8 knots.

with the integral being over the first Brillouin zone and $|u_k\rangle$ denoting the Bloch wave functions. The Zak phase has a similar form to the Chern number, and the same arguments for the relation between the Chern number and the number of edge states can be extended to the Zak phase.

2.4.5 State robustness

One of the themes of this thesis is the robustness of topological states of matter. When we consider robustness we will be concerned with state robustness, i.e. the properties of the state under perturbations or the introduction of interactions. This means that we are not considering the robustness of the topological invariant and the application of the bulk-boundary correspondence. Instead, we are directly considering the properties of the topological state and its robustness under interactions and impurities. We are especially interested in impurities that do not preserve the symmetry of the system, which will be discussed in further detail in Chapter 3.

2.4.6 Links and knots

Another interesting form of topology is the presence of linked or knotted structures. In general, knot theory is the study of embedding circles in a space [131–133]. Knot theory in mathematics was in part inspired by Lord Kelvin's theory that all chemical properties of atoms are related to a knotting between the atoms [134]. At first, the concern of mathematicians was mainly in classifying knots up to a certain number of crossings [132, 135]. However, the topological nature of knots and their related links has been a vibrant field of mathematical study over the last 150 years [136–143].

In essence, a knot is a topological property of a closed string in three-dimensional space. We can write a stricter definition of a knot; a knot $K \subset \mathbb{R}^3$ is a subset of points homeomorphic to a circle [131]. We illustrate three of the simplest examples of knots in Fig. 2.1. The circle is the most trivial of structures that fits the definition of a knot, and it is usually referred to as the trivial knot. The simplest 'true' knot is the trefoil knot which has three crossings of the string and is then a knot of order

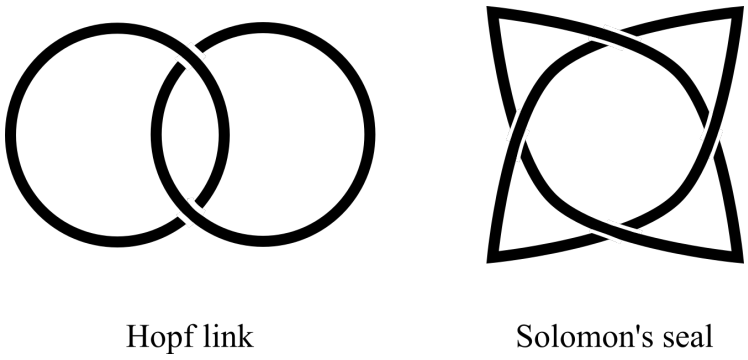

Figure 2.2: Illustrations of the two lowest order links - the Hopf link and Solomon's seal.

three. The next most complex knot is the figure-8 knot, which is of order four. Note, that while we have chosen to draw these knots as smooth curves this does not need to be the case, and it is possible to draw all three of these knots as polygons.

It is also possible to think of links if we allow there to be a collection of knots allowed in a three-dimensional space. We can write a more formal definition of a link; a link is a finite disjoint of the union of knots $L = K_1 \cup K_2$ [131]. The labelling of the topological order of links is a little more complicated than that of knots, as we also need to count the number of knots, referred to as components. We illustrate two simple examples of links in Fig. 2.2 with the Hopf link and Solomon's seal. Note, that both examples have two components, but they have different topological order, with two and four crossings respectively of the components.

Non-trivial topological structures, like knots and links, have been studied from a physics perspective in classical fluids [144–148], nuclear physics [149, 150], plasma physics [151–153], solid state systems [154], soft matter [155], biological applications (e.g. DNA) [156, 157], and in the electromagnetic field of light [158–161]. Linked and knotted structures can also form in the field lines of a topologically non-trivial magnetic field. Topological magnetic fields are an area of growing research interest with work on the mathematical construction of such fields [162] and on the stability of the field lines [146, 148, 163]. We will consider the realisation of synthetic topologically non-trivial magnetic fields in an ultracold atomic gas in Chapter 5.

Chapter 3

Analytical solutions of finite lattice models

Tight-binding lattice models are an essential theoretical framework for the study of condensed matter systems. Work in recent decades has mainly focused on the analytical form of edge states of topological tight-binding models in semi-infinite systems. For example, the edge states of the Harper and Hofstadter models were investigated by Hatsugai [116] via a transfer matrix approach and by Hügel and Paredes [164] by extending the bound state approach of Ref. [90]. These two methods only work if the lattice is semi-infinite or the periodicity of the lattice is commensurate with the size of the system. There has also been work on exact helical edge states from an ansatz in the quantum Hall and Bernevig-Hughes-Zhang models [165–167], under similar conditions of commensurability and boundary conditions. Analytical topological states have also been studied in models of stacked layers of lattices, including for the one-dimensional limit, by taking a fit for the decay of the edge states [168, 169]. To solve for all states of finite lattices with arbitrary parameters of general (aperiodic or periodic) size has so far required numerical exact diagonalisation.

The majority of states of a finite lattice are contained in the bulk continuum bands of the model. These bulk states do not have the localisation properties of the topological edge states and are generally extended across the full lattice. The analytical form of these states, outside of the cases of infinite size or periodic boundaries, has received little attention and to the best knowledge of the author, there are no previous works focused on their exact analytical form. One reason to consider the analytical form of these states is that it allows the labelling of the states with their corresponding quantum number, the quasi-momentum. Whereas, when solving the problem numerically by exact diagonalisation, the quantum numbers of the states can only be assigned according to an ordering of the energy levels. The knowledge of the analytical form for all states of the lattice (bulk and topological) could also be useful in the calculation of interaction matrix elements and for dealing with lattices of large size as we will discuss at the end of this chapter.

This chapter begins with a definition of the general model we will consider. We then derive the exact bulk states in Sec. 3.2 and the exact edge states in Sec. 3.3. The case of inhomogeneous lattices, with an impurity, is then studied in detail in Sec. 3.4. We finish this chapter by considering a quench of the lattice by an impurity and the robustness of edge states against this quench.

3.1 General model

The general model that we will construct exact analytical solutions to is a one-dimensional single-particle tight-binding model. This general Hamiltonian has the form

$$H = \sum_x \left(J_{x+1,x}\left(\xi_1, \tau_1\right) \hat{c}_x^\dagger \hat{c}_{x+1} + \text{H.c.} \right) + \sum_x V_x\left(\xi_2, \tau_2\right) \hat{c}_x^\dagger \hat{c}_x, \tag{3.1}$$

with $\hat{c}_x$ ($\hat{c}_x^\dagger$) being the annihilation (creation) operators of a particle at site x, we have set the lattice spacing to unity and we will take $x = x_0+1, \ldots, L_s-1$ as labels of the lattice site positions with open boundary conditions ($\psi(x_0) = \psi(L_s) = 0$, where $\psi(x)$ is the wave function). We can consider the tunnelling J and on-site potential V as having two different periodicities, τ_1 and τ_2 respectively, with the largest of these being proportional to the smallest, to give the overall periodicity τ. Note, that if this condition on periodicity is not met, then the periods are incommensurate, in this case, the procedure and solutions described in this chapter are still valid, but the periodicity will be equal to the lattice length, i.e. $\tau = L_s - x_0$. The strengths of the tunnelling and potential are denoted by ξ_1 and ξ_2 respectively, and we denote the set of the strengths as $\xi = \{\xi_1, \xi_2\}$.

The Hamiltonian of the system is considered to be time-independent and to follow the time-independent Schrödinger equation of

$$H\left(\xi, \tau\right) |\psi_{\sigma,k}\rangle = \epsilon_\sigma\left(k\right) |\psi_{\sigma,k}\rangle, \tag{3.2}$$

with the eigenenergies $\epsilon_\sigma\left(k\right)$ of the σ Bloch band ($\sigma = 1, \ldots, \tau$), quasi-momentum $k \in (-\pi/\tau, \pi/\tau]$ and eigenstates $|\psi_{\sigma,k}\rangle$, labelled by the quantum number k and σ. In the majority of this chapter we will work in the more convenient position representation, with

$$|\psi_{\sigma,k}\rangle = \sum_{x=x_0+1}^{L_s-1} \psi_{\sigma,k}(x) c_x^\dagger |0\rangle, \tag{3.3}$$

where $|0\rangle$ is the vacuum state and $\psi(x)$ is the position representation of the wave function in the xth lattice site. The probability of occupation in each lattice site is then defined through $|\psi(x)|^2$ and the wavefunction is characterised by $\psi(x)$. Note, that the eigenenergies satisfy $\epsilon_\sigma(k) = \epsilon_\sigma(-k)$. The time-independent Schrödinger equation can be recast in terms of the position representation to give a difference

equation of

$$J_{x,x-1}\psi_{\sigma,k}(x-1) + J^*_{x+1,x}\psi_{\sigma,k}(x+1) + V_x\psi_{\sigma,k}(x) = \epsilon_\sigma(k)\psi_{\sigma,k}(x). \tag{3.4}$$

In Sec. 3.4.3, we will consider a two-dimensional model which is reducible to a problem described by a one-dimensional Hamiltonian of the form of Eq. (3.1). This example considers the Hofstadter model on a square lattice. However, other geometries are possible to reduce to one-dimensional Hamiltonians. An example is graphene's non-interacting tight-binding Hamiltonian, which can be reduced to one dimension but with multiple sublattices [170]. The reduced model of graphene has been used to obtain the Zak phase for the model, which is a topological invariant defined in one dimension [130].

We will refer to commensurate and incommensurate lattices throughout this chapter. There are multiple definitions of the concept of a commensurate lattice. We will consider a commensurate lattice to be one where $L_s - x_0 = n\tau$, with $n \in \mathbb{Z}$. All other lattice sizes are incommensurate with the lattice period.

3.2 Bulk states

First of all, it will be useful to explain the definition of a bulk state. We will define a bulk state to be a state that has an eigenenergy which is within the infinite-size continuum energy bands. This definition means that the quasi-momentum can label the bulk states, $k \in (-\pi/\tau, \pi/\tau]$. We will discuss the other case, of quasi-momenta which do not satisfy this bound in Sec. 3.3.

The bulk solutions of Schrödinger equation (3.2) in the infinite-size limit are well known, and are of the form

$$\psi_{\sigma,k}(x) = e^{ikx}\phi_{\sigma,k}(x), \tag{3.5}$$

with $\phi_{\sigma,k}(x)$ being the Bloch functions which satisfy $\phi_{\sigma,k}(x+\tau) = \phi_{\sigma,k}(x)$. Given the exact form of the Hamiltonian, the Bloch functions can be obtained by utilising their periodicity. When deriving the Bloch functions, it is always possible to set their value at a single point, as they are only defined up to an overall normalisation constant. The infinite-size continuum bulk bands are also obtained at the same time as all the Bloch functions. It is worth stating for clarity that for any periodic lattice there are τ separate Bloch functions for each k and there are at most τ bulk bands.

It is from the infinite-size solutions that we can construct the finite size wave functions. To construct the finite size solutions we need to utilise the symmetry of the spectrum of our general model, i.e. $\epsilon_\sigma(k) = \epsilon_\sigma(-k)$. Due to this property, we can superpose $|\psi_{\sigma,k}\rangle$ and $|\psi_{\sigma,-k}\rangle$ to form a new state, which will have a wave

function of form

$$\psi_{\sigma,k}(x) = C_+\phi_{\sigma,+k}(x)\, e^{ikx} + C_-\phi_{\sigma,-k}(x)\, e^{-ikx}, \tag{3.6}$$

with $C_\pm$ being coefficients which will be obtained from the boundary conditions. This superposition of the $+k$ and $-k$ Bloch theorem solutions is, of course, itself an eigenstate of the Schrödinger equation of Eq. (3.4). We use the boundary condition of $\psi_{\sigma,k}(L_s) = 0$ to obtain the relation between C_+ and C_- as

$$\frac{C_+}{C_-} = -\frac{\phi_{\sigma,-k}(L_s)}{\phi_{\sigma,+k}(L_s)} e^{-2ikL_s}. \tag{3.7}$$

This allows us to write the un-normalised wave functions as

$$\psi_{\sigma,k}(x) = \phi_{\sigma,+k}(x)\, e^{ikx} - \frac{\phi_{\sigma,+k}(L_s)}{\phi_{\sigma,-k}(L_s)}\phi_{\sigma,-k}(x)\, e^{-ik(x-2L_s)}, \tag{3.8}$$

where the coefficient of the second term is now the ratio of the Bloch functions at the site L_s.

The quasi-momentum, k, of the exact states can now be calculated by means of the other boundary condition. By applying the boundary condition $\psi_{\sigma,k}(x_0) = 0$ to Eq. (3.8) we obtain the quantisation condition of

$$e^{2ik(x_0-L_s)} = \frac{\phi_{\sigma,+k}(L_s)\,\phi_{\sigma,-k}(x_0)}{\phi_{\sigma,+k}(x_0)\,\phi_{\sigma,-k}(L_s)}. \tag{3.9}$$

For the case of commensurate systems, $L_s = x_0 + m\tau$, with $m \in \mathbb{Z}$, the Bloch functions at x_0 and L_s are equal, and we obtain the condition for the quasi-momentum of

$$e^{2ik(x_0-L_s)} = 1, \tag{3.10}$$

which is solved by

$$k = \frac{n\pi}{m\tau}, \tag{3.11}$$

with $n \in \mathbb{Z}$ and the usual condition of $k \in (-\pi/\tau, \pi/\tau]$ satisfied.

3.2.1 Two-band model

Before discussing edge states and topologically non-trivial Hamiltonians, it is worthwhile to present a simple non-topological model. As an example, we will consider the standard ionic Hubbard model with a Hamiltonian

$$H = J\sum_x \left(\hat{c}_x^\dagger \hat{c}_{x+1} + \text{H.c.}\right) + \sum_x V_x \hat{c}_x^\dagger \hat{c}_x, \tag{3.12}$$

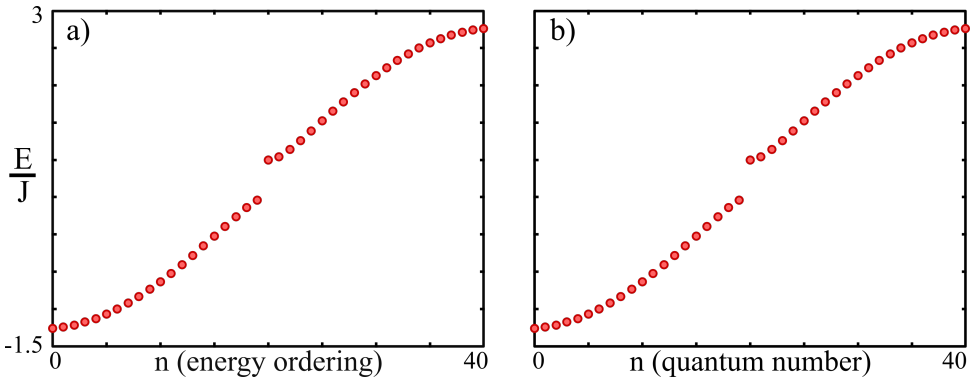

Figure 3.1: Energy spectrum of the two-band model with $u/J = 1$, $v/J = 0.5$ and $L_s = 41$. a) Spectrum from exact diagonalisation. b) Spectrum from exact analytical states.

with the tunnelling J a constant and the on-site potential

$$V_x = \begin{cases} u & \text{if } x \text{ is even} \\ v & \text{if } x \text{ is odd} \end{cases}. \tag{3.13}$$

By writing the Schrödinger equation of the form of Eq. (3.4) and using the infinite size ansatz, Eq. (3.5), it is straight-forward to obtain the bulk energy spectrum

$$E_s = \frac{1}{2}\left(u + v + (-1)^s \sqrt{8J^2 + (u-v)^2 + 8J^2\cos(2k)}\right), \tag{3.14}$$

which in the $u, v \to 0$ limit has the familiar form of $E = 2J\cos(k)$ corresponding to a homogeneous tight-binding lattice. We have labelled the bands $s = 0, 1$. The Bloch functions are two-periodic and are given by

$$\phi_s(x) = \begin{pmatrix} 1 \\ \frac{2J\cos(k)}{E_s - v} \end{pmatrix}, \tag{3.15}$$

for the s bands. To allow for a quick example, we can take the commensurate case ($x_0 = -1$ and $L_s = m\tau - 1$, $m \in \mathbb{Z}$), where the allowed quasi-momentum are given by

$$k = \frac{n\pi}{m\tau}, \tag{3.16}$$

with $n \in \mathbb{Z}$. The exact wave functions are then

$$\psi_k(x) = \phi_s(x)\, e^{ikx} - \phi_s(x)\, e^{-ik(x-2L_s)}, \tag{3.17}$$

due to the $k \to -k$ symmetry of the Bloch functions, and with s representing the band index.

We begin by looking at the spectrum of the two-band model from the quantisa-

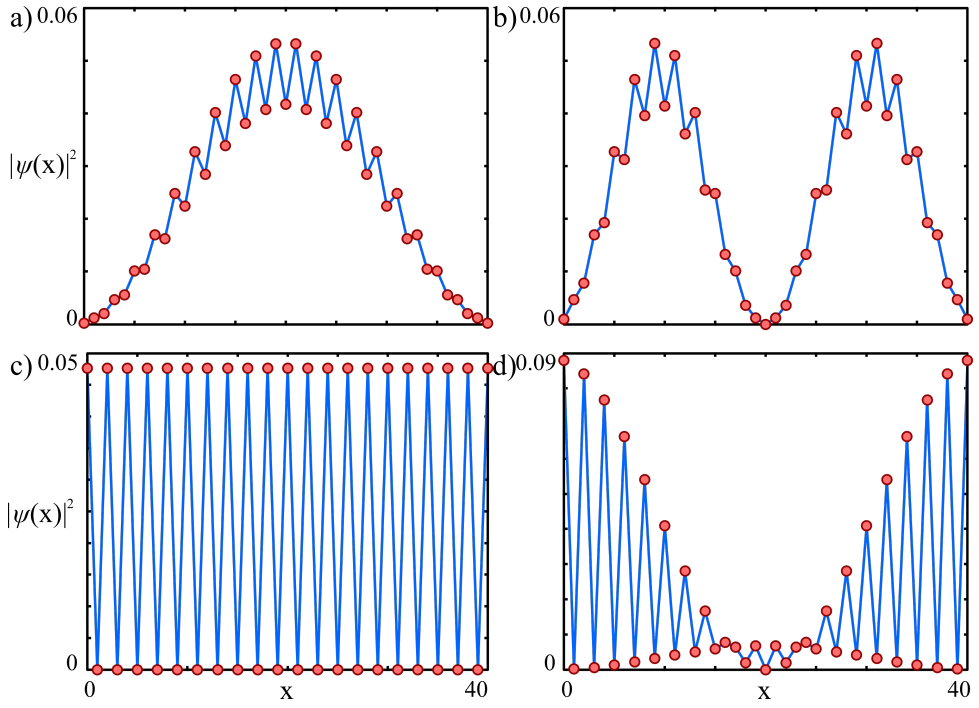

Figure 3.2: Probability densities of the states for the two-band model with $u/J = 1$, $v/J = 0.5$ and $L_s = 41$. a) $n = 1$, b) $n = 2$, c) $n = 21$ and d) $n = 22$. Circles (red) denote the exact analytical wavefunctions and solid lines (blue) connect points obtained via numerical exact diagonalisation.

tion and energy derived above to that obtained from numerical exact diagonalisation. These spectra, for $u/J = 1$, $v/J = 0.5$ and $L_s = 41$, are plotted side by side in Fig. 3.1, and it can be seen that there is an exact agreement between the results. We also consider some example wavefunctions in Fig. 3.2, where we observe an exact correspondence between the numerical exact diagonalisation and the exact wave functions of Eq. (3.17). This example serves to visualise that the exact analytical bulk states we have constructed are correct.

3.3 Edge or topological states

While bulk modes are intriguing and deserve attention, this method is in no way limited to only the consideration of states that have energies inside the bulk band. We will now consider the case of 'non-bulk' states, which have energies outside the continuum bands. In one-dimensional single-particle systems, this 'non-bulk' state will typically be in the form of an edge state. Each state outside the bulk band being an edge state is not the case for systems with impurities, where a state outside the bulk continuum bands can be bound to the impurity. We will focus on edge states, which can also be called topological states as their presence in the spectrum is due to the topological properties of the bulk bands.

When an edge state exists in a system, it is formally no different to any other

usual bound state. In the semi-infinite case, a general bound state of Hamiltonian (3.1) will have a wave function of the form

$$\psi(x) = \phi(x)\,\alpha^x, \tag{3.18}$$

where $0 < |\alpha| < 1$ for the case of $L_s \to \infty$ or $|\alpha| > 1$ for the case of $x_0 \to -\infty$. To find the Bloch functions, the ansatz of Eq. (3.18) can be placed in the Schrödinger equation and the periodic boundary condition of the Bloch functions utilised, i.e. $\phi(x) = \phi(x+\tau)$. The Bloch functions are then derived as functions of α instead of the usual k. The coefficient defining the bound states, α, is allowed to be real or complex, but, of course, its corresponding energy is required to be real as the systems we will consider are always Hermitian. The bound state of Eq. (3.18) is formally no different to the semi-infinite bulk state ansatz

$$\psi(x) = \phi(x)\,e^{ikx}, \tag{3.19}$$

if we allow k to be complex. Allowing k to be complex is equivalent to stating that the bound state can be a decaying solution of the bulk state ansatz, which is not surprising as the edge states are, by definition, localised states and for the energy to lie outside the bulk the quasi-momentum is required to be complex.

We will consider the form of states in finite lattices, where both limits of α in the semi-infinite case are normalizable. As in the case of the bulk states, we can then write the wave function in terms of a 'k' state and a '$-k$' state. Hence, as long as the energy has the $\alpha \to 1/\alpha$ symmetry, then the general bound edge state wave function in a finite system can be written as

$$\psi(x) = A_+\phi_+(x)\,\alpha^x + A_-\phi_-(x)\,\alpha^{-x}, \tag{3.20}$$

with $A_\pm$ denoting the coefficients to be determined by the boundary conditions. The notation of the Bloch function sub-indices now corresponds to the sign of the exponent of α, i.e. $+(-)$ corresponds to $\alpha^x\,(\alpha^{-x})$. By using the boundary condition $\psi(L_s) = 0$, we can obtain the form of the coefficients $A_\pm$ and the un-normalised exact wave functions as

$$\psi(x) = \phi_+(x)\,\alpha^x - \frac{\phi_+(L_s)}{\phi_-(L_s)}\phi_-(x)\,\alpha^{2L_s-x}. \tag{3.21}$$

3.3.1 Su-Schrieffer-Heeger model

Having defined the exact analytical wave functions for both bulk and edge states, we can now tackle a topological model. We will start by considering the paradigmatic example of the Su-Schrieffer-Heeger (SSH) model. The SSH model was introduced in 1979 as a model of polyacetylene [171]. In the decades since, the SSH model has

become an important example of a topological insulator, featuring in many works [172–177], including an experimental observation of the topological state by Meier *et al.* [178].

The SSH model is a limit of both the Rice-Mele [179] and Harper [180] models, and the Hamiltonian is commonly written in a unit-cell form as [120]

$$H = v \sum_{m=1}^{N} \left(|m, B\rangle\langle m, A| + \text{h.c.} \right) + w \sum_{m=1}^{N-1} \left(|m+1, A\rangle\langle m, B| + \text{h.c.} \right), \tag{3.22}$$

with m denoting the number of the unit cell, the chain consisting of N unit cells, and the state $|m, A(B)\rangle$ denoting the occupation of the $A(B)$ site of the mth unit cell of the lattice. The SSH model has a staggering of the tunnelling which in the above Hamiltonian is given by an intra-unit-cell tunnelling v and inter-unit-cell tunnelling w. The unit-cell form of the Hamiltonian is useful for the normal use of the Hamiltonian in lattice problems, to find the Bloch functions and energy. However, this form of the Hamiltonian does not lend itself well to lattice sizes that are not an integer number of unit cells.

We will write the SSH Hamiltonian in a different form, which is more fitting with the usual definitions of Harper Hamiltonians. We take the SSH Hamiltonian to be

$$H = \sum_{x} \left(J_{x,x+1} \hat{c}_x^\dagger \hat{c}_{x+1} + \text{h.c.} \right), \tag{3.23}$$

where we have placed all periodicity of the Hamiltonian into the tunnelling coefficient which has the form

$$J_{x,x+1} = J - \Lambda \left(-1\right)^x, \tag{3.24}$$

with J being the regular tunnelling strength and Λ the deviation between neighbouring terms. We will write the tunnelling coefficient as

$$J_{x,x+1} = 1 - \lambda \left(-1\right)^x, \tag{3.25}$$

with $\lambda = \Lambda/J$ denoting a dimensionless strength. In reference to the SSH Hamiltonian in the unit-cell notation, the tunnelling strengths are related as $v = 1 - \lambda$ and $w = 1 + \lambda$.

The topological invariant of one-dimensional tight-binding models is the Zak phase, as defined in Sec. 2.4.4. In our notation, the SSH model is topological if $\lambda > 0$ (with a non-zero Zak phase of the bulk bands) and topologically trivial with no edge state for $\lambda < 0$. For the topological invariant, the Zak phase of the Bloch bands is π for $\lambda > 0$ and zero for $\lambda < 0$. This difference in the topological invariant has been measured experimentally using ultracold atoms in optical lattices [181]. However, the number of edge states, i.e. the validity of the bulk-edge correspondence, is dependent on whether the lattice size is an integer number of unit cells or not. We

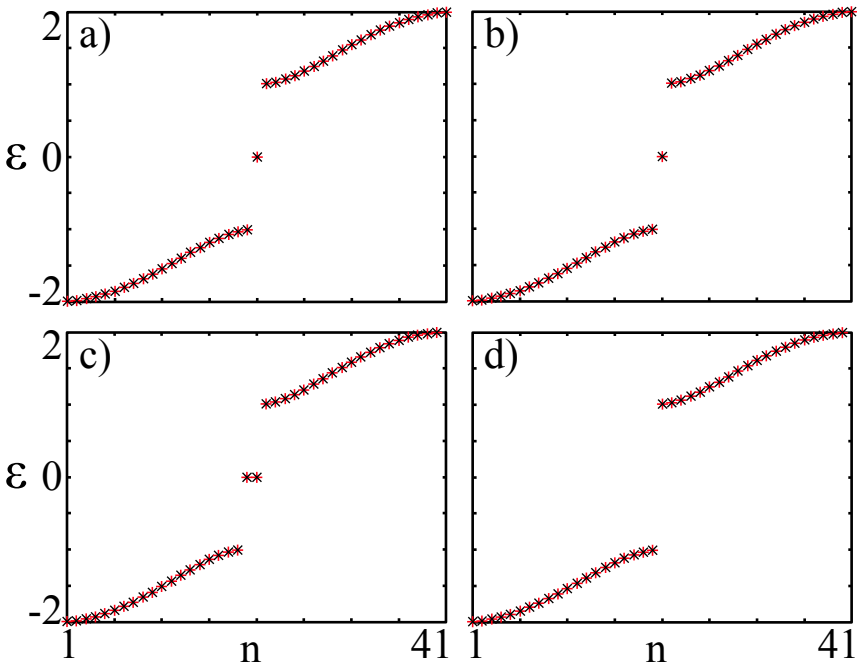

Figure 3.3: Energy spectra of the SSH model with a) $L_s = 41$ and $\lambda = 0.5$, b) $L_s = 41$ and $\lambda = -0.5$, c) $L_s = 40$ and $\lambda = 0.5$, and d) $L_s = 40$ and $\lambda = -0.5$. Numerical exact diagonalisation is given by plus signs (red) and the exact analytical results by crosses (black). Note, that the numerical and exact results are directly on top of each other.

will see this at play in the spectra of the SSH model in this section.

We can write the Schrödinger equation for this system, utilising Eq. (3.4), as

$$\left[1 - \lambda\left(-1\right)^{x-1}\right]\psi\left(x-1\right) + \left[1 - \lambda\left(-1\right)^{x}\right]\psi\left(x+1\right) = \varepsilon\psi\left(x\right), \tag{3.26}$$

with ε the dimensionless energy. Using the semi-infinite size limit, we can solve for the Bloch states and energies of the bulk and bound state ansatz, Eqs. (3.5) and (3.18). The bulk Bloch functions are

$$\phi_{s,\pm k}\left(x\right) = \begin{pmatrix} 1 \\ \frac{(1-\lambda)e^{\mp ik} + (1+\lambda)e^{\pm ik}}{\varepsilon_s} \end{pmatrix}, \tag{3.27}$$

with $s = 0, 1$ labelling the two bands of the spectrum given by

$$\varepsilon_s = \left(-1\right)^s \sqrt{\left(2\cos k\right)^2 + \left(2\lambda \sin k\right)^2}. \tag{3.28}$$

The bound state Bloch functions are found to be

$$\phi_{s,\pm}\left(x\right) = \begin{pmatrix} 1 \\ \frac{\left(1+\alpha^{\pm 2}\right) - \lambda\left(1-\alpha^{\pm 2}\right)}{\epsilon_s \alpha^{\pm 1}} \end{pmatrix}, \tag{3.29}$$

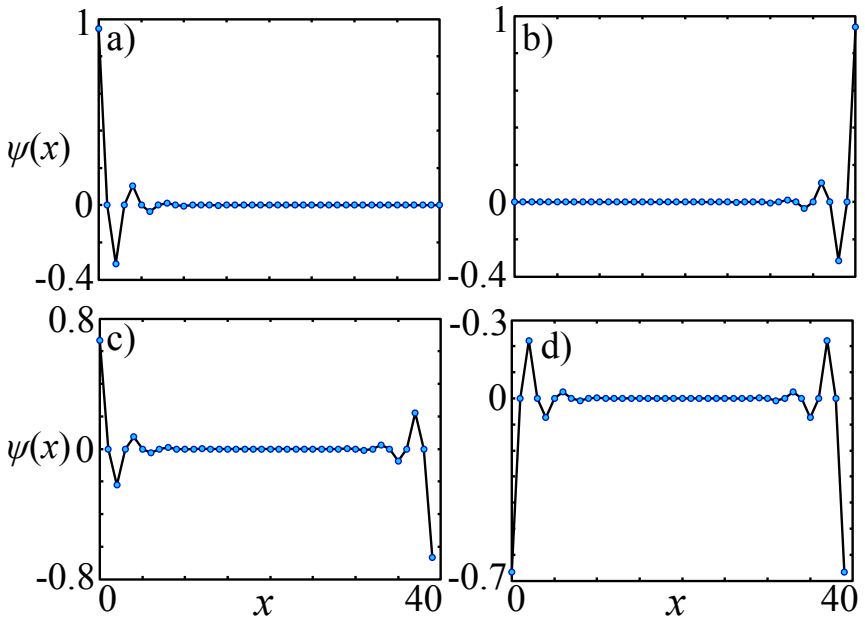

Figure 3.4: Edge or bound states of the SSH model with a) $L_s = 41$ and $\lambda = 0.5$ for state $n = 21$, b) $L_s = 41$ and $\lambda = -0.5$ for state $n = 21$, c) $L_s = 40$ and $\lambda = 0.5$ for state $n = 20$, and d) $L_s = 40$ and $\lambda = -0.5$ for state $n = 21$. The exact technique points are shown as (blue) circles and there is a solid (black) guide line between the points of numerical exact diagonalisation.

with a spectrum of form

$$\varepsilon_s = (-1)^s \sqrt{\left(\frac{1+\alpha^2}{\alpha}\right)^2 - \left(\lambda\frac{\alpha^2-1}{\alpha}\right)^2}. \tag{3.30}$$

We can now consider some examples. We will use the equation from the boundary conditions, Eq. (3.9), to define the bulk solutions. To obtain the bound state solution we consider the Schrödinger equation of Eq. (3.26) at $x = 0$, which is

$$\varepsilon_s = (1-\lambda)\frac{\psi(x+1)}{\psi(x)}. \tag{3.31}$$

This can be solved for α, using the exact analytical form of the state given in Eq. (3.21). By solving for α, we obtain all solutions, bulk and edge, for any set of parameters. The spectra for commensurate and incommensurate cases and both $\lambda < 0$ and $\lambda > 0$ are shown in Fig. 3.3. The bound edge states are shown in Fig. 3.4, this model has real eigenstates, allowing the straightforward display of the wave function instead of the probability densities. Note, throughout this chapter, we will consider relatively small system sizes to allow for the simple visualisation of the energies and the states. However, the method developed in this chapter works equally well for large system sizes.

For the incommensurate case of $L_s = 40$, we observe what is expected from previous studies [120], with a topological model for $\lambda > 0$, with two bound states in

the middle of the band gap, and a non-topological model for $\lambda < 0$ with all states in the bulk bands. The two edge states are not actually of the form of Eq. (3.21), as the two states have hybridised. The separate edge states are given by $\psi(x)$, as defined in Eq. (3.21), and $\psi(L_s - 1 - x)$ its spatial inverse. The hybridisation are given by the normalised symmetric, $\psi(x)+\psi(L_s-1-x)$, and antisymmetric, $\psi(x)-\psi(L_s - 1 - x)$, combinations of the eigenfunctions. It is these antisymmetric and symmetric wavefunctions which are compared to the numerical exact diagonalisation eigenstates in Fig. 3.4(c) and (d). Note, that the labelling of these two hybridised states as quantum numbers $n = 20$ and 21 is due to these being the missing quantum numbers from the two bands of the bulk. The quantum number of the edge states can be considered to be the coefficient α, which, in this case, for both states is $\alpha = 0.57735i = -0.57735e^{i2\pi/\tau}$.

The commensurate case is far more intriguing, as for both $\lambda < 0$ and $\lambda > 0$ there is a single mid-gap edge state. These states are localised to the side of the lattice where the tunnelling coefficient to the single connected lattice site is equal to $(1 - \lambda)$, i.e. the weaker of the alternating tunnelling terms. It is not surprising that a bound state would localise to this, as a weaker tunnelling coefficient reduces its energy. This result of a single state for all $\lambda \neq 0$ is not contrary to the prediction from the Zak phase as the Zak phase is only valid in inversion symmetric models and for lengths commensurate with the period [182]. The termination of the lattice with the definition of a commensurate lattice $L_s = m\tau - 1$, or in a non-integer number of unit cells, does not preserve the symmetry of the system. For the commensurate lattice, there is a single in-gap bound state independent of the model parameters, and the quantum number is n for the bulk, with $k = n\pi/(L_s - x_0)$.

3.4 States in the presence of an impurity

Now, we place an impurity on the lattice. An impurity on a single-particle lattice model can be considered to be an on-site potential impurity, a tunnelling impurity, or a combination of the two forms. We will focus on the on-site potential impurity at a single edge of the lattice, which can be arbitrarily repulsive or attractive. However, the case of tunnelling impurities can also be considered using the same techniques discussed in this section. We focus on the case of an impurity located on the edge as this is analogous to edge softening and is the most physically relevant case for topological systems. It is also possible to extend the technique of this section to consider spatially extended impurities. The impurity will be deemed to be static, and in this sense, it is analogous to a classical defect of a solid state lattice. Note, the impurity we are considering does not necessarily preserve the symmetry of the system, in particular, the inversion symmetry, meaning it can destroy topological states without closing the bulk band gap [183].

Bloch's theorem is a consequence of the conservation of crystal momentum by a periodic potential [92]. However, with the introduction of an impurity, the perfect periodic nature of the system is broken. Impurities are to be expected in any real physical system, and this makes the consideration of topological models with an impurity an essential topic of study. The exact states of the model are still given by the forms of Eqs. (3.8) and (3.21). However, the transcendental equation to obtain the bulk quantisation, Eq. (3.9), is now an approximation, as the Bloch functions do not account for the presence of an impurity in the system. In other words, the impurity modifies the quantisation, i.e. k and α. To account for this variation, we must consider the Schrödinger equation of the model, which for the original clean Hamiltonian is given by Eq. (3.4).

We will consider the impurities to be added to the original system, giving a modified Hamiltonian

$$H_I = H + \Delta, \tag{3.32}$$

where H is the Hamiltonian of the original system, of the form of Eq. (3.1), and

$$\Delta = U\hat{c}^\dagger_{x'}\hat{c}_{x'} \tag{3.33}$$

is the operator of the impurity at site x' of strength U. For a potential impurity, k and α are obtained from the Schrödinger equation

$$\begin{aligned} J_{x,x-1}\psi_{\sigma,k}(x-1) + J^*_{x+1,x}\psi_{\sigma,k}(x+1) \\ + V_x\psi_{\sigma,k}(x) + U\psi_{\sigma,k}(x')\delta_{x,x'} = \epsilon_\sigma(k)\psi_{\sigma,k}(x), \end{aligned} \tag{3.34}$$

where $\delta_{x,x'}$ is the Kronecker delta function and $x' \in x$ is the label of the position of the on-site potential impurity. We will solve for all states of the lattice by considering the Schrödinger equation at the site where the impurity is located. Solving the Schrödinger equation at the site of the impurity for all states is a common approach for bound state problems on a lattice [184–186].

Topological states are robust against weak local perturbations [117, 187], especially perturbations which preserve the symmetry, e.g. changing on-site potential on a lattice site of a unit-cell. This robustness is according to the bulk-edge correspondence and is mostly relevant for disorder or impurities in the bulk. Of course, we can perform an act of *reductio ad absurdum* to prove that topological states cannot be arbitrarily robust from an impurity placed near the edge. If we introduce a wall into the lattice, i.e. an effectively infinite perturbation, the state cannot be robust against this being placed at positions close to the edge where it has a non-zero probability density. A simple energetic comparison can further corroborate this. The introduction of an on-site potential impurity at a single site modifies the energy on the order of the impurity strength if the corresponding state has a non-zero com-

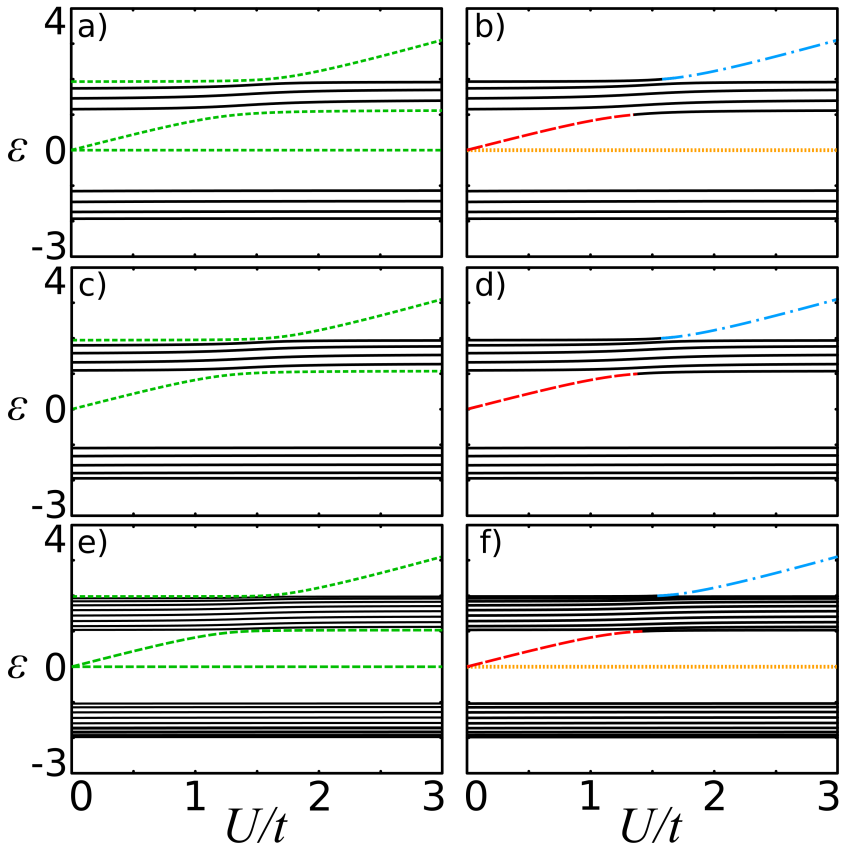

Figure 3.5: Energy spectra of the SSH model with an impurity of strength U/J on site $x = 0$. Model parameters are $\lambda = 0.5$ and a,b) $L_s = 10$, c,d) $L_s = 11$, and e,f) $L_s = 20$. The left panels, (a,c,e) show the numerical results of exact diagonalisation of the Hamiltonian at a resolution of $U/J = 0.01$ with solid (black) lines interpolated between data points of the energies always in the bulk bands and dashed (green) lines for energies that are at some point out of the bulk band. The right panels (b,d,f) show the analytical approach utilised in this work with solid (black) lines for states in the bulk band, the original x_0 edge state given by a dashed (red) line, the original L_s edge state given by a dotted (orange) line and the Shockley state out of the top of the band by a dashed-dotted (blue) line.

ponent on that site. A natural energy scale of the system is the finite bulk band gap. Therefore, a simplistic picture would imply that when the impurity strength is far larger than the bulk band gap, and if the impurity is 'felt' by the edge state, then the state that was initially in the gap will now have an energy that is outside the gap. In the rest of this chapter, we will characterise this robustness of the state against an impurity on the edge using the exact analytical edge states introduced earlier. Note, as we are considering the introduction of an impurity on the edge, the topology, characterised by the topological invariant, of the bulk bands will not be affected.

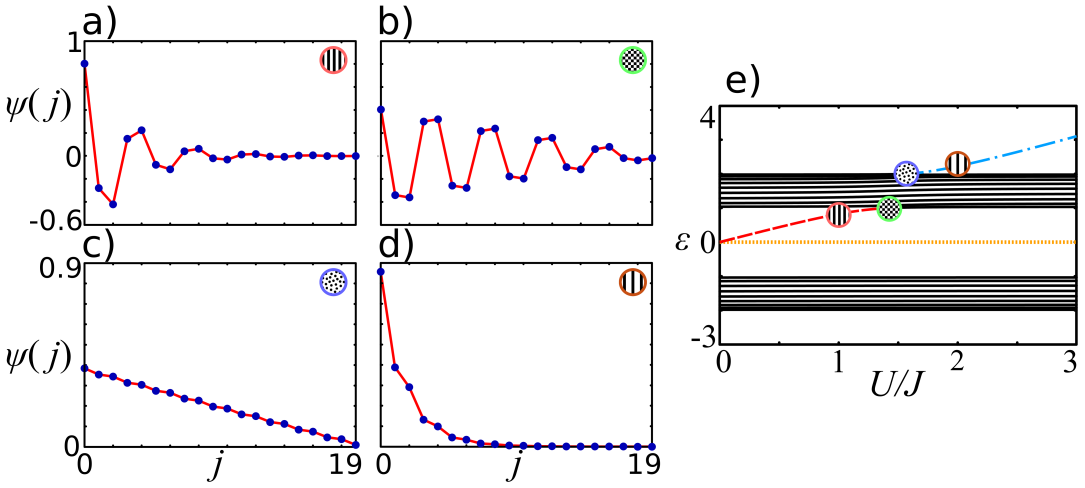

Figure 3.6: Wave functions of the states bound to x_0 of the SSH model for $\lambda = 0.5$ and $L_s = 20$. a) $U/J = 1$ with $\alpha = 0.725e^{i\pi/2}$, b) $U/J = 1.42$ with $\alpha = 0.977e^{i\pi/2}$, c) $U/J = 1.54$ with $\alpha = 0.978$, and d) $U/J = 2$ with $\alpha = 0.583$. e) The spectrum of the $L_s = 20$ SSH model. The circles filled with patterns label the position of the states, with each states corresponding circle in the top right corner of the panels a-d. The solid (red) lines are a guide for the eye between the analytical points and the numerics denoted by (blue) circles.

3.4.1 SSH model with a potential impurity

We can begin by considering the case of an impurity on a single edge of the lattice of the SSH model. The impurity will be located at the $x_0 + 1$ edge. Utilising the boundary condition $\psi(x_0) = 0$ and taking $x_0 = -1$, the Schrödinger equation of Eq. (3.34) at $x = 0$ will be

$$\epsilon_\sigma(k) = \frac{U}{J} + (1 - \lambda)\frac{\psi(1)}{\psi(0)}. \tag{3.35}$$

From this equation, by substituting in the exact bulk or bound states, k or α can be calculated for any impurity strength. Note, that we will consider the impurity strength in units of the tunnelling strength J and with a repulsive impurity ($U > 0$).

The above equation can be systematically solved for all k and α for a range of U. The energy landscape as a function of the impurity strength can then be considered from the exact calculations and compared to the calculation of the energies numerically, as is shown in Fig. 3.5. The analytical technique can quickly be seen to have a crucial advantage over the numerics, by obtaining the quasi-momentum k, the transition points from bound edge state to bulk state can clearly be identified by the points at which the quasi-momentum goes from being complex to entirely real, or alternatively where $|\alpha| = 1$. The form of the states can also be considered for changes in U, as in Fig. 3.6. For both the wave functions and the energies we observe perfect agreement between the exact diagonalisation numerics and the exact analytical approach.

The energy landscapes of the SSH model with varying impurity strength, Fig. 3.5, follow the simple energetic considerations discussed at the start of this section. We observe that bound states on the edge where the impurity exists increase in energy. These states merge with the bulk band at an impurity strength of the order of the bulk band gap. It is also observed that even a weak impurity can affect the topological states. The effect of a weak impurity is not only seen energetically but also in the wave function, as the edge state becomes less localised for impurity strengths below that which it merges with the bulk band, see Fig. 3.6a and b for an example. In addition, for the incommensurate system, the hybridisation of the two bound states is destroyed even by a small impurity of $U/J \sim 0.01$. This destruction of the hybridisation is not entirely surprising, as the required inversion symmetry and equivalent energies leading to the hybridisation is no longer met. Eventually, the edge state at x_0 merges with the bulk band resonantly with $|\alpha| = 1$ at the merging point.

After the edge state merges with the bulk, the bulk modes shift by small amounts in energy to accommodate the extra state in the band, see Fig. 3.5. Around the same energy scale as the original state merging with the bulk, a single state is ejected from the top of the bulk band. This state is trivially localised to the impurity and is, hence, a Shockley state [188]. The trivial localisation of the state is most easily seen at large U, for which the state goes as $\psi(0) \to \delta_{x,0}$ and the energy $\epsilon \sim U/J$. This state is to be expected, as when $U \to \infty$ the system must tend to the case of $L_s - 1$ with no impurity. For the infinite impurity strength limit, the Shockley state would effectively have infinite energy and would not exist, leaving the predicted $L_s - 1$ states.

It is of no surprise that the bulk band states are not as profoundly affected by these impurities, and that edge states localised to the boundary at L_s are not impacted at all. The bulk states are only altered energetically around points of merging/ejection of the bound states into/from the band.

3.4.2 Diagonal Harper model with an impurity

We can now consider a third model, the diagonal Harper model, which is often called the Aubry-André model. This model is a one-dimensional topologically non-trivial lattice where the periodicity of the system is contained in the on-site potential with a constant tunnelling strength. As the periodicity is fully contained in the on-site potential of the lattice, this model corresponds to the tight-binding approximation of a particle in a superlattice. The case of a superlattice has been realised experimentally in both photonic lattices [189, 190] and ultracold atoms [191]. We can

parametrise the diagonal Harper Hamiltonian as

$$H = -J \sum_x \left(\hat{c}_x^\dagger \hat{c}_{x+1} + \text{H.c.} \right) + \sum_x V_x \left(\Lambda, \tau, \theta \right) \hat{c}_x^\dagger \hat{c}_x, \tag{3.36}$$

with $x = 0, \ldots, L_s - 1$ (i.e. we set $x_0 = -1$). The potential term is defined as

$$V_x \left(\Lambda, \tau, \theta \right) = \Lambda \cos \left(\frac{2\pi x}{\tau} + \theta \right), \tag{3.37}$$

where θ is a constant phase offset and τ the spatial periodicity as previously defined. Hamiltonian (3.36) is also the reduced Harper equation of the two-dimensional Hofstadter model, where the phase θ is replaced with the quasi-momentum in the y-direction [192, 193]. We will show this in Sec. 3.4.3, where we will consider the Hofstadter model.

Having shown that the exact analytical method works for both edge and bulk states, we will move straight to considering the case of a static impurity in the diagonal Harper model. We will take an impurity placed at a single edge, $x = 0$, examples of two periodicities $\tau = 3$ and $\tau = 4$, and we set $\lambda/J = 1/2$ and $\theta = \pi$. As for the SSH model, we take as a parameter the dimensionless impurity strength U/J. We will select sizes of lattices which are commensurate in the limit of $U = 0$ but are effectively incommensurate in the limit of $U \to \infty$ after dropping the Shockley state that emerges from the top band. The behaviour of the energy spectrum as a function of the impurity strength is shown in Fig. 3.7, where we compare the results of exact diagonalisation and the exact analytical method. We note, again, that the exact analytical method gives us precise knowledge of where states enter/exit the bulk continuum bands.

For the case of $\tau = 3$, see Fig. 3.7b, there are three bulk continuum bands within which the bulk modes exist and for $U = 0$ there exists two edge states for the commensurate case with one in each band gap. As the impurity strength is ramped up, the edge mode in the lower band gap starts to move towards the above band whereas the second edge state is initially unaffected. However, with the lower energy edge state moving towards the middle bulk band, the top state of the bulk band is pushed out and this state, in turn, pushes the higher energy edge state towards the top bulk band. This avoided crossing of the two states at $U/J \approx 1.5$ appears to be a similar process to the usual Landau-Zener avoided crossing of two-level quantum systems [194]. The single edge state present in the band gaps for large U/J approaches, asymptotically ($U/J \to \infty$), the energy of the edge state for the incommensurate case ($L_s \to L_s - 1$). There is also a Shockley state which emerges from the highest energy bulk band and tends to infinite energy in the limit of the incommensurate case.

For the second example of $\tau = 4$ there are usually four bulk continuum bands, but for the choice of offset phase in this example, $\theta = \pi$, two of the bulk bands

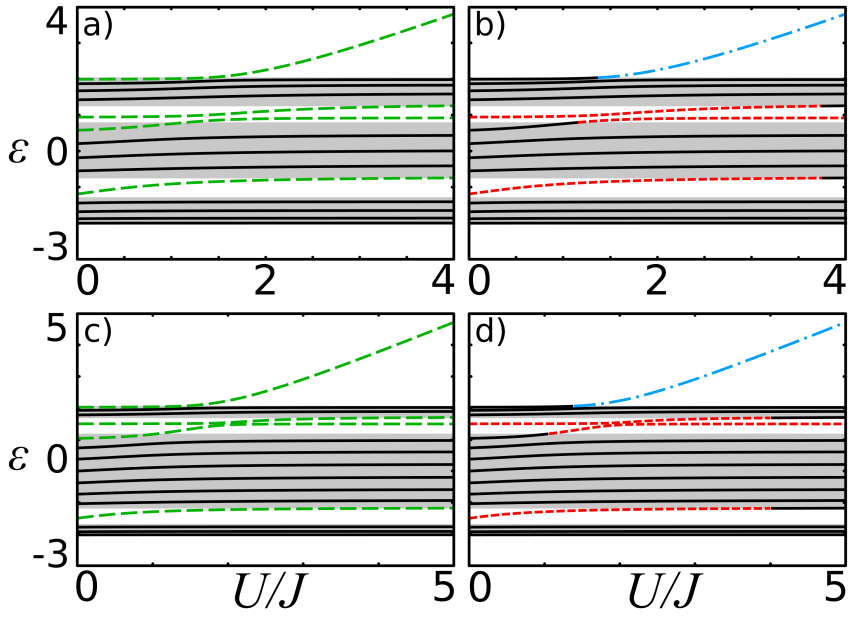

Figure 3.7: Energy spectrum of the Harper model with an impurity at $x = 0$ of strength U. Shaded areas of the plots represent the continuum bulk bands for the parameters. Values of $\lambda = 0.5$, $\theta = \pi$ and a,b) $\tau = 3$ $L_s = 14$ c,d) $\tau = 4$ $L_s = 15$ are selected. The left panels, (a,c) show the numerical results of exact diagonalisation of the Hamiltonian at a resolution of $U/J = 0.01$ with solid (black) lines interpolated between data points of the energies always in the bulk bands and dashed (green) lines for energies that are at some point out of the bulk band. The right panels (b,d) show the analytical approach utilised in this work with solid (black) lines for states in the bulk band, dashed (red) lines for edge states out of the continuum bulk bands and (blue) dash-dotted lines for the Shockley states out of the top of the spectra.

merge resulting in three bands. The behaviour of this example takes a similar form to the previously discussed case for $\tau = 3$. There is again an avoided crossing in a band gap and for large U/J a single edge state in the band gaps and a Shockley state which is scaling approximately as $\varepsilon \sim U/J$. For this example, we also consider the form of the edge states, which are shown in Fig. 3.8. From the structure of these edge states, we can observe how close the energy of the state is to the bulk band continuum by their extent in the lattice. It can be seen that when the edge states merge with or emerge from the bulk band, they are extended throughout the system as well as being localised to the wall. We also observe the localisation properties of the Shockley state for large U/J, see Fig. 3.8h, with it being localised to the impurity at $x = 0$. It is clear from their respective forms that different mechanisms localise the Schockley state and edge states.

3.4.3 Hofstadter model with a softened edge

The exact solutions that we have established can also be considered for systems where the model can be reduced down to the form of Hamiltonian (3.1). We will

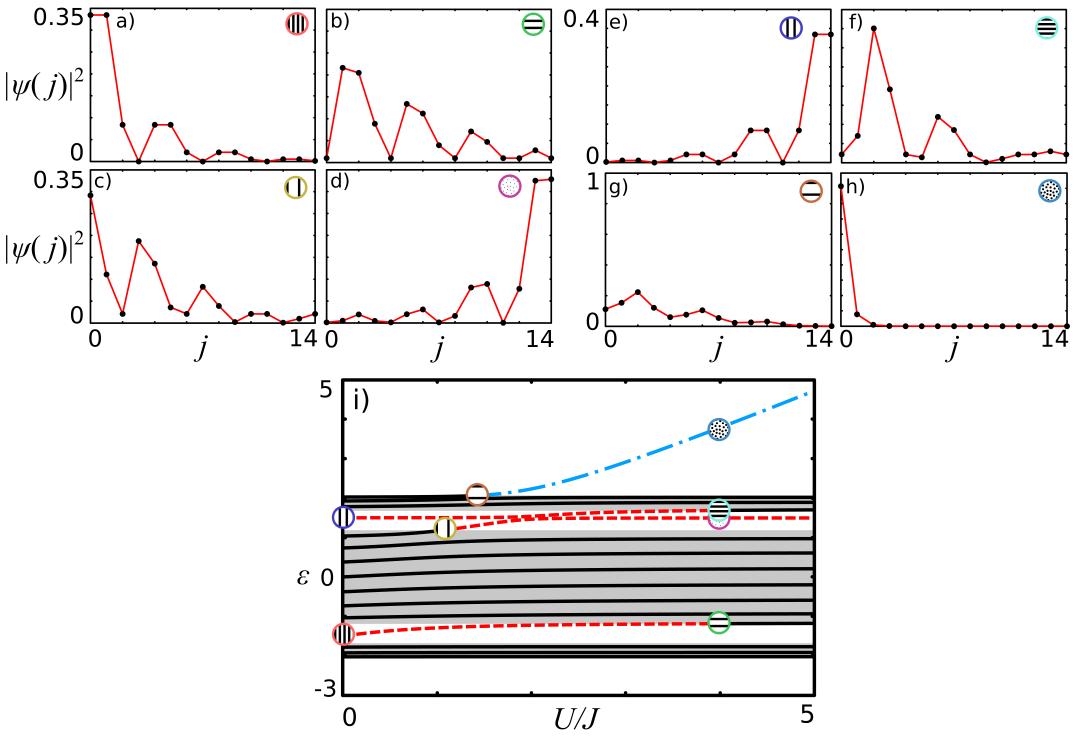

Figure 3.8: The edge probability densities of the diagonal Harper model for $\tau = 4$ and $L_s = 15$. Examples of the states are shown in a)-h) and the spectrum is shown in i) as a function of the impurity strength. On the spectrum circles filled with patterns label the position of the states, with each states corresponding circle in the top right corner of the panels a)-h). a,b) $U/J = 0$ edge state in the first band gap for a) $U/J = 0$ and b) $U/J = 4$. c,d) emerging state in second band gap that emerges from the band for c) $U/J = 1.07$ and d) $U/J = 4$, e,f) $U/J = 0$ edge state in the second band gap at e) $U/J = 0$ and f) $U/J = 4$ and g,h) Shockley state emerging from second band for g) $U = 1.39$ and h) $U/J = 4$. i) The spectrum of the $L_s = 15$ diagonal Harper model. Each state has ε and α of; a) $\varepsilon = -1.500$, $\alpha = 0.841e^{i\frac{\pi}{4}}$, b) $\varepsilon = -1.186$, $\alpha = 0.999999e^{i\frac{\pi}{4}}$, c) $\varepsilon = 1.187$, $\alpha = 0.990e^{i\frac{\pi}{4}}$, d) $\varepsilon = 1.495$, $\alpha = 0.840e^{i\frac{\pi}{4}}$, e) $\varepsilon = 1.500$, $\alpha = 0.841e^{i\frac{\pi}{4}}$, f) $\varepsilon = 1.686$, $\alpha = 0.999999e^{i\frac{\pi}{4}}$, g) $\varepsilon = 2.062$, $\alpha = 0.987$, h) $\varepsilon = 3.789$, $\alpha = 0.287$.

take an example of this in this section, with a two-dimensional model which in a particular geometry can be reduced to a one-dimensional problem.

An important and paradigmatic two-dimensional topologically non-trivial tight-binding model is that of the Hofstadter model [195] which has a Hamiltonian

$$H = -\sum_{x,y} \left[J_1 \hat{c}^\dagger_{x+1,y} \hat{c}_{x,y} + J_2(x)\, \hat{c}^\dagger_{x,y+1} \hat{c}_{x,y} + \text{H.c.} \right], \tag{3.38}$$

where $\hat{c}_{x,y}$ ($\hat{c}^\dagger_{x,y}$) annihilates (creates) a single particle at site (x, y). Hamiltonian (3.38) has only tunnelling terms with two independent tunnelling strengths, J_1 and J_2, in each direction. We will consider the case of the tunnelling being constant in one direction and periodic in the other, i.e. $J_1 = J$ and $J_2(x + \tau) = J_2(x)$. In particular, we will take the Hofstadter model in the Landau gauge which has a

periodic tunnelling term of form

$$J_2(x) = \Lambda e^{i\Omega(x)}, \tag{3.39}$$

with Λ being a constant strength and $\Omega(x) = 2\pi xp/q$ with p, $q \in \mathbb{Z}$. The fraction p/q then determines the periodicity of the lattice. For simplicity, if $p = 1$ then the periodicity is defined only by q. The Hofstadter model is well-studied already and has been experimentally realised using ultracold atoms [39, 196]. This model is known to be topologically non-trivial [113, 164, 195, 197] and exhibits the fractal Hofstadter butterfly for its spectrum with respect to p/q. Each bulk band of the model has a non-zero Chern number [193] which has been experimentally measured [99].

To reduce this two-dimensional problem down to a single dimension, we are required to take a particular set of boundary conditions, that of a strip geometry. The strip geometry boundary conditions are periodic (boundary-free) in the y-direction and open in the x-direction. With this geometry, the wave function is separable in the original coordinates as

$$\Psi(x, y) = \psi_{k_y}(x)\, e^{ik_y y}, \tag{3.40}$$

with k_y being the quasi-momentum in the y-direction, which due to the boundary conditions is defined $k_y \in [-\pi, \pi)$. We will drop the k_y sub-script for the single dimension wave function component $\psi(x)$. Substituting Eq. (3.40) into the time-independent Schrödinger equation $H\Psi = E\Psi$, a one-dimensional Schrödinger equation of form

$$\left[-J\sum_x \left(\hat{c}_x^\dagger \hat{c}_{x+1} + \text{H.c.}\right) + \sum_x V_x(\Lambda, \tau, k_y)\, \hat{c}_x^\dagger \hat{c}_x\right]\psi = E\psi, \tag{3.41}$$

is obtained, with a constant tunnelling strength defined by the tunnelling in the x-direction and a periodic on-site potential given by

$$\frac{V_x(\Lambda, \tau, k_y)}{J} = -2\lambda\cos(\Omega(x) - k_y), \tag{3.42}$$

which is defined from the tunnelling in the y-direction. We have set the dimensionless potential strength to be given by $\lambda = \Lambda/J$. The reduced Schrödinger equation is of the same form as that for the diagonal Harper model in Sec. 3.4.2. The component of the wave function of the Hofstadter model that we have labelled ψ in Eq. (3.40) is equivalent to the eigenstate of the corresponding diagonal Harper model.

We will again consider the effect of an impurity on the system, with a single impurity at site $x = 0$ of the reduced model. This impurity corresponds to a line defect at the edge of the two-dimensional system and is a relevant problem for this

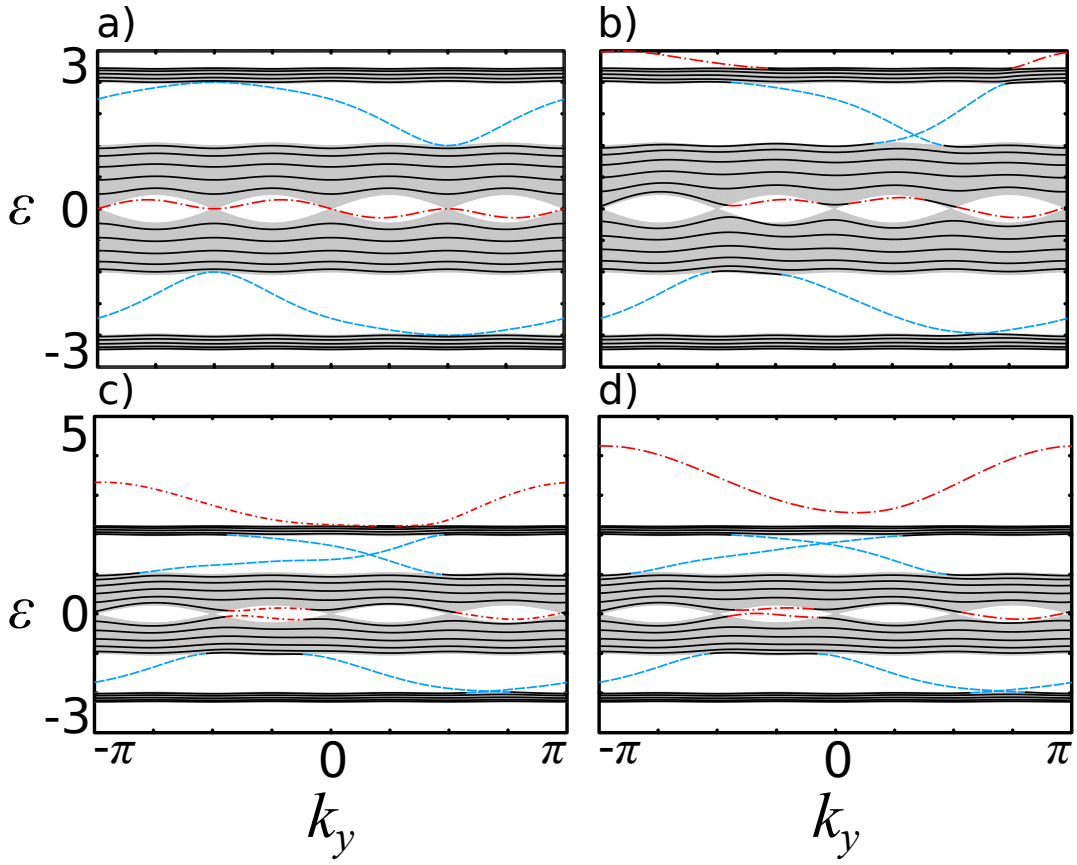

Figure 3.9: Spectra for the Hofstadter model by the exact analytical method for $J = 1$, $\lambda = 0.5$, $L_s = 23$ and an impurity of a) $U/J = 0$, b) $U/J = 1$, c) $U/J = 2$, d) $U/J = 3$. Bulk states given by solid (black) lines, edge states with phase π/τ by dashed (blue) lines and edge states with phase 0 by dashed-dotted (red) lines. Shaded (grey) regions define the infinite limit continuum in the x-direction.

system as it corresponds to edge softening. This form of defect could easily be present in the physical realisation of two-dimensional models and could have important effects on the topological edge states of the system. We will take an example case of periodicity $\tau = 4$ ($p/q = 1/4$), $\lambda/t = 1/2$ and consider a commensurate size of the lattice of $L_s = 23$. Four different values of the edge deformation are selected, and the corresponding spectra are shown in Fig. 3.9.

The Hofstadter model without an impurity for our choice of parameters is shown in Fig. 3.9a, and exhibits four bulk continuum bands and three topological states (one in each band gap). It is worth noting that the two edge states in the lowest and highest energy band gaps do not merge into the bulk continuum at any point in the quasi-momentum for $U = 0$. As a line defect is introduced on a single edge, we see that the three edge states merge with the bulk continuum bands at specific points in k_y. Again, we observe the emergence of a Shockley-like state. However, this Shockley state emerges from the top bulk band for smaller U/t at certain k_y. Note, that at points in the spectra where edge states cross in Fig. 3.9b, c and d, there are small gaps that are opened of the order of $\epsilon \sim 0.001$. The size of these

gaps decreases with increasing impurity strength and system size.

3.5 Robustness of states under a quench

We can take the use of the exact analytical states further and consider the robustness of edge modes to a quench of a potential generated by an impurity. This quench of the impurity is a feasible way of probing the stability of edge states in inhomogeneous lattices. The transition or decay probability of an edge mode initially prepared in a lattice without an impurity when the system is perturbed is a good measure of robustness. We will focus in this section on the diagonal Harper model and again use $\tau = 4$. The arguments in this section can be extended to other one-dimensional and reducible two-dimensional models.

We consider a model with an initial Hamiltonian of the same form as Hamiltonian (3.36) with no impurity which is perturbed at a time $t = t_1$. The perturbing operator term is a single-site potential acting on the lattice at a single site next to the edge, giving a full time-dependent Hamiltonian of

$$H'(t) = H + \frac{\mathcal{U}}{J}\theta(t - t_1)\hat{c}^{\dagger}_{x_0+1}\hat{c}_{x_0+1}, \tag{3.43}$$

where H is the diagonal Harper model Hamiltonian of Eq. (3.36), $\mathcal{U}$ is an impurity strength constant, and $\theta(t - t_1)$ is the Heaviside step function.

We will define the transition probabilities of an initial state $|i\rangle$ to a set of final states $F = \{|f_{\mathcal{U}}\rangle\}$ after the quench as

$$P_{i\to F}(t) = \sum_{f_{\mathcal{U}}\in F} |\langle f_{\mathcal{U}}|i(t)\rangle|^2, \tag{3.44}$$

where $|i(t)\rangle$ is the solution to the time-dependent Schrödinger equation at time t with an initial condition of $|i(t_1)\rangle = |i\rangle$. The initial state $|i\rangle$ is an eigenstate of the Hamiltonian for $t < t_1$ and the set of states $\{|f_{\mathcal{U}}\rangle\}$ are eigenstates for $t > t_1$ of the full Hamiltonian. The presence of a static impurity qualitatively and quantitatively changes the spectrum of all states. Therefore, the overlaps for the transition probability must be between the time-evolved initial state and a set of states from the eigenstates of the quenched Hamiltonian. We can write the evolved initial state as $|i(t)\rangle = \hat{U}(t, t_1)|i\rangle$, where $\hat{U}(t, t_1)$ is the propagator for the perturbed Hamiltonian. Then since the final states are eigenstates of the full perturbed Hamiltonian, the transition probabilities take the form

$$P_{i\to F}(t) = \sum_{f_{\mathcal{U}}\in F} |\langle f_{\mathcal{U}}|i\rangle|^2. \tag{3.45}$$

A possibly interesting and relevant process to consider is the transition of an initial topological edge state into the bulk continuum band states after a quench.

This type of transition probability could be regarded as a measure of the robustness of the edge state upon a quench. To calculate such a transition probability we need to take the initial state $|i\rangle$ to be one of the edge states of the model without an impurity and the set of final states $|f_{\mathcal{U}}\rangle$ to be the set of all states in the bulk band continuum of the spectra for the quenched Hamiltonian. Note, as we are summing only over the bulk states of the quenched system, the transition probability is not required to be a continuous function of the quench impurity strength, as the number of bulk states is not a conserved quantity. The expected discontinuities will give good measures of the transition points where topological states enter or exit the bulk bands.

We can utilise the known analytical form of the eigenstates of the system to simplify the calculation of the transition probabilities. Without loss of generality, we will consider the case of $x = 0, \ldots, L_s - 1$. All the transition probabilities calculated come down to the calculation of expectation values of the form $\langle \psi_k^{\mathcal{U}} | \psi_\alpha \rangle$, where $\psi_k^{\mathcal{U}}$ is a perturbed bulk mode and ψ_α is an unperturbed topological edge state. Substituting in the known exact forms of the states we can write the overlap calculation as

$$\langle \psi_k^{\mathcal{U}} | \psi_\alpha \rangle = \sum_{x=0}^{L_s-1} \left[A_k^* \phi_k^*(x) e^{-ikx} + B_k^* \phi_{-k}^*(x) e^{ikx} \right] \left[\bar{A}_\alpha \phi_+(x) \alpha^x + \bar{B}_\alpha \phi_-(x) \alpha^{-x} \right], \tag{3.46}$$

where the constants A_k, B_k, $\bar{A}_\alpha$ and $\bar{B}_\alpha$ are constants which mean the states are normalised and solutions to their respective time-independent Schrödinger equation. The simplification of the calculation comes from the periodicity of the Bloch functions $\phi_{\pm k}$ and $\phi_\pm$. After expanding Eq. (3.46), we find that all terms are of the form

$$S = \sum_{x=0}^{L_s-1} \phi_1^*(x) \phi_2(x) e^{zx}, \tag{3.47}$$

where we assume that the functions ϕ_1^* and ϕ_2 have a periodicity τ and z is an x independent parameter. First, we find the largest positive integer n such that $(n-1)\tau < L_s \leq n\tau - 1$. Then, using the periodic properties of ϕ_1^* and ϕ_2, we can write the form of the summations as

$$\begin{aligned} S &= \sum_{j=0}^{\tau-1} \phi_1^*(j) \phi_2(j) e^{jz} \sum_{m=0}^{n-1-j} e^{mz\tau} + \sum_{x=(n-1)\tau+1}^{L_s-1} \phi_1^*(x) \phi_2(x) e^{zx} \\ &= \sum_{j=0}^{\tau-1} \phi_1^*(j) \phi_2(j) e^{jz} \frac{e^{z\tau(n-j)} - 1}{e^{z\tau} - 1} + \sum_{x=(n-1)\tau+1}^{L_s-1} \phi_1^*(x) \phi_2(x) e^{zx}. \end{aligned} \tag{3.48}$$

The summations involved in the calculations of the overlap are, therefore, simplified to summations over the periodicity and summations of exponentials which have known solutions. This simplification could be useful for the calculation of overlaps and matrix elements for large systems in numerical codes.

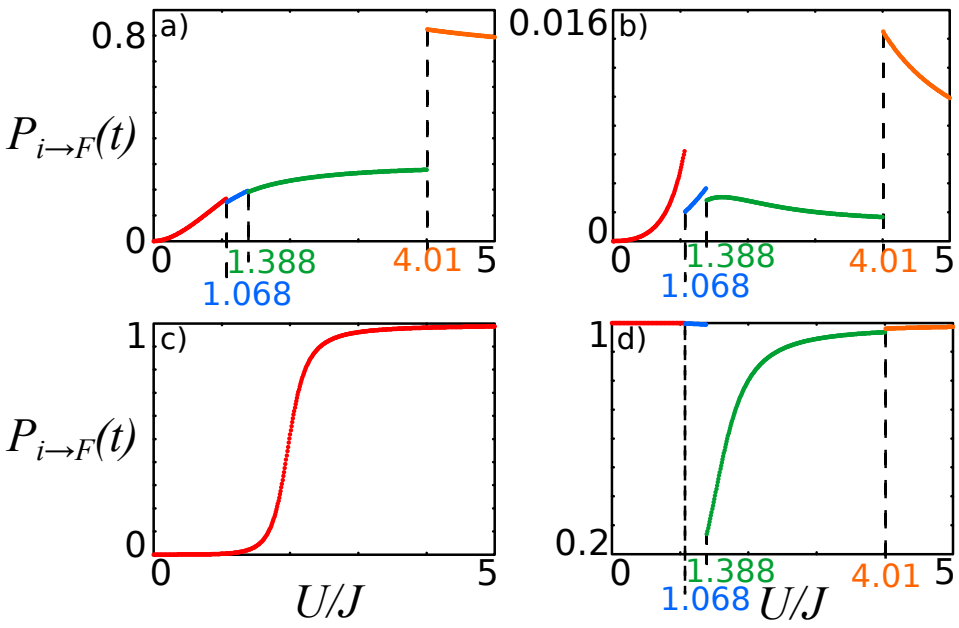

Figure 3.10: Transition probabilities defined in Eq. (3.44) for the quenched diagonal Harper model with $L_s = 15$ and $\tau = 4$ from an initial state (i) at $t = 0$ to a set of (or single) final states (F) at time t. a) i – edge state with $\varepsilon = -1.5$, F – all bulk states of the quenched Hamiltonian. b) i – edge state with $\varepsilon = 1.5$, F – all bulk states of the quenched Hamiltonian. c) i – edge state with $\varepsilon = 1.5$, F – the 11th state, which starts in the bulk and in the $U/J \to \infty$ is in the band gap, see Fig. 3.7d. d) i – highest energy state with $\varepsilon = 2.03$, F – all bulk states of the quenched Hamiltonian. Points of discontinuity are marked on the plots and correspond to points where states resonantly enter or exit the bulk continuum in the spectrum of Fig. 3.7d.

Having established the forms of the transition probabilities and discussed the advantage of knowing the exact analytical states, we can now consider the example of the diagonal Harper model. We will take $\tau = 4$, $x_0 = -1$ and $L_s = 15$, which is the same as the example in Sec. 3.4.2, with its spectra shown in Fig. 3.7d and the probability densities in Fig. 3.8. The transition probabilities for each of the two initial edge states into the perturbed bulk bands are shown in Fig. 3.10a and b. It can be seen that there are discontinuities in the transition probabilities when states enter or leave the bulk in the original spectrum shown in Fig. 3.7d. We also observe that the edge state localised to the edge where the impurity is placed exhibits sizeable transition amplitudes into the bulk after the quench. However, the edge state on the opposite wall has a much smaller transition probability due to the robustness of this state to the choice of placement for the impurity.

In Fig. 3.10c, we consider the transition probability of the two states that exhibit an avoided crossing in the second band gap shown in Fig. 3.7d. We observe the near-perfect transfer of the topological state from the initial edge state to the state that emerges from the middle band. We also consider the transition probability of the initially highest energy state in the top bulk band with the states of the bulk

continuum bands of the perturbed Hamiltonian in Fig. 3.10d. We observe that there is a significant transition probability of finding the initial state in this case outside of the bulk for moderate impurity strength, due to the Shockley state's energy being close to the energy at the top of the bulk band. However, a transition out of the bulk becomes highly unfavourable for a large quench, since the energy of the Shockley state is far from the continuum bulk band.

3.6 Chapter summary

In this chapter, we have constructed the exact analytical wave functions for general one-dimensional periodic Hamiltonians and higher dimension models that are reducible to one-dimensional problems. The method described obtains all states (edge and bulk) and their corresponding energies for finite periodic systems, without any constraint on the geometry, such as commensurability. The method introduced is extended to systems with impurities, and we consider in detail the relevant case of a potential deformation on the edge. The symmetry breaking placement of an impurity on the edge can have a drastic effect on the topological states of the lattice. We have seen that for weak impurity strengths, the edge states are robust, but, as would be expected, for large impurity strengths, they can become unstable. However, even for small and intermediate impurity strengths, there can be a non-negligible transition probability that a state prepared as an initial edge state of the Hamiltonian without an impurity could transition into the bulk. We observed that edge states that are localised to regions far away from any impurities are stable. The transition probabilities of initial edge states into the bulk continuum can exhibit discontinuities which are good measures of states entering or exiting the bulk at that impurity strength. The discontinuities (or resonances) could potentially be identifiable in realisations of topological models with the introduction (willingly or not) of an impurity into the system.

Chapter 4

Driven classical and quantum topological many-body systems

In out-of-equilibrium systems, it is possible for models to exhibit topological modes that are not characterised by the usual Chern numbers of the static case [198]. It has been shown that in a system where all the Chern numbers are zero for the static case, there can exist edge states in the driven counterpart [198]. In this chapter, we will consider the case of including strong interactions into these systems. Introducing interactions into out-of-equilibrium systems can be difficult, and this is the case for periodically-driven systems. There have been some examples of consideration of interactions in such models, e.g. the classification of topological phases in interacting systems [100] and the emergence of many-body localisation [199, 200]. In addition, the stability of edge states in periodically driven photonic lattices with nonlinearities (effectively interactions) has been investigated experimentally [201].

In this chapter, we will consider a first step to introducing strong interactions into a topological periodically driven model with chiral edge modes by considering a classical limit. Interactions are simpler to study in the classical picture as states do not contain superpositions. We will consider the classical limit by neglecting any phases in the system. The quantum model will also be considered for small lattices to confirm regions where the classical limit gives a good approximation to the full quantum dynamics. In part, this work is a comparison between discrete time classical [202] and quantum random walks [203–205]. It has been shown that classical and quantum random walks can behave rather differently in some cases [206, 207], and quantum walks can possess rich topological phases [208–211]. There has also been research into the phase transition between quantum and classical random walks [212–214]. This transition has been considered experimentally using a free-space optical set-up and tunable decoherence [215]. The tunable decoherence allows the transition to be probed as even small amounts of decoherence are known to make quantum random walks give classical results [216–218]. This quantum to classical transition makes sense, as the washing out of phases by decoherence

will make the classical dynamics a good approximation. It is this approach to the classical limit that we are utilising by neglecting phases. This chapter investigates whether the decoherence introduced from the presence of interactions make this classical limit a good approximation to the quantum dynamics.

We will begin this chapter by defining the quantum and classical models we will consider, including the form of the periodic driving. We then discuss the edge transport properties of the classical system via theoretical considerations and direct simulation in Sec. 4.2. The effect of interactions on the transport properties are considered in detail in Sec. 4.3, and the classical and quantum cases are then compared in Sec. 4.4. The chapter is finished by comparing the introduced observables of edge transport to the full transport properties. The work contained in this chapter resulted in the publication of Ref. [219], and the figures have been taken directly from this work.

4.1 Definition of the models

4.1.1 Quantum model

We will consider a periodically driven two-dimensional tight-binding lattice model, which is based on the model proposed in Ref. [198]. The dynamics of the model can be given by the time-dependent Hamiltonian

$$H(t) = \sum_{\langle \mathbf{i},\mathbf{j}\rangle} J_{\mathbf{i},\mathbf{j}}(t)|\mathbf{i}\rangle\langle\mathbf{j}| + \text{H.c.}, \tag{4.1}$$

with $\mathbf{i} = (i_x, i_y) \in \mathbb{Z}^2$ labelling the lattice sites and $\langle \mathbf{i}, \mathbf{j}\rangle$ restricting the summation to only over nearest-neighbours. We will consider the geometry of the two-dimensional lattice to be square, giving each site four nearest-neighbours. The tunnelling coefficients $J_{\mathbf{i},\mathbf{j}}(t)$ are driven periodically in time as

$$\begin{aligned}
&J_1\colon J_{\mathbf{i},\mathbf{j}\pm\hat{e}_y} = 0,\ J_{\mathbf{i}+\hat{e}_x,\mathbf{j}} = [1-(-1)^{i_x+i_y}]J \text{ for } mT < t \leq mT + T/4,\\
&J_2\colon J_{\mathbf{i}\pm\hat{e}_x,\mathbf{j}} = 0,\ J_{\mathbf{i},\mathbf{j}+\hat{e}_y} = [1+(-1)^{i_x+i_y}]J \text{ for } mT + T/4 < t \leq mT + T/2,\\
&J_3\colon J_{\mathbf{i},\mathbf{j}\pm\hat{e}_y} = 0,\ J_{\mathbf{i}+\hat{e}_x,\mathbf{j}} = [1+(-1)^{i_x+i_y}]J \text{ for } mT + T/2 < t \leq mT + 3T/4,\\
&J_4\colon J_{\mathbf{i}\pm\hat{e}_x,\mathbf{j}} = 0,\ J_{\mathbf{i},\mathbf{j}+\hat{e}_y} = [1-(-1)^{i_x+i_y}]J \text{ for } mT + 3T/4 < t \leq mT + T,
\end{aligned} \tag{4.2}$$

with $m \in \mathbb{Z}$, J a constant tunnelling strength, and $\hat{e}_x = (1,0)$ and $\hat{e}_y = (0,1)$ unit vectors of the lattice. The tunnelling coefficients couple pairs of lattice sites in an alternating fashion as is illustrated in Fig. 4.1. In effect, this periodic driving couples each site to each of its four nearest-neighbours in turn. This periodically driven toy model has been realised experimentally for the single-particle limit using photonic lattices [220, 221] and its topological nature shown by the presence of chiral edge states.

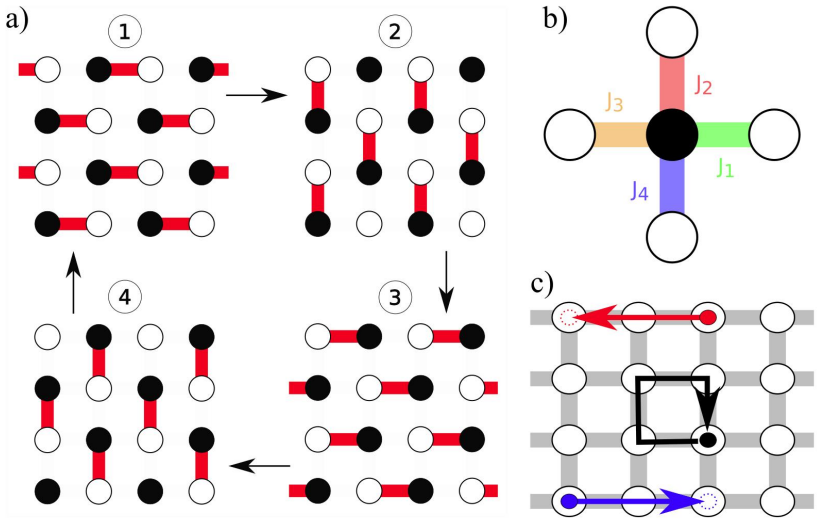

Figure 4.1: Illustration of the driven model. a) Steps for the periodic driving of this model. At each step the sites that are coupled are joined by red lines. Sublattice A(B) is drawn as a white(black) site. The lattice is periodic in the horizontal direction but has horizontal edges. b) The order of couplings from a single B site to the adjacent A sites. c) Illustration of edge (indicated by red and blue arrows) and bulk paths (black arrow) for unit tunnelling probability.

The quasi-spectrum of Hamiltonian (4.1) confirms the presence of edge states in the gaps, see Fig. 4.2. Note, that as we are considering the time evolution of the system by the unitary $\exp(-i/\hbar \int dt' H(t'))$, the correct parameter for the tunnelling in the system is Jt with t being the time scale of a single time step. The quasi-spectrum is the eigenvalues of the unitary evolution operator, as discussed in Sec. 2.3. There is a special point for this model for $Jt = \pi/2$, where the bulk continuum modes form a flat band, and the edge modes are linearly-dispersed. This special point will come up throughout this chapter, as at this point, we will find the quantum and classical cases to be equivalent. A single particle in one site is transferred to another perfectly for the special point tunnelling. As the tunnelling strength is decreased, the edge states dispersion shown in Fig. 4.2 attains curvature, which is well understood [222], and the bulk continuum is no longer a flat band. At a tunnelling strength of $Jt = \pi/4$, the bulk continuum band is across the full quasi-spectrum and the gap is closed. For $Jt < \pi/4$, there is no longer an edge state in the band gap, this is a normal topological transition as the gap has been closed across the transition.

4.1.2 Classical model

We will now define a classical many-body counterpart to the quantum model we have introduced. To do this, we neglect the quantum nature of the tunnelling process, that is the ability of the single-particle state to be in a superposition of

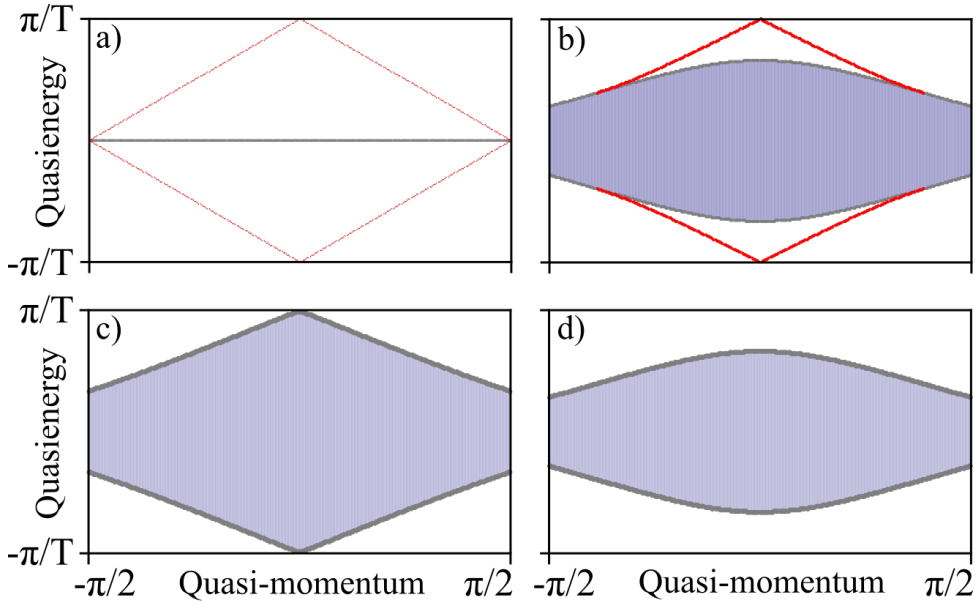

Figure 4.2: Spectra of the quantum model, with red data points representing edge modes and the bulk continuum band shown between grey markers. a) $Jt = \frac{\pi}{2}$ ($P_t \sim 100\%$) b) $Jt = 1.05$ ($P_t \sim 75\%$) c) $Jt = \frac{\pi}{4}$ ($P_t \sim 50\%$) d) $Jt = 0.52$ ($P_t \sim 25\%$).

sites. This is achieved by substitution of the quantum tunnelling coefficient by a classical tunnelling probability P_t at each time step of the periodic driving t. This classical model captures the dynamics of the quantum case at $Jt = \pi/2$ ($P_t = 1$) and, trivially, $Jt = 0$ ($P_t = 0$), when superpositions do not occur for a single particle in the quantum case. However, for tunnelling strengths sufficiently close to these points, it is not unreasonable to expect the classical model to be a good approximation.

A mapping between the quantum tunnelling coefficient and the classical probability can be obtained by exploiting the fact that the Hamiltonian only couples pairs of sites during each time step. The Hamiltonian in matrix form for a single pair in each time step is

$$H = \begin{pmatrix} 0 & J \\ J & 0 \end{pmatrix}, \tag{4.3}$$

with the wave function defined as

$$\psi(t) = \begin{pmatrix} c_1(t) \\ c_2(t) \end{pmatrix}, \tag{4.4}$$

where $c_{1(2)}(t)$ is the coefficient for the occupation of site 1(2) at time t. We pick the initial state to be $\psi(0) = (1, 0)$ and then we solve the Schrödinger equation after a

single time step t_i. The evolution of the state is enforced by the unitary operator

$$U = e^{-iHt_i} = \begin{pmatrix} \cos(Jt_i) & -i\sin(Jt_i) \\ -i\sin(Jt_i) & \cos(Jt_i) \end{pmatrix}, \tag{4.5}$$

which is of a similar form to the two-dimensional rotation matrix. After propagation, this results in a probability density of

$$\begin{pmatrix} |\, c_1(t)\,|^2 \\ |\, c_2(t)\,|^2 \end{pmatrix} = \begin{pmatrix} \cos^2(Jt_i) \\ \sin^2(Jt_i) \end{pmatrix}. \tag{4.6}$$

We can then find that for a single time step the mapping between the quantum tunnelling to the classical probability for a single particle is

$$P_t = \sin^2(Jt_i). \tag{4.7}$$

This mapping matches the known points of $Jt = \pi/2 \mapsto P_t = 1$ and $Jt = 0 \mapsto P_t = 0$.

To compare the dynamics of the classical and quantum models, we can consider a general example of the return probability of a particle. The return probability is defined as the probability of a walker (quantum or classical particle) being in its initial location after an entire period of driving. We will label the initial site of the particle as $\mathbf{i}_0$, giving an initial state of $|\psi(0)\rangle = |\mathbf{i}_0\rangle$. After a single time step, t_1, the quantum state would be

$$|\psi(t_1)\rangle = \frac{A|\mathbf{i}_0\rangle + B|\mathbf{i}_1\rangle}{\sqrt{(|A|^2 + |B|^2)}}, \tag{4.8}$$

with $\mathbf{i}_1$ being the site connected to $\mathbf{i}_0$ and the coefficients A/B being dependent on the model parameters. For the classical case, the particle after a single time step has a probability of P_t or $1 - P_t$ of being in the site $\mathbf{i}_1$ or $\mathbf{i}_0$ respectively. In the quantum case, the coefficients are in general complex and can be expressed as $A = |A|\exp(i\phi_A)$ and $B = |B|\exp(i\phi_B)$, with ϕ_A and ϕ_B denoting the phase gained for the particle either remaining in the initial site or tunnelling after a single time step. For the quantum case, after one single period, the return probability can then be calculated to be

$$|\langle \mathbf{i}_0|\psi_{\mathbf{i}_0}(t_4)\rangle|^2 = P_t^4 + (1-P_t)^4 + 2P_t^2(1-P_t)^2\cos(\phi_S - \phi_L), \tag{4.9}$$

with $\phi_S = 4\phi_A$ and $\phi_L = 4\phi_B$ being the accumulated phases. The classical result is obtained for the accumulated phases having a difference of an odd integer times $\pi/2$.

For the classical simulations, we will consider N particles in the two-dimensional

square lattice already described with a strip geometry, i.e. periodic boundaries in the x direction and open boundaries in y. Each particle will have a tunnelling probability of P_t during each time step and will be considered to have the same properties as all other particles. We will choose the lattice to be square in its full size, with a number of lattice sites L in each direction and define a filling factor of the lattice as $\nu = N/L^2$. This classical model in the single-particle limit is similar to a random walk on a lattice.

4.1.3 Inclusion of interactions

The main focus of this chapter is to consider the effect of strong interactions on the single-particle robust edge states of this periodically-driven model. To simulate an effective hardcore interaction of the classical particles, we limit the occupancy of all sites at all times to one. This limitation is effectively taking a constrained classical random walk for every single particle. In the quantum model, we can consider strong interactions of either hardcore bosons or spinless fermions. Spinless fermions are far simpler to simulate, as the interaction is due to the statistics of the particle meaning the system is described by a single-particle Hamiltonian. Therefore, for the interacting quantum case, we will consider spinless fermions.

4.2 Edge Transport

The traditional observables for topological states are based on the measurement of transport properties. The most straightforward transport observable to consider for edge modes is the current $\mathcal{I}$ along the edge due to their conducting properties. As this is a dynamical problem, for any single edge the particle number is not conserved. Therefore, to measure the current, we consider the non-destructive measurement of the tunnelling of particles between lattice sites. We can then define a straightforward edge current by counting the number of tunnelling events of particles to the left N_L and right N_R along the considered edge. If we allow the system to evolve for m periods, we can define the edge current as

$$\mathcal{I} = \frac{N_L - N_R}{LmT}, \tag{4.10}$$

with the length of the lattice edge being L and the period time scale T.

For the simulations in this chapter, we will usually be considering randomly filled and uniformly distributed initial states of the lattice. This initial state is then evolved with the transport properties measured, and the process is repeated over a set of realisations then averaged. Under such an averaging the edge current of Eq. (4.10) will be zero due to the contribution of bulk modes that straddle the edge of the lattice. These bulk modes will be clear when we theoretically calculate the

edge currents in Sec. 4.2.1. Therefore, we need to define a more rigorous measure of the edge transport properties which will work for the case of random initial states. For this more rigorous measure, we will take a directional component of the full edge current. We will consider a single edge of the lattice, as the two edges in this strip geometry are equivalent under a rotation, see Fig. 4.1c. The directional component of the full current we select will be the flow of particles in the direction of the chiral edge state, for our case, this is to the left. This component will be referred to as the directional edge current, and we will denote it by $\mathcal{J}$. We can write the directional edge current in a simple form as

$$\mathcal{J} = \frac{N_L}{LmT}. \tag{4.11}$$

The directional edge current is positive by construction and is invariant to rotations of the Hamiltonian. We will show in Sec. 4.2.1 that the usual bulk modes of the periodic driving do not contribute to the directional edge current as they move in the opposite direction on the edge.

As already stated, we will consider uniformly filled random initial states where each site has a probability of ν of being occupied, with ν being the filling of particles for both quantum and classical cases. The simulations are conducted in position space, and we evolve the initial state through a number of periods of the driven dynamics. It is, therefore, more natural to consider the current observables in terms of the occupation of lattice sites than the number of tunnelling events we have considered above. Note, that movement along the edge only contributes to the current in two of the four time steps, as can be seen by the illustration of the driving in Fig. 4.1a. For a current observable we only need to consider pairs of lattice sites during the first and third time step, and we can break up the pairs of lattice sites into a left and right site. Then we can construct an observable for the current which is dependent on the occupation of one of the lattice sites in the pair before and after the time step. For each pair, the edge current can then be written as

$$\mathcal{I}\left(t_u\right) = \frac{n_{\mathrm{L}}(t_u) - n_{\mathrm{L}}(t_{u-1})}{LmT}, \tag{4.12}$$

where $n_{\mathrm{L}}(t_u)$ is the number operator on the left site of the pair at time t_u, with $t_u(t_{u-1})$ being the time after(before) the time step of the driving. The directional edge current can be denoted as

$$\mathcal{J}\left(t_u\right) = \frac{\left(n_{\mathrm{L}}(t_u) - n_{\mathrm{L}}(t_{u-1})\right)}{LmT} \frac{1 + \mathrm{sgn}\left(n_{\mathrm{L}}(t_u) - n_{\mathrm{L}}(t_{u-1})\right)}{2}, \tag{4.13}$$

with $\mathrm{sgn}(x)$ being the sign function of the term x. Note, for the classical case the number operator of any given site is either 0 or 1, whereas, for the quantum case, the number operator is within the range $[0, 1]$.

We will turn our attention briefly to the potential experimental implementation of the current measures discussed above. In an ultracold atomic setting, the currents defined in terms of the occupation of sites may be simpler to realise. A method of performing such a measurement could utilise the ability to project states into isolated wells in ultracold atoms [164, 223, 224]. Such a method would project the occupation of the lattice sites on the edge before a time step, allowing a measurement of the occupation of sites before and after a time step to be performed. To measure the occupation of the sites a similar protocol to that used to measure the imbalance of atoms between sites [191] could be implemented. This method requires only the techniques of lattice tilting, time-of-flight, and absorption imaging to allow the number of atoms in each site to be counted.

4.2.1 Theoretical edge transport in the classical limit

As the behaviour of the classical particles under the proposed driving is entirely probabilistic, we can consider the form of the edge currents theoretically. It is worth repeating that we are considering a randomly filled initial state with no multi-particle occupancies of sites in the lattice. The edge currents defined by Eqs. (4.12) and (4.13) are the observables that will be averaged over all possible initial states of the lattice and the evolution time.

As the problem is classical, the dynamics of any single particle in a lattice over a full period of evolution can be decomposed into a set of possible paths. This set of paths can be reduced by considering only paths that contribute to the measured full current defined by Eq. (4.12). Therefore, we obtain seventeen paths that a single classical particle can take in a single period that contribute to the edge current. The seventeen contributing paths are shown in Fig. 4.3. Note, that the contributing paths include what would be usually considered as 'bulk' modes with the particle starting and ending in the same site after a cyclotron-like motion. We will discuss the contribution of these states in due course, and we only stop here to note that the contribution of these 'bulk' modes goes against the contribution of the chiral edge current modes. The edge current measurement can be obtained analytically for the classical limit by deriving the probability for each of the contributing paths to occur. The probability of a path to occur is given from a combination of the tunnelling probability, P_t, and the filling, ν. In this section, we will calculate the current observables already discussed for both the non-interacting (NI) and strongly interacting (SI) cases for classical particles.

4.2.1.1 Calculating the probability of particular paths

We now describe the derivation of the probabilities for two example paths to occur. The probability of each path to happen will be denoted by p_i. We will assume that the particles are randomly and uniformly distributed and that no correlations

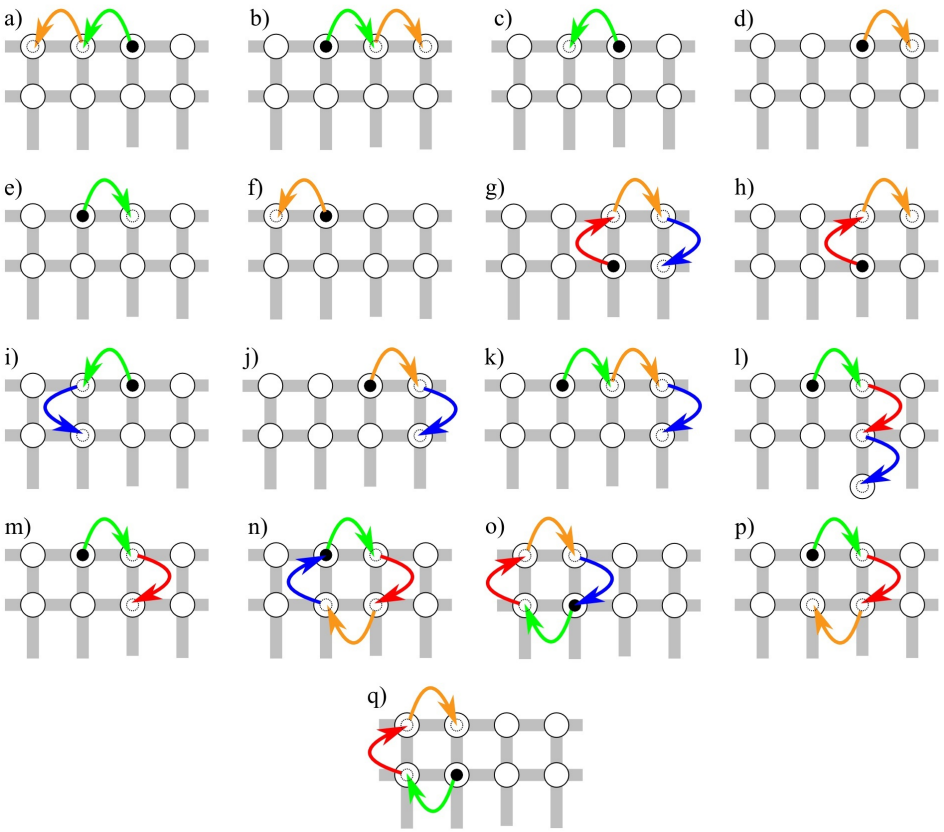

Figure 4.3: All possible one-body paths that contribute to the current, Eq. (4.12). The arrows are colour coded to the step they occur in our considered driving cycle as in Fig. 4.1b. © 2017 American Physical Society.

between particles build up over time. The second assumption is a reasonable one for classical particles and is in part the distinguishing difference between them and their quantum counterparts, i.e. no superposition or interference. In addition, with the averaging over initial states, any correlations can be expected to be washed out over long time scales. As the classical particles do not have the possibility of superposition, the contributing paths can be split into four parts to consider their behaviour independently in each time step of a single period.

It is natural first to consider the chiral edge path itself, which is shown in Fig. 4.3a. This path is separated into its four time steps that are required for it to occur and we can write the probabilities for each time step in the path to occur as

Step	NI	SI
1:	P_t	$P_t\,(1-\nu)$
2:	1	1
3:	P_t	$P_t\,(1-\nu)$
4:	1	1

. (4.14)

For the chiral edge state path the particle tunnels in the first and third time steps of the driving protocol. For the case of a non-interacting system, the particle tunnels

according to only the classical tunnelling probability. Whereas, for the instance of a strongly interacting system, with hardcore interactions, the tunnelling of the classical particle is also dependent on the site it is tunnelling to being unoccupied. In time steps two and four of the chiral path the occupied lattice site is not coupled to any other site according to the driving protocol. Combining the probabilities of each time step occurring we can obtain the full path probability for the chiral mode to be for non-interacting particles

$$p_a^{\mathrm{NI}} = \nu P_t^2, \tag{4.15}$$

and for strongly interacting particles

$$p_a^{\mathrm{SI}} = \nu P_t^2 \left(1-\nu\right)^2. \tag{4.16}$$

In these full path probabilities, we have also accounted for the probability of the initial site of the path being occupied at the start of the period which is given by the filling ν. Note, we have labelled the path probabilities with a subscript corresponding to the label of the path in Fig. 4.3, and we will follow this convention throughout this section.

As already discussed, this driving protocol has two chiral edge modes with a single chiral mode on each edge of the lattice. It is then not surprising that the path that is the opposite of the chiral edge mode for this boundary is a more complicated path to envisage. This path is shown in Fig. 4.3b. For each time step of the driving, the path probabilities are given by

Step	NI	SI
1:	P_t	$P_t\left(1-\nu\right)$
2:	$\left(1-P_t\right)$	$\left[\nu+\left(1-\nu\right)\left(1-P_t\right)\right]$
3:	P_t	$P_t\left(1-\nu\right)$
4:	$\left(1-P_t\right)$	$\left[\nu+\left(1-\nu\right)\left(1-P_t\right)\right]$

. (4.17)

The path probabilities for time steps one and three (when the particle tunnels) is straightforward and the same as for the chiral path itself. However, we can see that the path probabilities for the time steps two and four are more complicated than for the chiral edge mode. These path probabilities are not unity and contain the probability of a tunnelling event not occurring. For the strongly interacting case, there are two possibilities for the particle not to tunnel, either both lattice sites in the coupled pair are filled or the particle does not tunnel according to the tunnelling probability. From the path probabilities of the four time steps, we can derive the full path probability for the non-interacting case

$$p_b^{\mathrm{NI}} = \nu P_t^2 \left(1-P_t\right)^2, \tag{4.18}$$

a	$L\nu P_t^2$	j	$-\frac{L}{2}\nu P_t^2\left(1-P_t\right)^2$
b	$-L\nu P_t^2\left(1-P_t\right)^2$	k	$-L\nu P_t^3\left(1-P_t\right)$
c	$\frac{L}{2}\nu P_t\left(1-P_t\right)^2$	l	$-\frac{L}{2}\nu P_t^3\left(1-P_t\right)$
d	$-\frac{L}{2}\nu P_t\left(1-P_t\right)^3$	m	$-\frac{L}{2}\nu P_t^2\left(1-P_t\right)^2$
e	$-\frac{L}{2}\nu P_t\left(1-P_t\right)^2$	n	$-\frac{L}{2}\nu P_t^4$
f	$\frac{L}{2}\nu P_t\left(1-P_t\right)$	o	$-\frac{L}{2}\nu P_t^4$
g	$-\frac{L}{2}\nu P_t^3\left(1-P_t\right)$	p	$-\frac{L}{2}\nu P_t^3\left(1-P_t\right)$
h	$-\frac{L}{2}\nu P_t^2\left(1-P_t\right)^2$	q	$-\frac{L}{2}\nu P_t^3\left(1-P_t\right)$
i	$\frac{L}{2}\nu P_t^2\left(1-P_t\right)$		

Table 4.1: The contributed currents, j, of the seventeen contributing paths to the full current for the case of non-interacting particles with a tunnelling probability of P_t, a lattice length of L, and a uniform filling of ν. Each form of the current is labelled with a letter corresponding to the labels of Fig. 4.3.

and the strongly interacting case

$$p_b^{\mathrm{SI}} = \nu P_t^2\left(1-\nu\right)^2\left[\nu+\left(1-\nu\right)\left(1-P_t\right)\right]^2. \tag{4.19}$$

Having considered two example path probabilities in detail, we can now state the full path probabilities for all seventeen contributing paths. We now also take into account the number of times each path is possible to occur in the lattice, this is equal to the total number of initial sites of the correct type corresponding to that path. For this driving protocol, the lattice has two types of sites and each path is unique to the initial state being in a certain one of these sublattices. Therefore, the number of possible initial sites in the lattice for each path is given by $L/2$. We will also account for the 'strength' of each path in correspondence to the current, this is the number of tunnelling events in that path, as each tunnelling event is weighted equally in the measured current quantities. The range of possible current contributions for each path is the integers between -2 and $+2$. With the inclusion of these definitions, the terms we are writing are no longer the path probabilities but the current contributed by each path, which we will denote as j. For non-interacting and strongly-interacting particles, the contributed currents for all possible paths over a single period are shown in Tables 4.1 and 4.2 respectively.

4.2.1.2 Classical current for non-interacting particles

To calculate the full edge current as defined in Eq. (4.10) we can sum all the current contributions give in Table 4.1 for each of the seventeen paths. The result of this summation is that the full current is $\mathcal{I}_{NI} = 0$. This confirms the discussion of Sec. 4.2. If the state was initialised in the chiral edge mode or any of the other possible paths, then the current would be non-zero. The directional edge current is required to characterise the edge transport properties of the randomly filled lattice. Only four out of the seventeen considered paths contribute to the directional

a	$L\nu\left(1-\nu\right)^{2}P_{t}^{2}$
b	$-L\nu\left(1-\nu\right)^{2}P_{t}^{2}\left(\nu+\left(1-\nu\right)\left(1-P_{t}\right)\right)^{2}$
c	$\frac{L}{2}\nu\left(1-\nu\right)P_{t}\left(\nu+\left(1-\nu\right)\left(1-P_{t}\right)\right)^{2}$
d	$-\frac{L}{2}\nu\left(1-\nu\right)P_{t}\left(\nu+\left(1-\nu\right)\left(1-P_{t}\right)\right)^{3}$
e	$-\frac{L}{2}\nu\left(1-\nu\right)P_{t}\left(\nu+\left(1-\nu\right)\left(1-P_{t}\right)\right)^{2}$
f	$\frac{L}{2}\nu\left(1-\nu\right)P_{t}\left(\nu+\left(1-\nu\right)\left(1-P_{t}\right)\right)$
g	$-\frac{L}{2}\nu\left(1-\nu\right)^{3}P_{t}^{3}\left(\nu+\left(1-\nu\right)\left(1-P_{t}\right)\right)$
h	$-\frac{L}{2}\nu\left(1-\nu\right)^{2}P_{t}^{2}\left(\nu+\left(1-\nu\right)\left(1-P_{t}\right)\right)^{2}$
i	$\frac{L}{2}\nu\left(1-\nu\right)^{2}P_{t}^{2}\left(\nu+\left(1-\nu\right)\left(1-P_{t}\right)\right)$
j	$-\frac{L}{2}\nu\left(1-\nu\right)^{2}P_{t}^{2}\left(\nu+\left(1-\nu\right)\left(1-P_{t}\right)\right)^{2}$
k	$-L\nu\left(1-\nu\right)^{3}P_{t}^{3}\left(\nu+\left(1-\nu\right)\left(1-P_{t}\right)\right)$
l	$-\frac{L}{2}\nu\left(1-\nu\right)^{3}P_{t}^{3}\left(\nu+\left(1-\nu\right)\left(1-P_{t}\right)\right)$
m	$-\frac{L}{2}\nu\left(1-\nu\right)^{2}P_{t}^{2}\left(\nu+\left(1-\nu\right)\left(1-P_{t}\right)\right)^{2}$
n	$-\frac{L}{2}\nu\left(1-\nu\right)^{4}P_{t}^{4}$
o	$-\frac{L}{2}\nu\left(1-\nu\right)^{4}P_{t}^{4}$
p	$-\frac{L}{2}\nu\left(1-\nu\right)^{3}P_{t}^{3}\left(\nu+\left(1-\nu\right)\left(1-P_{t}\right)\right)$
q	$-\frac{L}{2}\nu\left(1-\nu\right)^{3}P_{t}^{3}\left(\nu+\left(1-\nu\right)\left(1-P_{t}\right)\right)$

Table 4.2: The contributed currents, j, of the seventeen contributing paths to the full current for the case of strongly interacting particles with a tunnelling probability of P_t, a lattice length of L, and a uniform filling of ν. Each form of the current is labelled with a letter corresponding to the labels of Fig. 4.3.

edge current. Summing the four contributing paths, we obtain the directional edge current for non-interacting particles to be

$$\mathcal{J}_{NI} = \nu P_t. \tag{4.20}$$

The directional edge current scales linearly with both the filling factor and tunnelling probability. For the case of non-interacting particles, there is no bound on the current as while $P_t \in [0,1]$, the filling ν is not bound from above.

4.2.1.3 Classical current for strongly interacting particles

We can consider the same process for strongly interacting particles with the current contributions given in Table 4.2. Again, by summing all seventeen currents, we obtain the full edge current averaged over random initial states to be zero, i.e. $\mathcal{I}_{SI} = 0$. The directional edge current, given from the four contributing paths is

$$\mathcal{J}_{SI} = \nu P_t \left(1-\nu\right). \tag{4.21}$$

The strongly interacting current is bound of course, as for hardcore particles $\nu \in [0,1]$. We also see that the directional edge current contains particle-hole symmetry as would be expected for the strongly interacting case.

4.2.1.4 Transport by mean-field

By merely inspecting the forms of the directional edge currents, a straightforward mean-field approach to obtaining the strongly interacting case can be seen. This mean-field accounts for effectively an 'excluded volume' term in the tunnelling. The map for a mean-field approach for the strongly interacting case is given by

$$P_t \to P_t\,(1-\nu)\,. \tag{4.22}$$

Therefore, to consider the strongly interacting case we can simulate non-interacting particles with a tunnelling probability rescaled by an 'excluded volume' term of $(1-\nu)$. In other words, the strongly interacting system can be simulated by a classical random walk that is not constrained but rescaled.

By taking this mean-field approach to the strongly interacting regime, we are considering a single particle interacting with a mean-field sea of randomly and uniformly distributed particles. This mean-field can be exploited to run simulations considering the dynamical behaviour of a single particle for the strongly interacting case. The interaction with a sea of particles is a good mean-field for the classical limit as correlations between particles do not build up over time. For a quantum system, this is not necessarily the case as the build-up of phases can result in the superposition and interference of multiple particles becoming more complex over time.

4.2.2 Link to traffic models

We have derived the forms of the measurable currents that characterise the classical edge transport. Another transport problem utilising components of random walks for a physical problem is the topic of models of traffic flow. There has been extensive research into the understanding of traffic flow problems [225–227] and these include models based on particle dynamics in a lattice [228]. One limit of traffic flow models is the Nagel-Schreckenberg cellular automata model [229]. This model starts with a random placement of cars on a grid of density ρ, with the grid being a discretisation of a road. Of course, cars can be said to be strongly interacting on-site, i.e. there is a maximum occupancy on each point of the grid of one. The model accounts for the dynamics of all cars with a four step algorithm: 1) Each vehicle is assigned a constant acceleration. 2) Other vehicles cause a deceleration of respective cars. 3) A random deceleration to each car with a certain probability is applied (this models differences in driving habits), 4) Each vehicle moves in a single direction according to its acceleration according to the first three steps [230]. The mean-field limit of this model considers a single car at any one-time and gives the flow of each car as

$$\mathcal{J}_{NaSch} = \rho\,(1-\rho)\,. \tag{4.23}$$

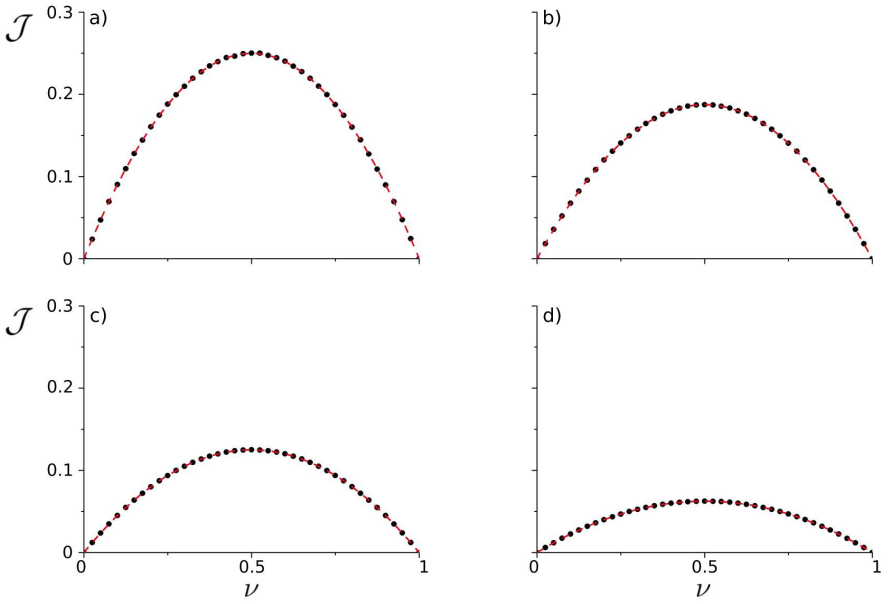

Figure 4.4: Directional edge currents in the strongly interacting case. Points (Black) are from the numerical simulations and the dashed (red) line is the theoretical estimation from Eq. (4.21). a)–d) correspond to different values of P_t, a) $P_t = 100\%$, b) $P_t = 75\%$, c) $P_t = 50\%$, d) $P_t = 25\%$. © 2017 American Physical Society.

This is equivalent to the case of strongly interacting particles in Eq. (4.11) for a tunnelling probability strength of unity.

4.2.3 Simulation of edge transport

The properties of the edge transport under the driving protocol considered can be simulated classically by a dynamical code evolving the initial particles' positions with time. We will consider an $L \times L$ lattice in a strip geometry with N particles in the lattice. We will fix the size of the system to $L = 100$ unless otherwise stated. This size is sufficiently large to avoid finite size effects while remaining manageable from a computational point of view. For each value of the tunnelling probability P_t, we run 5000 simulations of random initial configurations of the lattice and evolve for $m = 100$ periods. We consider as a measured quantity the directional edge current. We also check that the full edge current is zero to ensure we are averaging over sufficient initial states.

In Fig. 4.4, we compare the theoretical derivation of a directional edge current given by Eq. (4.21) and the results of the simulations described above. We observe a perfect agreement between the derived current and the simulations. This agreement is independent of the tunnelling probability. From the plots of the directional edge current, the particle-hole symmetry of the model is evident, with the current symmetric around the expected point of $\nu = 1/2$.

The classical results shown in Fig. 4.4 can be compared to the behaviour of the

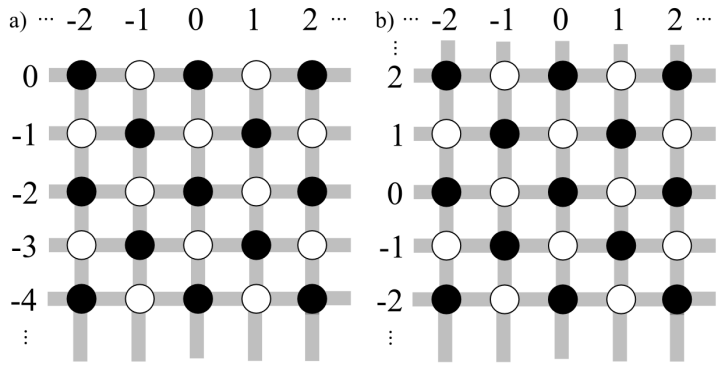

Figure 4.5: Geometries considered for the effect of interactions on transport in Sec. 4.3. a) an infinite half-plane with one edge. b) infinite system. Empty (full) sites denote the A-(B-) sublattice.

spectra of the quantum model in Fig. 4.2. For the quantum model, the spectra show that when the tunnelling strength is reduced, then the edge modes are lost into the bulk continuum band. We observe in the classical limit that the strength of the directional edge current decreases linearly with the tunnelling probability. This linear decrease would not be expected to be the case for the quantum dynamics. However, this means that for both the classical and quantum case, the edge paths are not robust for small tunnelling strengths.

4.3 The effect of interactions on transport

We will now take advantage of the classical mean-field mapping, Eq. (4.22), to consider the classical limit of the dynamics of a single particle in the interacting model. To perform these mean-field simulations, a single particle will be initialised in an edge or bulk path of evolution for the non-interacting limit. This particle will then be evolved according to the mean-field tunnelling probability of Eq. (4.22), i.e. it interacts strongly with a background of particles of density ν. The dynamics of the background particles are 'traced' away, i.e. the background particles are not evolved in time, which allows us to focus on the dynamics of the single evolving particle. We will set the tunnelling probability of the mapping to $P_t = 1$ and consider a varied filling factor of the background lattice. This means the mean-field tunnelling of the single particle is given by the excluded volume term $(1 - \nu)$. The chosen geometry of the system will be that of an infinite (lower) half-plane which has only a single wall boundary and is infinite in the three other directions. Simulations are conducted such that only the definite position of the classical particle is tracked. The considered geometry is shown in Fig. 4.5a.

The particle is initialised at a site (x_0, y_0), where x_0 is 0(1) if the particle starts in the $A(B)$ sublattice and y_0 denotes the distance from the edge, i.e. y_0 is all negative integers with the inclusion of zero for the edge itself. Note, that given a

non-interacting system, the initial site required for the occupation of the chiral edge path is $(0, 0)$. We track the single particle over its full evolution for a given long timescale. The evolution of the particle is repeated for each background ν then averaged over the realisations to obtain the average trajectory of the single particle. This average trajectory can be rather different from any single path of the particle, but it does give information on the average behaviour of the particle. It is also possible to calculate the mean speed of the particle, as we know the full trajectories of the single particle over many realisations for any given filling. We are particularly interested in observing if the particle when initialised in the chiral edge path stays on the edge or moves into the bulk on average due to the introduction of interactions. We have selected in this section the special point, $P_t = 1$, where the dynamics of classical and quantum hardcore particles are equivalent. Therefore, if the classical chiral edge paths move into the bulk on-average, then a quantum hardcore particle would be expected to on-average 'decay' into the bulk.

To simulate the quantum particle for this problem would usually require Monte Carlo simulations. For this phenomena, the use of Monte Carlo simulations is normally slow and the variances of the distribution tend to grow in time. Therefore, our approach in the classical limit is slightly different and instead uses a transition matrix approach. The transition matrix is considered to evolve the single particle through one period of evolution. From the transition matrix, denoted as $M(\mathbf{i}, \mathbf{j})$, we calculate the time-dependent probabilities of any single site being occupied after a single period of evolution as

$$O(\mathbf{i}; t) = \sum_{\mathbf{j}} M(\mathbf{i}, \mathbf{j}) O(\mathbf{i}; t - T), \tag{4.24}$$

with $O(\mathbf{i}; t)$ characterising the occupation of the site $\mathbf{i}$ at time t. As we consider the evolution of a single period, the transition matrix has a finite set of non-zero elements. This means that there are six distinctive transition matrices for the evolution of the particle dependent on if it is occupying one of six different types of lattice sites. These types of lattice sites are illustrated in Fig. 4.6. Therefore, to evolve the system according to the transition matrix approach, only six forms of the transition matrix need to be calculated. Of these six forms, two correspond to the occupation of the A and B sublattice sites along the edge, two correspond to the A and B sublattice sites one row in from the edge, and the last two correspond to all other A and B sublattice sites. The reduction of the number of transition matrices required cannot be shown immediately analytically. Instead, it is necessary to calculate a number of transition matrices and then observe that for any particle with $y_0 \leq -2$ the transition matrices are equivalent in each sublattice. This equivalence is because in a single period the particle will not 'feel' any effect of the edge when in the effective bulk of the lattice.

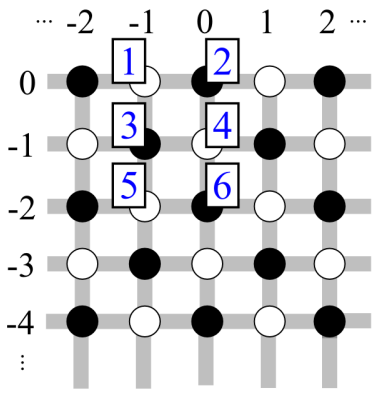

Figure 4.6: The six distinct sites for the half-plane geometry over one period. © 2017 American Physical Society.

All six distinct transition matrices for the considered driving can be derived by considering the particle in each of the initial possible positions. The derivation requires the probabilities of being in each site to be found after each time step. As each time step only couples pairs of sites, the overall extent of the possible sites the particle can be in after each time step is limited. It is straightforward to know the maximum number of possible non-zero elements of the transition matrix, for the model considered here it is 2^4. The presence of the single edge of the lattice can reduce the number of non-zero elements of the transition matrix. The analytical derivation of the transition matrices is simply an algebraic exercise which is similar to the calculations discussed in Sec. 4.2.1.1. As an example, we give here the transition matrix for a particle occupying site $(1, 0)$ at the start of a period. This example has non-zero transition matrix elements of

$$M(1,0) = (1-P_t)^3, \tag{4.25}$$
$$M(2,0) = P_t(1-P_t)^3, \tag{4.26}$$
$$M(2,-1) = P_t^2(1-P_t)^2, \tag{4.27}$$
$$M(1,-1) = P_t(1-P_t)^3, \tag{4.28}$$
$$M(1,-2) = P_t^2(1-P_t)^2, \tag{4.29}$$
$$M(0,-1) = P_t^2(1-P_t)^2 + P_t^2(1-P_t), \tag{4.30}$$
$$M(0,0) = P_t^3(1-P_t) + P_t(1-P_t)^2, \tag{4.31}$$
$$M(-1,0) = P_t^2. \tag{4.32}$$

For every single pair and time step in this mean-field approach, the particle will be blocked from tunnelling by a background particle with a probability of ν. We can consider the background particles to instead be impurities in the system and the interactions to play the role of Markovian disorder. In other words, the system loses memory of the position of the impurities which are allowed to move around the

lattice with the only conditions being a constant, uniform density of impurities at all times. Over long periods, the memory of the positions of particles in the background would be washed out, and the Markovian approach to the interactions will be a good approximation. However, the background particles should truly evolve according to the driving meaning that over short timescales this approximation may be a poor one. The Markovian disorder is different from a static disorder where once the particle interacts with an impurity, it will be present in that lattice site with unit probability for the rest of the dynamics. The static disorder case would correspond to a complete memory present in the system. The consideration of a Markovian type disorder is interesting in this context, as it has been shown that Markovian disorder can destroy topological states easier than static disorder can [231].

Plots of the average trajectories for each of the six distinct lattice sites for a range of background fillings are shown in Fig. 4.7. Note, the variance in the overall displacement after a long time evolution is significant due to the nature of the driven system considered. The variance is of the order of the displacement. We also include insets in Fig. 4.7 showing the short timescale average trajectories. The evolution of the particle in short timescales can be intricate and is dependent on the initial sublattice of the particle. During the particles initial evolution, if it occupies an A sublattice site, we see an average trajectory in the same direction as the chiral edge path (to the left). If the particle is initially in a B sublattice site, the short term average trajectory performs a loop, with the particle initially moving against the chiral edge path. This loop at the start of the average trajectory is due to the initial occupation of 'bulk' modes, and the loop itself is an example of a cyclotron-like motion.

Over long timescales, it can be seen that the edge paths of the particle dominate the transport. This makes perfect sense, as when the particle occupies 'bulk' paths its motion will be small in comparison to that occupying the edge path. When the background filling is increased, we observe that the average trajectory still overall moves in the direction of the chiral edge mode. However, the average trajectory of the particle does move into the bulk for all values of the filling, with a faster movement into the bulk for large ν. This 'decay' into the bulk of the particle is robust, even when the particle is initialised on or near the edge. To show this, we consider the mean long timescale speed of the particle in the x-direction, i.e. in the direction of the edge mode. We will fix the background density to a small value, $\nu = 0.1$, and consider all six initial start sites to show this 'decay' is robust. To the velocities, we fit an asymptotic function of

$$v_x(t) = a + bt^{-1/2} + ct^{-1}, \tag{4.33}$$

with a, b, and c being parameters of the fit. The mean speeds of the particle are shown in Fig. 4.8 including the fitted functions. Note, that all the calculated fits

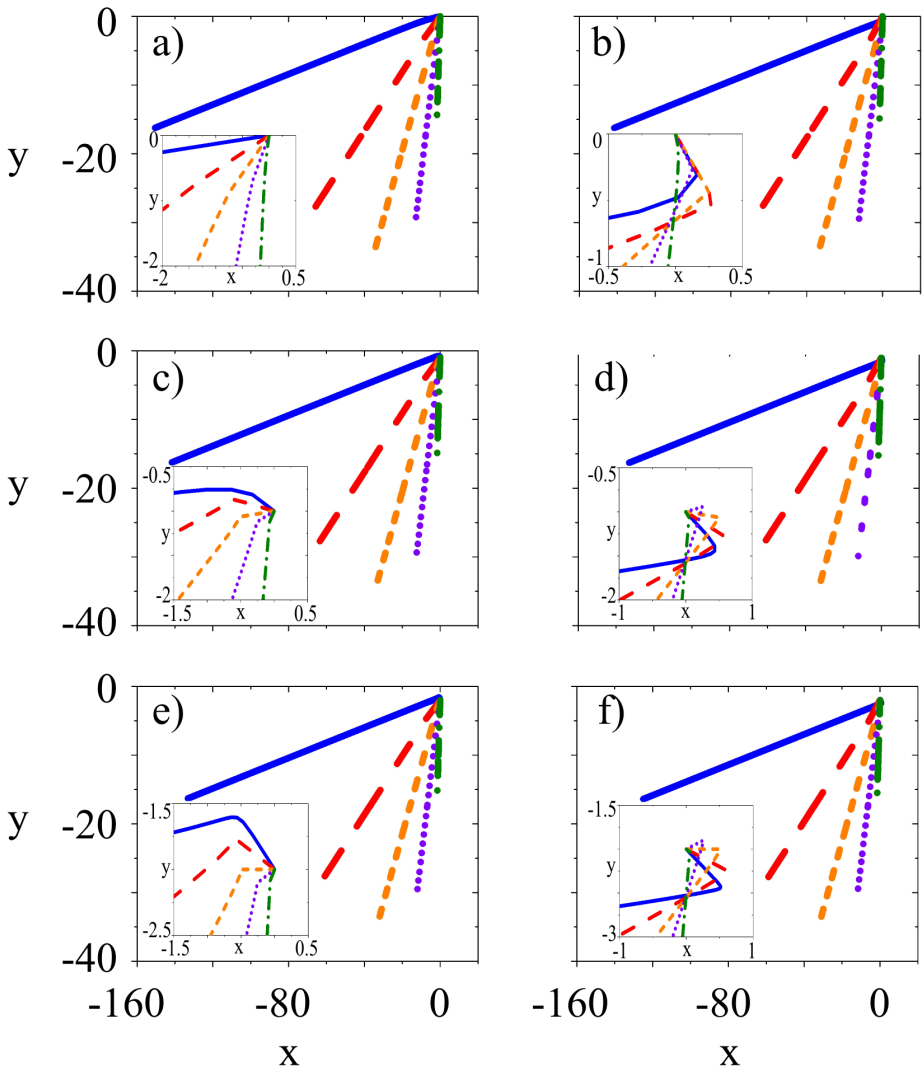

Figure 4.7: Trajectories of the average position over 2000 time periods starting from, a) A site row 0, b) A site row 1, c) A site row 3, d) B site row 0, e) B site row 1 and f) B site row 2. From each starting point we consider 5 fillings, solid (blue) $\nu = 0.1$, dashed (red) $\nu = 0.3$, short dash (orange) $\nu = 0.5$, dot (purple) $\nu = 0.7$ and dash dot (green) $\nu = 0.9$. The inset in each figure gives a close up look at the short time trajectories, of order 10-100 periods. Note, the variance in the particles average displacement is of order of the displacement. © 2017 American Physical Society.

are consistent with $a \equiv 0$ which corresponds to $\langle v_x \rangle_t \to 0$ at infinite time. There is also a slow deceleration of the average particle along x as $dv_x/dt \propto t^{-3/2}$, which can be considered to be a slow 'decay' of the occupancy of edge paths that have been coupled into initially or over the course of the dynamics. Recall that these results are equivalent to the quantum case for $P_t = 1$, meaning that in the case of a quantum model being driven we would also expect the edge modes to move into the bulk over long timescales. The timescales in which this 'decay' would occur is beyond the current experimental capabilities of driven systems but is becoming closer to being realisable with the implementation of state-recycling procedures in photonic lattices [232].

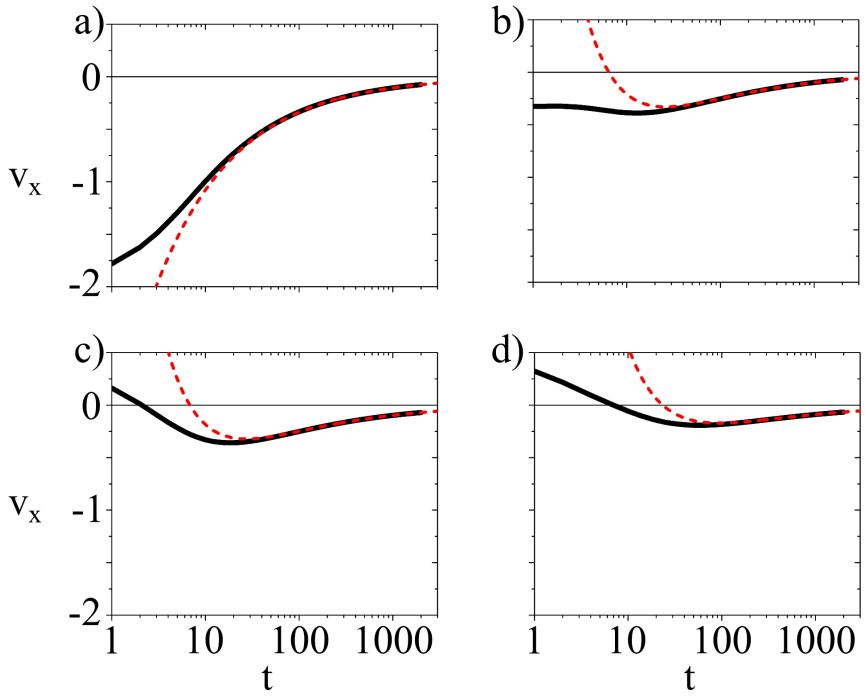

Figure 4.8: The average velocity (v_x) in x direction as a function of the number of periods (t), with fits (red dash) from Eq. (4.33). Starting in a) A site row 0, b) A site row 1, c) B site row 0, and d) B site row 1. The red dashed line is the fit from Eq. (4.33).

To consider the effect of interactions of a particle in a 'bulk' path, we now briefly consider the case of an infinite lattice in all directions with no edge, as illustrated in Fig. 4.5b. The two transition matrices of this geometry do not need to be calculated again, as they are equivalent to the two transition matrices considered for the lattice sites of $y_0 = -2$ in the previous geometry. We find that in this case again $\langle v_x \rangle_t \to 0$ for long times, as is consistent with the bulk nature of this geometry. The only effect of the interactions, in this case, is a small drift in the average trajectory from the cyclotron motion of the non-interacting case. This small drift is due to the coupling into alternative bulk modes when the particle interacts with the mean-field background.

4.4 Classical versus quantum evolution

We have claimed in this chapter that, in specific regimes, the classical limit we have taken will be a good approximation to the quantum model. In this section, we will compare the evolution of quantum and classical particles with hardcore interactions. We will also compare the transport properties by considering the directional edge current on average from randomly, uniformly distributed particles in the quantum case.

For the strongly interacting quantum particles, we can consider either spinless

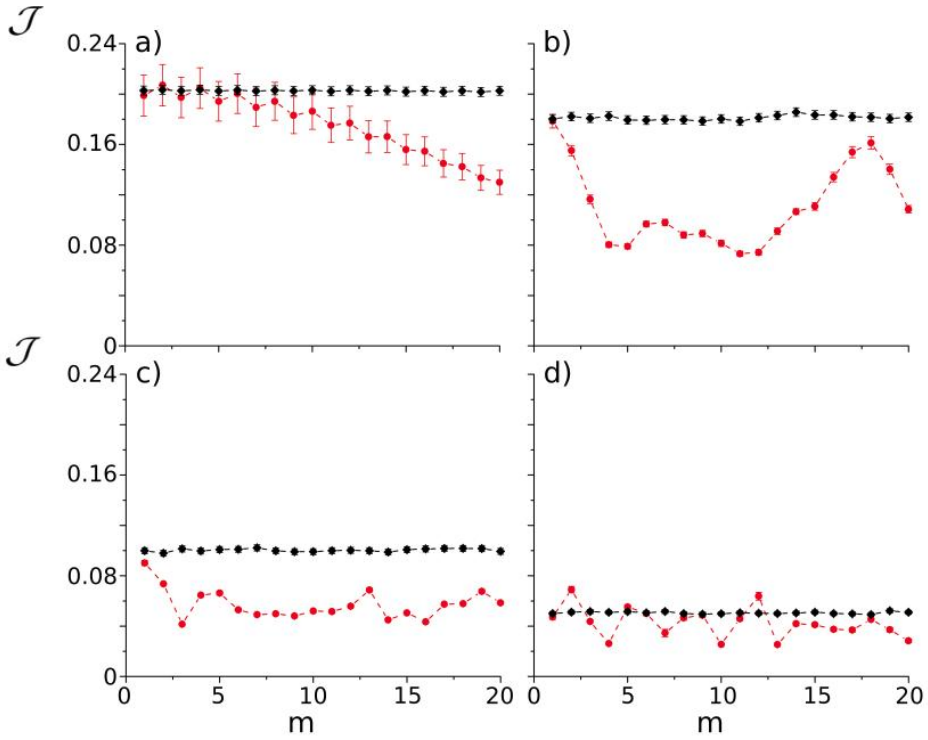

Figure 4.9: The average directional edge current $\mathcal{J}$ as a function of number of periods, m, for 4 particles in 16 lattice sites ($\nu = 0.25$). Circles (red) give spinless fermions and diamonds (black) give classical hardcore particles, for tunnelling coefficients of a) $J = 1.539\,(P_t = 0.999)$, b) $J = 1.249\,(P_t = 0.9)$, c) $J = 0.785\,(P_t = 0.5)$, d) $J = 0.524\,(P_t = 0.25)$.

fermions or hardcore bosons. It is known that in one dimension there is an exact mapping between spinless fermions and hardcore bosons [233], but this is not valid for all dimension in general [234, 235]. In dimensions higher than one, the different statistics of spinless fermions and hardcore bosons make their dynamics inequivalent. The classical limit considered in this work is valid for both spinless fermions and hardcore bosons, and we can take our pick. Hardcore bosons are notoriously difficult to simulate. However, spinless fermions are a non-interacting problem, as the statistics of the particles enforces the strong interactions. For the quantum particles, we will choose spinless fermions, to allow for efficient simulations which can be conducted on a desktop computer.

As we are now dealing with a non-interacting quantum problem it is natural to evolve the system according to a density matrix approach. The density matrix is defined from the wave function as

$$\rho(t_m) = |\Psi(t_m)\rangle\langle\Psi(t_m)|, \tag{4.34}$$

where t_m is the time at the discrete time step of the driving m. To evolve the density

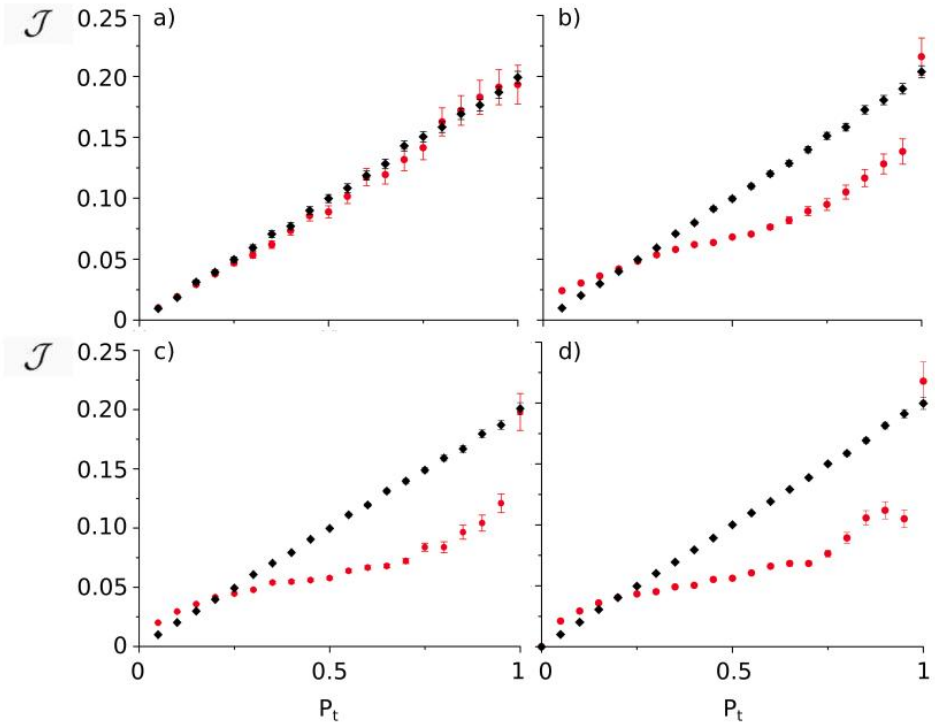

Figure 4.10: The average directional edge current $\mathcal{J}$ as a function of the classical probability, P_t, for 4 particles in 16 lattice sites. Circles (red) give spinless fermions and diamonds (black) give classical hardcore particles, for number of periods a) $m = 1$, b) $m = 5$, c) $m = 10$, d) $m = 20$. © 2017 American Physical Society.

matrix requires the usual unitary of time evolution and is given by

$$\rho(t_m) = e^{-iH(t_m)}\rho(t_{m-1})e^{iH(t_m)}. \tag{4.35}$$

In this case, $|\Psi(t_m)\rangle$ is the spinless fermion many-body wavefunction. The initial density matrix of the system is easily calculated from the initial positions of the particle. The initial state of the system has no correlations meaning the initial density matrix is diagonal in position space. The Hamiltonian in the evolution, Eq. (4.35), are the driven Hamiltonian of Eq. (4.1) and we again consider the transport properties in terms of the directional edge current. We will consider small lattices of 16 sites.

In Fig. 4.9, we show in detail the short timescale average transport properties of four spinless fermions as compared to classical particles. We observe that their transport properties after a single period of evolution are approximately the same but after a few periods of evolution the transport can be quantitatively quite different. The build-up of a difference between the classical and quantum transport properties is due to the growth of interference in the quantum case. As expected, for low tunnelling strength or classical probability, the dynamics are qualitatively similar. However, for intermediate tunnelling strengths, the transport properties differ substantially. The case of close to unity tunnelling probability shown in Fig. 4.9a is

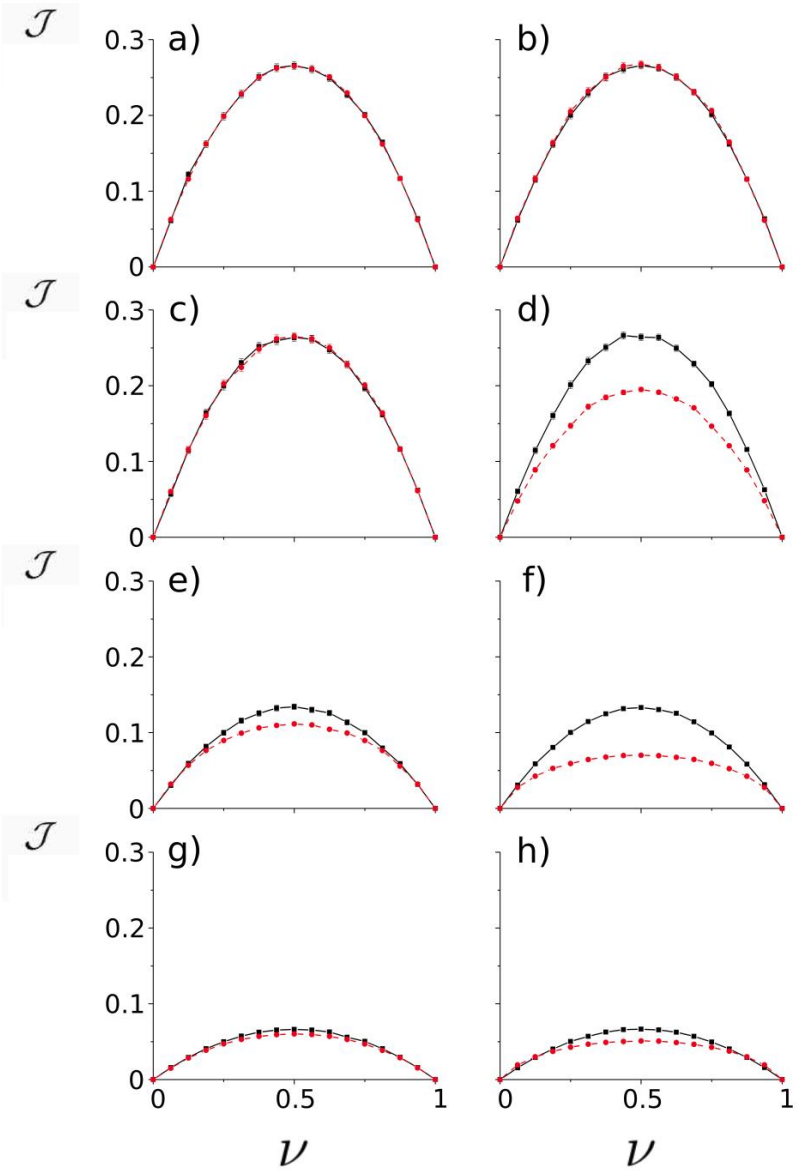

Figure 4.11: The average directional edge current $\mathcal{J}$ as a function of the filling, ν, of a 16 site lattice. Circles (red) give spinless fermions and squares (black) give classical hardcore particles, for tunnelling coefficients of a-b) $J = \pi/2$ ($P_t = 1$), c-d) $J \approx 1.539$ ($P_t = 0.999$), e-f) $J \approx 0.785$ ($P_t = 0.5$), and g-h) $J \approx 0.524$ ($P_t = 0.25$), after $m = 1$ (a, c, e, g) and $m = 30$ (b, d, f, h) time periods of evolution. © 2017 American Physical Society.

interesting, as for up until ten periods of evolution the transport is nearly equivalent, then we observe an increase in the interference of the quantum particles and a corresponding change in the directional edge current.

We next investigate the relationship between the transport and the tunnelling strength over a given number of periods for both the classical and quantum cases as shown in Fig. 4.10. We are again considering four particles in the 16 site lattice. For a single period of evolution, we observe a good agreement between the classical and quantum cases, as would be expected from previous results. However, for all longer

times of evolution, we find the same general behaviour, with agreement for low probability strengths but large deviations for large tunnelling strength. There is a substantial fall off in the observed directional edge current for small deviations away from the special point of unit tunnelling probability. These large discrepancies in the transport properties as $P_t \to 1$ are where the interference and superposition present in the quantum state propagate quickly from the initial state. For deviations from $P_t = 1$ up to order 10^{-3}, we observe agreement between the quantum and classical particles transport. The propagation of interference is expected to be slow in the case of small tunnelling strength, hence the agreement in this regime of evolution.

We now turn to the full transport behaviour in the lattice, where we consider the average directional edge current in a randomly, uniformly filled lattice of density ν as shown in Fig. 4.11. For a single period of evolution, we observe good agreement between the classical and quantum cases, which is in agreement with the previous findings of this section. The only discrepancies after a single period of evolution are around $\nu = 0.5$, these hint at the long term behaviour. The classical and quantum long term transport properties agree in the regions of small and large filling of the lattice. However, around the symmetric mid-point, the discrepancies can be significant, especially for intermediate tunnelling strengths. In these regions of disagreement, the classical limit over-estimates the current, as the quantum current is reduced due to interference in the state.

4.5 Directional and full current

When measuring transport quantities throughout this chapter, we have considered the directional edge current only. This is down to the fact that the full current averages to zero when averaging over all possible paths. However, the full edge current is not necessarily zero if we do not average over all possible initial configurations. We can then compare the measured transport of the full and directional current by restricting the possible initial occupancy of the lattice. This comparison is given in part to validate the use of the directional edge current as a transport measure, i.e. it picks up the same qualitative features.

The full edge and directional edge currents are defined in Eqs. (4.11) and (4.13) respectively. We will restrict the possible initial states that will be averaged over in any one simulation to initial occupation of a random set of A or B sites. As the topological states of the driven model require initial occupation of A sublattice sites, restricting the initial occupation to the A or B sublattice gives the initial state the possibility of occupying the chiral edge mode or not. We will consider simulations of a system of 36 lattice sites and conduct simulations of both the classical and quantum cases.

For perfect tunnelling, $J = \pi/2$ ($P_t = 1$), the dynamics of the system is well

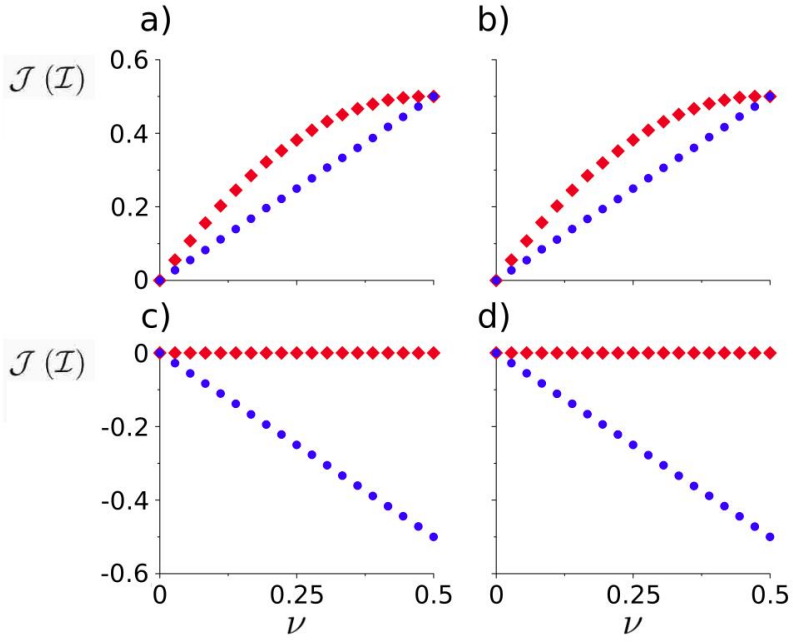

Figure 4.12: Average edge current $\mathcal{I}$ and directional edge current $\mathcal{J}$ on a 36 site lattice, with tunnelling strength $J = \pi/2$ ($P_t = 1$) and $m = 30$ time evolutions. Diamonds (red) denote $\mathcal{J}$ and circles (blue) denote $\mathcal{I}$. Cases of a) classical with the initial occupation of A sites only, b) quantum with the initial occupation of A sites only, c) classical with the initial occupation of B sites only, and d) quantum with the initial occupation of B sites only.

described by only knowing the form of the driving. If we have an initial state of only A or B sublattice sites, then after an integer number of periods only the respective A or B sublattice sites can be occupied. This is due to the pairing nature of the driving wherein each time step only lattice sites of different sublattices are connected. For this ideal tunnelling case, we will observe a non-zero directional edge current only for initial occupation of A sublattice sites. If the B sublattice sites are initially occupied then from the perspective of the top edge, only bulk paths are occupied and a negative full edge current would be observed. It is known that in the ideal tunnelling case there is only a single edge mode on the top edge, and it is moving in the positive current direction. Therefore, the directional edge current is a better observable for the occupation of paths in this scenario, as the full current is negative when there are no edge modes occupied.

For non-ideal tunnelling strength, the edge paths are not necessarily robust and can effectively 'decay' into the bulk. This decay was observed in Secs. 4.2.3 and 4.4 by a decrease of the observed current with decreased tunnelling strength. Also, we have shown that even in the ideal tunnelling case, an edge path can move into the bulk on average. We will consider tunnelling strengths away from the ideal case to compare the directional and full edge current. We would expect that over long timescales the full edge current should go to zero as the lattice will resemble the randomly occupied lattices studied so far.

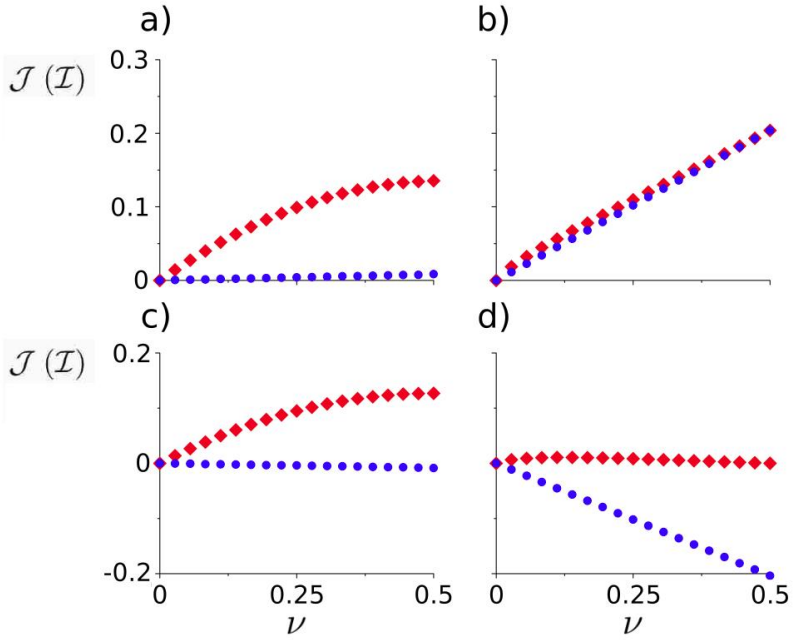

Figure 4.13: Same as Fig. 4.12, but with a tunnelling strength of $J \approx 0.785$ ($P_t = 0.5$) and $m = 30$ time evolutions. © 2017 American Physical Society.

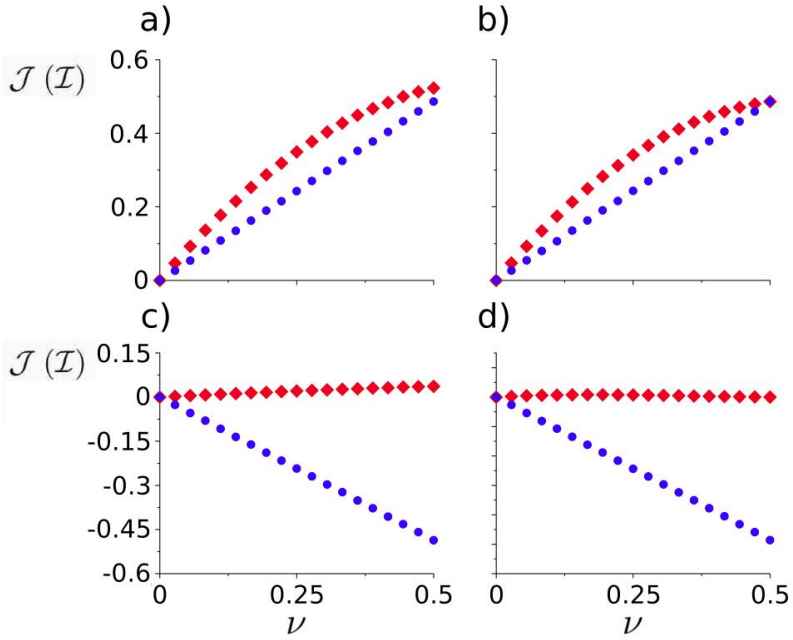

Figure 4.14: Same as Fig. 4.12, but with a tunnelling strength of $J \approx 1.249$ ($P_t = 0.9$) and $m = 30$ time evolutions. © 2017 American Physical Society.

We observe for the classical case a tendency towards the forms of the edge currents of the previous sections. This is seen in Figs. 4.12, 4.13, and 4.14. In each case the full edge current is of the opposite sign for the initial occupation of A or B sites. However, for the quantum case, we do not observe a similar form to the previous results. However, the net full current of both the A and B sublattice occupation is again zero in all scenarios. We also observe that for some cases of quantum evolution, the full and directional edge currents can coincide, see Fig. 4.13.

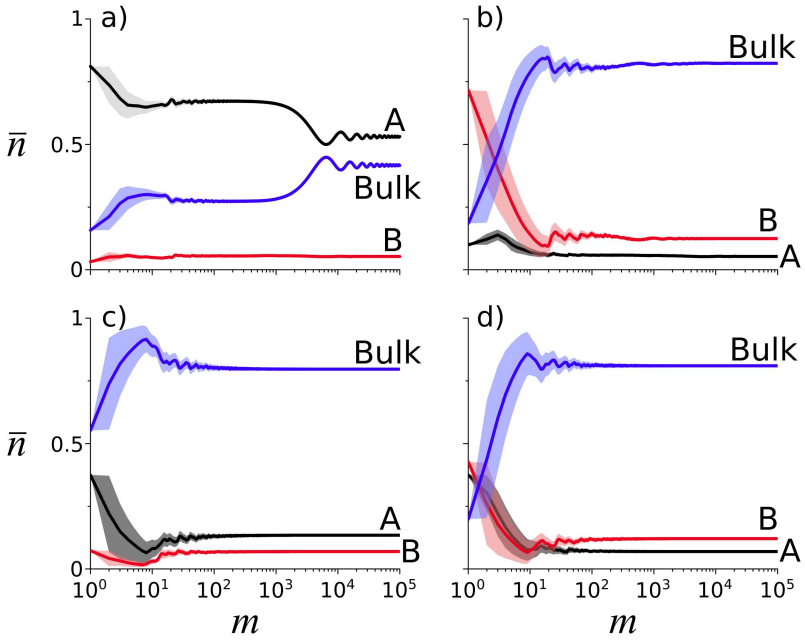

Figure 4.15: Average occupancy $\bar{n}$ in regions of the lattice, of a single-particle for the quantum case in a 36 site lattice after a number of periods, m. The lattice is split into three regions, A sites on the edge (black) denoted by 'A', B sites on the edge (red) denoted by 'B' and all other sites of the lattice (blue) denoted by 'Bulk'. The variance is given by the shaded regions of corresponding colour. a) Particle launched on A site on edge at $m = 0$ with $J \approx 1.249$, b) Particle launched on B site on edge at $m = 0$ with $J \approx 1.249$, c) Particle launched on A site on edge at $m = 0$ with $J \approx 0.785$, and d) Particle launched on B site on edge at $m = 0$ with $J \approx 0.785$. © 2017 American Physical Society.

The consideration of initial occupation of A or B sublattice sites has served well to confirm the forms of the currents we have assumed in this work. The full edge current is zero on average, and the directional edge current behaves similarly to the full current when edge paths are occupied. To investigate further the non-zero edge currents of the quantum case, we will study the evolution of a single particle initially in an A or B site. We will measure dynamically the average occupation over all previous periods of the A edge, B edge and bulk sites. We can take the occupation of A edge sites to be only A sublattice sites on the edge, and B edge sites to be only B sublattice sites on the edge. We will define the occupation of the bulk to be all other sites in the lattice. The average occupation of A sublattice sites gives a good indication of the directional edge current, as only paths that occupy these sites are in the edge path. If we initially occupy only A edge sites and have a strong tunnelling then after a long time evolution we observe the robustness of the edge paths, see Fig. 4.15a. However, if the tunnelling is decreased, then we observe a quick 'decay' of the edge paths into the bulk as is seen in Fig. 4.15c. Even for a low tunnelling strength, there is still a persistent occupation of some A sites on the edge over a long timescale. For the initial occupation of a B edge site, we observe

the particle to 'decay' quickly into the bulk, see Fig. 4.15b and d. This quick decay is of no surprise as the particle is initially in a site that couples with only bulk paths.

In this section, we have found that the directional edge current makes a good binary measurement of whether particles are occupying edge paths or not. A combination of both $\mathcal{J}$ and $\mathcal{I}$ is required to understand the dynamics of a driven system fully. However, in the case of the driving considered in this work with random initial states, only the directional edge current is required to characterise the dynamics of the system.

4.6 Chapter summary

In this chapter, we have focused on the properties of driven systems with anomalous edge states. We have considered the classical limit by considering no possible superpositions or interference. The classical limit was compared to the quantum case of spinless fermions in small lattices and observed regions where the two regimes are in agreement. We focused on the introduction of interactions into this topological driven system and observed that interactions can strongly affect the occupation of the edge modes of the system. We introduced a mean-field limit for the classical case that includes an excluded volume term. This mean-field can be used to study the dynamics of a single particle in a many-body system in the classical limit. The interactions we have considered can be seen as effectively a type of Markovian disorder, with impurities that are allowed to move. Overall, we have established that the introduction of interactions in topological driven systems can have a large impact on the behaviour of the edge modes. While edge modes will always exist in this system, as we have observed, the interactions can reduce the observable transport properties, and make the edge mode move into the bulk on average.

Chapter 5

Synthetic magnetic fields with a non-trivial topology

In this thesis, so far, we have considered the properties of a class of materials called topological insulators. However, as discussed in Chapter 2, topology is a broad topic and is in no way limited to the consideration of edge states and energy bands in lattices. In this chapter, we will consider the realisation of topologically non-trivial magnetic fields in ultracold atoms.

Within the community of ultracold atoms, there has been significant interest in the investigation and creation of knotted structures [42–46]. This interest includes the first knots in quantum matter, which were observed in spinor BECs [47, 48]. There have also been experiments to investigate the Shankar skyrmion, which is a knotted spin structure [49, 50]. Schemes have been proposed to imprint linked or knotted vortex structures onto BECs [51, 52]. Such knotted vortex lines, or knotted solitons, have been investigated in the context of both superfluids and superconductors [236–239]. There are also some proposals for fault-tolerant topologically protected quantum computing using topologically non-trivial vortex structures in superconductors [240, 241].

We will begin by discussing synthetic gauge fields using light-atom interactions and a finite number of internal atomic states. The scheme used in this work, the Λ-scheme, is introduced in Sec. 5.2. We then discuss the definition of topological linked and knotted magnetic fields in Sec. 5.3. A method to realise linked and knotted magnetic fields synthetically in ultracold gases is then proposed based on an expansion into Laguerre-Gaussian modes. This chapter is finished by considering the ground state of a trapped atomic gas in the three example synthetic magnetic fields of Hopf circles, linked rings, and a trefoil knot. The proposal contained in this chapter resulted in the publication of Ref. [242], and some of the figures of this chapter are taken from that publication.

5.1 Synthetic gauge fields

It is possible to mimic the behaviour of charged particles under magnetic fields in ultracold atoms in a variety of ways [55, 56, 74, 243–245]. One of these methods is to take advantage of the atom-light couplings present in the system by driving internal atomic transitions with lasers [69–71]. We will utilise one of these laser-driven methods in this chapter, the Λ-scheme. However, we will begin by considering a more general scenario of an atomic gas with internal energies and show how geometric gauge potentials can arise. This section takes a similar approach to that described in Refs. [55, 56] to show the introduction of synthetic magnetic fields in cold atomic gas systems coupled to light.

5.1.1 General geometric potentials

The Hamiltonian for the full atomic system under considerations is

$$\hat{H} = \sum_{n=1}^{N} |n\rangle \left(\frac{p^2}{2\mu} + V(\mathbf{r}) \right) \langle n| + \sum_{n,m=1}^{N} |n\rangle M_{nm}(\mathbf{r}) \langle m|, \tag{5.1}$$

with $V(\mathbf{r})$ being the position dependent trapping potential, $p = -i\hbar\nabla$ the momentum, μ the atomic mass, and $M_{nm}(\mathbf{r})$ the matrix elements of the atom-light interaction. The atom-light interaction matrix is of a similar physical origin as the optical lattice potential discussed in Sec. 2.2.2, and is also due to the interaction of an atomic dipole with the electromagnetic field of the light. The interaction matrix contains the Rabi frequencies for the atomic transitions, which we will discuss later. Hamiltonian (5.1) is written in the basis of the internal atomic states, $\{|1\rangle, \ldots, |n\rangle, \ldots, |N\rangle\}$. For the case of the Λ-scheme, the internal atomic state basis consists of only three states. However, we will work in general terms for now, with a basis of size N.

The internal state operator

$$\hat{M}(\mathbf{r}) = \sum_{n,m=1}^{N} |n\rangle M_{nm}(\mathbf{r}) \langle m|, \tag{5.2}$$

can be locally diagonalised to obtain a set of eigenstates $|\chi_n\rangle$ with $n = 1, \ldots, N$ with corresponding eigenenergies of $\epsilon_n(\mathbf{r})$ from the Schrödinger equation

$$\hat{M}(\mathbf{r})|\chi_n\rangle = \epsilon_n(\mathbf{r})|\chi_n\rangle. \tag{5.3}$$

These eigenstates are known as the atomic dressed states of the system. Any state can be expanded into any other basis, and the same can be done for the atomic

state in terms of the dressed state, giving

$$|\phi(\mathbf{r})\rangle = \sum_{n=1}^{N} \phi_n(\mathbf{r})|\chi_n(\mathbf{r})\rangle, \tag{5.4}$$

with $\phi_n(\mathbf{r})$ the coefficient of the wave function for the motion of the atoms in the dressed state $|\chi_n(\mathbf{r})\rangle$. The system's full time-independent Schrödinger equation is given by $\hat{H}|\phi(\mathbf{r})\rangle = E|\phi(\mathbf{r})\rangle$.

To connect the bare and dressed basis of the atomic levels, we can define a new operator

$$\hat{U} = \sum_{n=1}^{N} |\chi_n(\mathbf{r})\rangle\langle n|, \tag{5.5}$$

which performs the operation

$$\hat{U}|n\rangle = |\chi_n(\mathbf{r})\rangle. \tag{5.6}$$

It is straight-forward to see that this operator is unitary. The Hamiltonian in the bare basis can then be transformed into the dressed basis as

$$\hat{H}_T = \hat{U}^\dagger \hat{H} \hat{U} - i\hbar \hat{U}^\dagger \partial_t \hat{U}, \tag{5.7}$$

with ∂_t representing the derivative with respect to time. The second term in the transformed Hamiltonian is only relevant if the atom-light coupling matrix $\hat{M}(\mathbf{r})$ is time-dependent. The transformation of each term of Hamiltonian (5.1) is now considered, with the trap being invariant, i.e.

$$\hat{U}^\dagger V(\mathbf{r}) \hat{U} = V(\mathbf{r}), \tag{5.8}$$

the atom-light coupling being diagonalised, i.e.

$$\begin{aligned} \hat{U}^\dagger \hat{M}(\mathbf{r}) \hat{U} &= \sum_{n,m=1}^{N} |n\rangle\langle\chi_n(\mathbf{r})|\hat{M}(\mathbf{r})|\chi_m(\mathbf{r})\rangle\langle m| \\ &= \sum_{n=1}^{N} |n\rangle \epsilon_n(\mathbf{r})\langle n| \equiv \hat{\epsilon}(\mathbf{r}), \end{aligned} \tag{5.9}$$

and the momentum transformed as

$$\begin{aligned} \hat{U}^\dagger \hat{p} \hat{U} &= -i\hbar \sum_{n,m=1}^{N} |n\rangle\langle\chi_n(\mathbf{r})|\nabla|\chi_m(\mathbf{r})\rangle\langle m| \\ &= -i\hbar \sum_{n=1}^{N} |n\rangle\nabla\langle n| - i\hbar \sum_{m,n=1}^{N} |n\rangle\langle\chi_n(\mathbf{r})|\nabla\chi_m(\mathbf{r})\rangle\langle m| \equiv \hat{p} - \hat{A}(\mathbf{r}), \end{aligned} \tag{5.10}$$

where we have defined a vector potential

$$\hat{A}(\mathbf{r}) = i\hbar \sum_{m,n=1}^{N} |n\rangle\langle\chi_n(\mathbf{r})|\nabla\chi_m(\mathbf{r})\rangle\langle m|. \tag{5.11}$$

The time-dependence induced term is given by

$$-i\hbar\hat{U}^\dagger\partial_t\hat{U} = -i\hbar \sum_{m,n=1}^{N} |n\rangle\langle\chi_n(\mathbf{r})|\partial_t\chi_m(\mathbf{r})\rangle\langle m| \equiv \hat{\Phi}(\mathbf{r}). \tag{5.12}$$

Then Eq. (5.8) to Eq. (5.12) can be used to construct the transformed Hamiltonian

$$\hat{H}_T = \frac{(\hat{p} - \hat{A}(\mathbf{r}))^2}{2m} + V(\mathbf{r}) + \hat{\epsilon}(\mathbf{r}) + \hat{\Phi}(\mathbf{r}), \tag{5.13}$$

which is analogous to the Hamiltonian of a charged particle in a magnetic field with a corresponding vector potential $\hat{A}$ [76]. Note, the wave function has also been transformed as

$$|\phi_T(\mathbf{r})\rangle = \hat{U}^\dagger|\phi(\mathbf{r})\rangle = \sum_{n=1}^{N} \phi_n(\mathbf{r})|n\rangle. \tag{5.14}$$

In terms of the dressed states, $|\chi_n(\mathbf{r})\rangle$, from the form of Eq. (5.13) the equations of motion will be effectively those of a charged particle in a magnetic field with a corresponding vector potential $\hat{A}$. However, the ultracold gas needs to be prepared into these dressed states, or a subset of them, which is the focus of the next section.

5.1.2 Adiabatic approximation

If there is a subset of dressed states, e.g. $q \leq N$ states, which are well separated in energy from the other dressed states, then the dynamics of the states can be approximately separated. This is an adiabatic approximation which projects the system's dynamics onto a subset of internal energy states. The truncation of the basis can be achieved by the projection operator

$$\hat{P} = \sum_{n=1}^{q} |n\rangle\langle n|. \tag{5.15}$$

This adiabatic approximation is the same as the Born-Oppenheimer approximation, with the position of the atom and its internal energy levels being analogous to the nuclear and electron dynamics, respectively. In the Born-Oppenheimer approximation [246], the electron's dynamics are effectively integrated out and replaced by a potential energy surface for the nuclear degree of freedom. This approximation is valid as the time-scales of the nuclear dynamics are far slower than that of the electron dynamics. Therefore, this approach will be a good approximation if the dynamics of the internal energy levels are considerably faster than the motion of the atoms in space. Note, that the Born-Oppenheimer approximation without any

further approximations results in an effective vector potential for the slow system's dynamics due to the dynamics of the fast [247–249], which is a similar mechanism to the appearance of the synthetic vector potential by projecting into the dressed states.

The truncated Hamiltonian is obtained by the transformation

$$\hat{H}_A = \hat{P}\hat{H}_T\hat{P}, \tag{5.16}$$

note, there is explicitly no time-dependence in the projection operator. We can again calculate each transformation, with the trapping potential being truncated

$$\hat{P}\hat{\epsilon}(\mathbf{r})\hat{P} = \sum_{n=1}^{q} |n\rangle\epsilon(\mathbf{r})\langle n| \equiv \hat{\epsilon}^{(q)}(\mathbf{r}), \tag{5.17}$$

and the time-dependent scalar potential also being truncated

$$\hat{P}\hat{\Phi}(\mathbf{r})\hat{P} = -i\hbar \sum_{n,m=1}^{q} |n\rangle\langle\chi_n(\mathbf{r})|\partial_t\chi_m(\mathbf{r})\rangle\langle m| \equiv \hat{\Phi}^{(q)}(\mathbf{r}). \tag{5.18}$$

The momentum requires care due to the presence of the vector potential. We will first expand the momentum,

$$(\hat{p} - \hat{A}(\mathbf{r}))^2 = \hat{p}^2 - \hat{p}\hat{A}(\mathbf{r}) - \hat{A}(\mathbf{r})\hat{p} + \hat{A}(\mathbf{r})^2, \tag{5.19}$$

and consider each term independently. The transformation of $\hat{p}^2$ is given by

$$\hat{P}\hat{p}^2\hat{P} = -\hbar^2 \sum_{n=1}^{q} |n\rangle\nabla\langle n| \equiv (\hat{p}^{(q)})^2, \tag{5.20}$$

of $\hat{A}(\mathbf{r})^2$ by

$$\hat{P}\hat{A}(\mathbf{r})^2\hat{P} = -\hbar^2 \sum_{n,m=1}^{q}\sum_{k=1}^{N} |n\rangle\langle\chi_n(\mathbf{r})|\nabla\chi_k(\mathbf{r})\rangle\langle\chi_k(\mathbf{r})|\nabla\chi_m(\mathbf{r})\rangle\langle m|, \tag{5.21}$$

of $\hat{p}\hat{A}(\mathbf{r})$ by

$$\hat{P}\hat{p}\hat{A}(\mathbf{r})\hat{P} = -\hbar^2 \sum_{n,m=1}^{q} |n\rangle\Big[\langle\nabla\chi_n(\mathbf{r})|\nabla\chi_m(\mathbf{r})\rangle + \langle\chi_n(\mathbf{r})|\nabla\chi_m(\mathbf{r})\rangle\nabla\Big]\langle m|, \tag{5.22}$$

and of $\hat{A}(\mathbf{r})\hat{p}$ by

$$\hat{P}\hat{A}(\mathbf{r})\hat{p}\hat{P} = -\hbar^2 \sum_{n,m=1}^{q} |n\rangle\langle\chi_n(\mathbf{r})|\nabla\chi_m(\mathbf{r})\rangle\nabla\langle m|. \tag{5.23}$$

Of course, we want to write the truncated Hamiltonian with a momentum operator

of $\hat{p}^{(q)} - \hat{A}^{(q)}(\mathbf{r})$ with

$$\hat{A}^{(q)}(\mathbf{r}) = i\hbar \sum_{n,m=1}^{q} |n\rangle\langle\chi_n(\mathbf{r})|\nabla\chi_m(\mathbf{r})\rangle\langle m|. \tag{5.24}$$

We can consider if this is a correct form for the momentum by calculating the difference between this and the transformed momenta. This difference is given by

$$\hat{P}(\hat{p} - \hat{A}(\mathbf{r}))^2\hat{P} - (\hat{p}^{(q)} - \hat{A}^{(q)}(\mathbf{r}))^2 \equiv \Delta(\mathbf{r}). \tag{5.25}$$

We have all the terms required to calculate this difference, and it is a rather straightforward but long algebraic exercise. We find this difference to be

$$\begin{aligned}\Delta(\mathbf{r}) &= \hbar^2 \sum_{n,m=1}^{q} |n\rangle\langle\chi_n(\mathbf{r})|\left[\sum_{k=1}^{q} |\nabla\chi_k(\mathbf{r})\rangle\langle\chi_k(\mathbf{r})| - \sum_{k=1}^{N} |\nabla\chi_k(\mathbf{r})\rangle\langle\chi_k(\mathbf{r})|\right]|\nabla\chi_m(\mathbf{r})\rangle\langle m| \\ &= -\hbar^2 \sum_{n,m=1}^{q}\sum_{k=q+1}^{N} |n\rangle\langle\chi_n(\mathbf{r})|\nabla\chi_k(\mathbf{r})\rangle\langle\chi_k(\mathbf{r})|\nabla\chi_m(\mathbf{r})\rangle\langle m|.\end{aligned} \tag{5.26}$$

Therefore, we can write the truncated Hamiltonian

$$\hat{H}_A = \frac{(\hat{p}^{(q)} - \hat{A}^{(q)}(\mathbf{r}))^2}{2m} + V(\mathbf{r}) + \hat{\epsilon}^{(q)}(\mathbf{r}) + \hat{\Phi}^{(q)}(\mathbf{r}) + \hat{W}^{(q)}(\mathbf{r}), \tag{5.27}$$

with the geometric scalar potential

$$\hat{W}^{(q)}(\mathbf{r}) = \frac{\hbar^2}{2m} \sum_{n,m=1}^{q}\sum_{k=q+1}^{N} |n\rangle\langle\chi_n(\mathbf{r})|\nabla\chi_k(\mathbf{r})\rangle\langle\chi_k(\mathbf{r})|\nabla\chi_m(\mathbf{r})\rangle\langle m|. \tag{5.28}$$

Both the vector $\hat{A}^{(q)}(\mathbf{r})$ and scalar $\hat{W}^{(q)}(\mathbf{r})$ potentials emerge from the geometry of the atomic dressed states, and are, therefore, referred to as the geometric vector and scalar potentials.

5.2 Synthetic magnetic field from the Λ-scheme

The Λ-scheme requires a specific form for the energy levels of the atomic species. This particular form is shown in Fig. 5.1. The three energy levels are arranged with two ground states $|g_1\rangle$ and $|g_2\rangle$ coupled to a single excited state $|e\rangle$. The coupling of the ground and excited states is achieved via optical fields, i.e. laser beams, which are characterised by Rabi frequencies κ_1 and κ_2. Each Rabi frequency corresponds to the driving lasers spatial profile and phase and is given by

$$\kappa_{1,2}(\mathbf{r}) = E_{1,2}(\mathbf{r})e^{i\phi_{1,2}(\mathbf{r})}, \tag{5.29}$$

with $E_{1,2}(\mathbf{r})$ being the corresponding laser spatial profile and $\phi_{1,2}(\mathbf{r})$ the phase of the corresponding laser. We will drop the $\mathbf{r}$-dependence of the Rabi frequency for the following derivation of the dressed states and discuss its importance after. The atom-light coupling operator, written in the basis $\{|g_1\rangle, |g_2\rangle, |e\rangle\}$, for the Λ-scheme is given by [55]

$$\hat{M} = \frac{\hbar}{2}\begin{pmatrix} -2\delta & 0 & \kappa_1 \\ 0 & 2\delta & \kappa_2 \\ \kappa_1^* & \kappa_2^* & 0 \end{pmatrix}, \tag{5.30}$$

with 2δ denoting the detuning of the two-photon excitation with respect to the driving Raman laser. We will consider the case of the two-photon excitation, i.e. the offset of the frequencies of the two laser beams, being resonant so that $\delta = 0$. It is straightforward to find the eigenstates and energies of this Hamiltonian. The normalised eigenstates are

$$\begin{aligned} |+\rangle =& \left(\frac{\kappa_1}{\sqrt{2}\sqrt{|\kappa_1|^2 + |\kappa_2|^2}} |g_1\rangle + \frac{\kappa_2}{\sqrt{2}\sqrt{|\kappa_1|^2 + |\kappa_2|^2}} |g_2\rangle + \frac{1}{\sqrt{2}} |e\rangle \right), \\ |-\rangle =& \left(-\frac{\kappa_1}{\sqrt{2}\sqrt{|\kappa_1|^2 + |\kappa_2|^2}} |g_1\rangle - \frac{\kappa_2}{\sqrt{2}\sqrt{|\kappa_1|^2 + |\kappa_2|^2}} |g_2\rangle + \frac{1}{\sqrt{2}} |e\rangle \right), \\ |D\rangle =& \frac{1}{\sqrt{|\kappa_1|^2 + |\kappa_2|^2}} \left(\kappa_2^* |g_1\rangle - \kappa_1^* |g_2\rangle \right), \end{aligned} \tag{5.31}$$

with corresponding energies $E_\pm = \pm\sqrt{|\kappa_1|^2 + |\kappa_2|^2}$ and $E_D = 0$. Therefore, this system has a single state, $|D\rangle$, which has no contribution from the excited state. This state is robust against spontaneous decay, and we will refer to it as the dark state. We can write the eigenstates of the atom-light coupling in a different form as

$$\begin{aligned} |\pm\rangle &= \frac{1}{\sqrt{2}} \left(|B\rangle \pm |e\rangle \right), \\ |D\rangle &= \frac{1}{\sqrt{1 + |\zeta|^2}} \left(|g_1\rangle - \zeta^* |g_2\rangle \right), \end{aligned} \tag{5.32}$$

with $\zeta = \kappa_1/\kappa_2$ and

$$|B\rangle = \frac{1}{\sqrt{1 + |\zeta|^2}} \left(\zeta |g_1\rangle + |g_2\rangle \right). \tag{5.33}$$

This alternative form will prove helpful when determining the magnetic field and geometric scalar potential.

From Sec. 5.1 and restoring the $\mathbf{r}$-dependence of the dressed states due to the Rabi frequency we can derive the synthetic vector and scalar potential. We know that if we adiabatically prepare the atoms in the dark dressed state, with the state described by $|\Psi(\mathbf{r})\rangle = \psi_D(\mathbf{r})|D(\mathbf{r})\rangle$, then the equation of motion will be given by

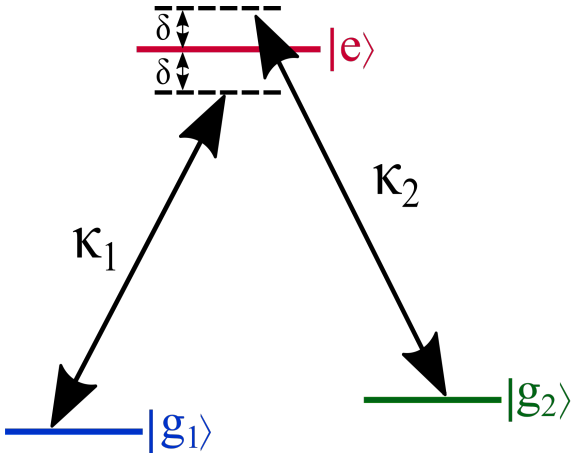

Figure 5.1: Illustration of the Λ-scheme, with internal atomic energy levels $|e\rangle$, $|g_1\rangle$ and $|g_2\rangle$ coupled by lasers κ_1 and κ_2 and with a detuning of δ.

the time-dependent Schrödinger equation

$$i\hbar\frac{\partial}{\partial t}\psi_D(\mathbf{r}) = \left[\frac{(\mathbf{p}-\mathcal{A}(\mathbf{r}))^2}{2m} + \mathcal{W}(\mathbf{r}) + V(\mathbf{r})\right]\psi_D(\mathbf{r}), \tag{5.34}$$

with $V(\mathbf{r})$ the trapping potential and

$$\mathcal{A}(\mathbf{r}) = i\hbar\langle D(\mathbf{r})|\nabla D(\mathbf{r})\rangle, \tag{5.35}$$

and

$$\mathcal{W}(\mathbf{r}) = \frac{\hbar^2}{2m}|\langle B(\mathbf{r})|\nabla D(\mathbf{r})\rangle|^2, \tag{5.36}$$

being the vector and scalar potential due to the spatial dependence of the dark state. Note, $\psi_D(\mathbf{r})$ gives the translational motion of the atoms in the dark states. This equation of motion is equivalent to that of a charged particle in a magnetic field of $\mathcal{B}(\mathbf{r}) = \nabla\times\mathcal{A}(\mathbf{r})$. Note, we are neglecting the scalar potential which arises from the time-dependence of the dressed states, as we are assuming there is no time-dependence in the atom-light coupling, and that the atomic state remains adiabatically in the dark dressed state.

By using the eigenstates as defined by Eq. (5.31), we find that the vector potential can be given by

$$\mathcal{A}(\mathbf{r}) = \frac{i\hbar(\kappa_1\nabla\kappa_1^* + \kappa_2\nabla\kappa_2^* - \kappa_1^*\nabla\kappa_1 - \kappa_2^*\nabla\kappa_2)}{2(|\kappa_1|^2 + |\kappa_2|^2)}, \tag{5.37}$$

where we have dropped the $\mathbf{r}$-dependence of the Rabi frequency. However, it is a long algebraic exercise to use this form of the dressed states to obtain the magnetic field and scalar potential. It is more straight-forward to consider the dressed states

in the form of Eq. (5.32), with the vector potential now given by

$$\mathcal{A}(\mathbf{r}) = i\hbar\frac{\zeta\nabla\zeta^* - \zeta^*\nabla\zeta}{2(1+|\zeta|^2)}, \tag{5.38}$$

a corresponding magnetic field of

$$\mathcal{B}(\mathbf{r}) = i\hbar\frac{\nabla\zeta\times\nabla\zeta^*}{(1+|\zeta|^2)^2}, \tag{5.39}$$

and a geometric scalar potential of

$$\mathcal{W}(\mathbf{r}) = \frac{\hbar^2}{2m}\frac{\nabla\zeta^*\cdot\nabla\zeta}{(1+|\zeta|^2)^2}. \tag{5.40}$$

At this point, it may appear rather arbitrary that we have derived two different forms of the vector potential. However, the vector potential is only defined up to a gradient, which would leave the magnetic field and scalar potentials unaffected. When considering the linked and knotted magnetic fields, we will find that the vector potential as defined by Eq. (5.38) is singular, whereas that defined by Eq. (5.37) is not. Therefore, to define a non-singular vector potential we will define $\mathcal{A}(\mathbf{r})$ in terms of Eq. (5.37). We will use the magnetic field and scalar potential as stated above in terms of ζ.

To ensure the adiabatic approximation utilised above is valid, the lifetime of the dressed state needs to be long enough to allow for the equation of motion of Eq. (5.34) to be experimentally realised. This requires some care on the part of the experimentalist: (i) Spontaneous emissions from the excited dressed state can be avoided if the Rabi frequency is large enough. (ii) Interactions also need to be avoided, as any atom-atom interactions would be detrimental to the stability of the dark state. (iii) Any Zeeman coupling terms that can exist between the two internal energy level ground states need to be small enough to allow them to be neglected.

5.3 Linked and knotted magnetic fields

We now need to define what we mean by linked and knotted magnetic fields. We will define a knotted magnetic field by a three-dimensional field which has lines which are knotted. The same argument is extended for the linked magnetic field, with it possessing linked field lines. Rañada proposed a systematic mathematical construction of these topologically non-trivial magnetic fields in the late 1980s [250, 251]. This approach has a geometrical interpretation in terms of the geometry of the 2-sphere which we will describe here. The details of this description in terms of geometry was developed in collaboration with Calum Ross and Bernd J. Schroers of the Mathematics department at Heriot-Watt University. We will first define some

concepts from differential geometry, and then we will derive the form of linked and knotted magnetic fields in Sec. 5.3.2.

5.3.1 Useful definitions from differential topology

5.3.1.1 Maps

The construction of the topological magnetic fields is based on rational maps. Maps are generalisations of functions, and here we will consider maps between manifolds. An n-dimensional manifold is defined as a topological space that is locally within a continuous transformation to the n-dimensional Euclidean space [109]. A good example of a manifold is the torus, where each point lies on a curved disk which can be continuously flattened into a disk in the plane. However, for example, the three-dimensional form of a cone is not a manifold, as the point at the end of the cone does not look like a small piece of any Euclidean plane [110]. A map f between two manifolds, e.g. from $G_1 \subset \mathbb{R}^m$ to $G_2 \subset \mathbb{R}^n$ is given by a function of m variables

$$y^n = f\left(x^1, \ldots, x^m\right), \tag{5.41}$$

where $(x^1, \ldots, x^m)$ runs over G_1 and $(y^1, \ldots, y^n)$ runs over G_2 [109]. We will write this map in the notation of $f : \mathbb{R}^m \to \mathbb{R}^n$. A rational map is defined as a map with

$$f\left(x^1, \ldots, x^m\right) = \frac{g\left(x^1, \ldots, x^m\right)}{h\left(x^1, \ldots, x^m\right)}, \tag{5.42}$$

where g and h are themselves polynomials, and they are useful for defining maps between $\mathbb{R}^3$ and S^2 [150].

5.3.1.2 Preimage

For a map $f : A \to B$, with $C \subseteq B$, the preimage of C under f is given as

$$f^{-1}(C) = \{a \in A \mid f(a) \in C\}. \tag{5.43}$$

The preimage is not the inverse of the map which is closer to the definition of a pullback. The preimage provides the points of the map that leads to the subset C.

5.3.1.3 Pullback

If $f : M \to \tilde{M}$ is a smooth map with x a point in M, then a tensor at the point $f(x) \in M$ can be pulled back to a tensor $\tilde{A}$ at $x \in M$. Now, if a field of tensors is defined on $\tilde{M}$, then we can pullback the tensor at each point $y \in \tilde{M}$ to a tensor at each point $f^{-1}(y)$, obtaining a new tensor field defined on M. This pullback of the field A is defined as f^*A [109]. Note, that in order to use this star notation for the

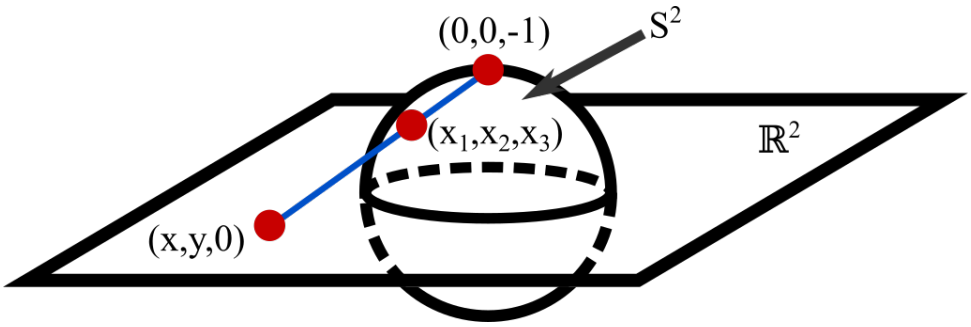

Figure 5.2: Illustrative example of stereographic projection from the south pole of a 2-sphere, S^2, to the two-dimensional plane of $\mathbb{R}^2$.

pullback, we will denote the complex conjugate of a complex number c within this section as $\bar{c}$.

5.3.1.4 Stereographic projection

In the course of defining the topological magnetic fields, we will utilise stereographic projections. Stereographic projection is a map between an n-sphere, S^n, with one point removed to the plane $\mathbb{R}^n$. It is simplest to think of this as a map $S \to \mathbb{R}$. In this case for each point A on the circle, except the omitted point P, we draw a line between P and A and label the intersection of this line with $\mathbb{R}$ as A', this map is then defined as $A \mapsto A'$ [109, 110]. We show a different illustrative example of the stereographic projection for $S^2 \to \mathbb{R}^2$ in Fig. 5.2.

5.3.2 Geometric description of topological magnetic fields

The construction of topological magnetic fields considered by Rañada is in terms of a map $f : \mathbb{R}^3 \to S^2$. This construction can be stated in terms of differential forms and pullbacks to show the coordinate-independent nature of their formulation.

5.3.2.1 Area element

We begin by considering the area element of the 2-sphere (S^2) which we will denote as Ω and is a 2-form. Performing the integration over the area element of S^2, we can set

$$\int_{S^2} \Omega = 1, \tag{5.44}$$

which is fixing a normalisation of the area of the 2-sphere. We will also fix the radius of S^2 to one. We can further write this integral in terms of the stereographically projected coordinates of $\mathbb{R}^2$ as

$$\int_{S^2} \Omega = \int_{\mathbb{R}^2} \Omega + \int_{\text{point}} \Omega = \int_{\mathbb{R}^2} \Omega, \tag{5.45}$$

where the second term is the integral over the single point removed from the 2-sphere, which is trivially zero. The 2-sphere is defined by

$$S^2 = \{(x_1, x_2, x_3) \in \mathbb{R}^3, x_1^2 + x_2^2 + x_3^2 = 1\}, \tag{5.46}$$

and we will set the plane of $\mathbb{R}^2$ to be at $x_3 = 0$, as illustrated in Fig. 5.2. We will define the coordinates of $\mathbb{R}^2$ to be given by a single complex number $\mathcal{Z} = x + iy$.

We know that the area element of the 2-sphere can be written as [252]

$$\int_{S^2} \Omega = \frac{1}{4\pi} \int_{S^2} (x_1 dx_2 dx_3 - x_2 dx_3 dx_1 + x_3 dx_1 dx_2)\,. \tag{5.47}$$

As we have set $x_1^2 + x_2^2 + x_3^2 = 1$, we have also that

$$x_1 dx_1 + x_2 dx_2 + x_3 dx_3 = 0, \tag{5.48}$$

this can be used to eliminate dx_3 from Ω to obtain

$$\int_{S^2} \Omega = \frac{1}{4\pi} \int_{S^2} \frac{dx_1 dx_2}{x_3}. \tag{5.49}$$

5.3.2.2 Stereographic projection

The stereographic projection from the south pole $(0, 0, -1)$ maps S^2 to $\mathbb{R}^2$, while sending the south pole to the point at infinity. We want to find the inverse stereographic projection which will map $g : \mathbb{R}^2 \to S^2$. The line through $(0, 0, -1)$ and $(x, y, 0)$ has a parametric equation of $(0, 0, -1) + t(x, y, 1)$, which intersects the unit 2-sphere when

$$t^2 x^2 + t^2 y^2 + (t - 1)^2 = 1. \tag{5.50}$$

The stereographic projection $S^2 \to \mathbb{R}^2$ is defined by [109]

$$(x_1, x_2, x_3) \mapsto (x, y) = \left(\frac{x_1}{1 + x_3}, \frac{x_2}{1 + x_3}\right). \tag{5.51}$$

Then if we find $x^2 + y^2$ then rearrange we can obtain

$$x_3 = \frac{1 - r^2}{r^2 + 1}, \tag{5.52}$$

with $r^2 = x^2 + y^2$. We know that $x_1 = x(1 + x_3)$ and $x_2 = y(1 + x_3)$ and can find each by substituting in the above defined x_3. This gives the inverse stereographic map to be [252]

$$\mathcal{Z} = x + iy \mapsto \left(\frac{2x}{1 + r^2}, \frac{2y}{1 + r^2}, \frac{1 - r^2}{1 + r^2}\right) = (x_1, x_2, x_3). \tag{5.53}$$

Using this map, it can be obtained that the integral over the area element is given by

$$\int_{S^2} \Omega = \frac{1}{2\pi i} \int_{\mathbb{R}^2} \frac{d\bar{\mathcal{Z}} d\mathcal{Z}}{\left(1 + |\mathcal{Z}|^2\right)^2}. \tag{5.54}$$

5.3.2.3 Removing the integral

The removal of the integration signs in Eq. (5.54) is a rather hard concept without getting too involved in the fundamental concepts of differential topology. However, we will attempt to motivate this here.

Under the integral sign we have $d\bar{\mathcal{Z}} d\mathcal{Z}$, if we write $d\mathcal{Z} = dx + idy$ then

$$d\bar{\mathcal{Z}} d\mathcal{Z} = (dx)^2 + (dy)^2 - 2idxdy. \tag{5.55}$$

It is difficult to think of any way the integral $(dx)^2$ could be valid in two-dimensions, integrating over x twice does not make sense. Therefore, we can write in effect that

$$d\bar{\mathcal{Z}} d\mathcal{Z} = -2idxdy, \tag{5.56}$$

which is equivalent to

$$d\bar{\mathcal{Z}} \wedge d\mathcal{Z} = -2idxdy, \tag{5.57}$$

where $\wedge$ is the wedge product, the antisymmetric part of the tensor product defined as

$$A \wedge B = \frac{1}{2} \left(A \otimes B - B \otimes A \right), \tag{5.58}$$

with $\otimes$ the tensor product. We can then write that

$$\int d\bar{\mathcal{Z}} d\mathcal{Z} = \int d\bar{\mathcal{Z}} \wedge d\mathcal{Z} \tag{5.59}$$

and then

$$\Omega = \frac{1}{2\pi i} \frac{d\bar{\mathcal{Z}} \wedge d\mathcal{Z}}{\left(1 + |\mathcal{Z}|^2\right)^2}. \tag{5.60}$$

This form of the area element is closed, with $d\Omega = 0$, and normalised to unit area. In its current form, Ω is defined as a tensor field on S^2.

5.3.2.4 Pullback of the area element

Given a map $f : \mathbb{R}^3 \to S^2$, the map is

$$(x_1, x_2, x_3) \mapsto f(x_1, x_2, x_3) = \mathcal{Z}, \tag{5.61}$$

in essence, the map is defined as $\mathbb{R}^3 \to S^2$ but is given by the function $f(x_1, x_2, x_3)$. Therefore, if we want to pullback the area element Ω to be a tensor field on $\mathbb{R}^3$ then we must replace all $\mathcal{Z}$ by the function $f(x_1, x_2, x_3)$. The pullback of Ω is then given

by

$$f^*\Omega = \frac{1}{2\pi i}\frac{df^* \wedge df}{(1+|f|^2)^2}. \tag{5.62}$$

This pullback is automatically closed, $d(f^*\Omega) = 0$, as the pullback commutes with the exterior derivative. However, this is still defining a tensor field, and we wish to obtain a magnetic field which is a vector field.

5.3.2.5 Writing the tensor field as a vector field

We will not consider the exact details of transforming Eq. (5.62) into a vector field. This involves some rather complex topics of differential topology including the Hodge star operator, which maps k-vectors to $(n-k)$-vectors for an n-dimensional vector space [109, 253, 254].

By using the metric and volume element associated with Euclidean space the pullback can be written as a vector field of [242]

$$\mathbf{B} = \frac{1}{2\pi i}\frac{\nabla \bar{f} \times \nabla f}{(1+|f|^2)^2}, \tag{5.63}$$

which defines our magnetic field in three-dimensional Euclidean space. Note, that due to the closure of $f^*\Omega$, the defined magnetic field satisfies $\nabla \cdot \mathbf{B} = 0$, i.e. the static Maxwell equations with a general non-trivial current. The formulation of the magnetic field given by Eq. (5.63), along with the definition of the maps, has been utilised in several publications to study topologically non-trivial vector fields [153, 158, 160–162, 255].

5.3.2.6 The map

The maps we have considered so far are truly compositions and can be defined as

$$f : \mathbb{R}^3 \to S^3 \to S^3 \to S^2, \tag{5.64}$$

where the $\mathbb{R}^3 \to S^3$ is a stereographic projection, $S^3 \to S^3$ is a map to polynomials, and $S^3 \to S^2$ is a Hopf map.

We can consider S^3 as being given by $|u|^2 + |v|^2 = l^2$ with u and v being the complex coordinates of S^3, whereas S^2 can be given as a complex projective line ($\mathbb{C}$ with a single point at infinity added) [109]. This complex projective line is also known as the Riemann sphere and is illustrated in Fig. 5.3. The complex line has one dimension over the complex coordinate space $\mathbb{C}$ but has two dimensions in the real coordinate space $\mathbb{R}$, therefore, the complex line is topologically equivalent to a plane in $\mathbb{R}$. Then the Hopf map is between $(u, v) \in S^3$ to the point of the complex projective with homogeneous coordinates (u, v). The Hopf map then takes

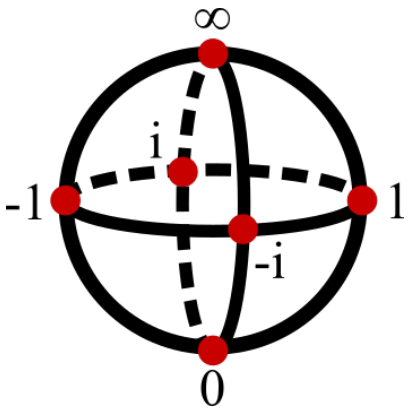

Figure 5.3: Illustration of the Riemann sphere, or the complex projective line with the point at infinity added.

the ratio of the complex coordinates of S^3 to define a single complex number for the coordinates of the complex projective line.

The Hopf invariant, or number, is a linking number associated to the homotopy class of maps between spheres [109, 252, 256]. Homotopy classes define topological spaces that have the same shape. Taking a point $a \in S^2$ of the map $\tilde{f} : S^3 \to S^2$, then the preimage $\tilde{f}^{-1}(a)$ will be a collection of closed curves. The Hopf invariant of $\tilde{f}$ is then defined by the linking number of two non-intersecting closed curves $\tilde{f}^{-1}(a)$ and $\tilde{f}^{-1}(b)$, where a and b are distinct regular points on S^2 [109].

Using the complex notation for S^3, the inverse stereographic projection maps $(x, y, z) \in \mathbb{R}^3$ to [242, 257]

$$u = \frac{2l^2\,(x + iy)}{l^2 + r^2}, \quad v = \frac{2l^2 z + il\,(r^2 - l^2)}{l^2 + r^2}, \tag{5.65}$$

where $r^2 = x^2 + y^2 + z^2$ and l setting the unit of length (the size of S^3).

We can then write the full map in terms of coordinate transformations as

$$\begin{aligned}(x, y, z) &\mapsto \Big(u(x, y, z), v(x, y, z)\Big) \\ &\mapsto \Big(g\Big(u(x, y, z), v(x, y, z)\Big), h\Big(u(x, y, z), v(x, y, z)\Big)\Big) \\ &\mapsto \frac{g\Big(u(x, y, z), v(x, y, z)\Big)}{h\Big(u(x, y, z), v(x, y, z)\Big)},\end{aligned} \tag{5.66}$$

where g and h are two complex polynomials of the same degree. The degree of the polynomials is related to the Hopf number of the map, with n^2 being the Hopf number for degree n polynomials [257]. Therefore, the topology of the map is characterised by the polynomials of the $S^3 \to S^3$ map. It is these polynomials that can be changed to define magnetic fields of different topology, e.g. links or knots.

Hence, the topology of the map (associated with the Hopf number) is contained within the $S^3 \to S^3$ part of the composition.

The rational map f then takes the form

$$f(x,y,z) = \frac{g\Big(u(x,y,z), v(x,y,z)\Big)}{h\Big(u(x,y,z), v(x,y,z)\Big)}, \tag{5.67}$$

with g and h being polynomials in u and v. Note, for this definition of the map to hold, g and h must not vanish at the same points. By our definition of the magnetic field, the nodal lines of the polynomial h will encode the form of the desired link or knot, and g encodes the desired helicity as observed in Ref. [162].

5.3.3 The three example topological fields

In this work, we will focus on three examples of topological magnetic fields:

1. The standard Hopf map with $f_H = u/v$ which defines Hopf circles for the magnetic field, i.e. each magnetic field line will be a circle which links once with every other field line.

2. The quadratic Hopf map with $f_L = u^2/(u^2 - v^2)$ which defines linked rings as the magnetic field lines.

3. The map $f_T = u^3/(u^3 + v^2)$ which defines a trefoil knot for the magnetic field lines.

Of these, the first two define magnetic fields which are topological in the sense that they have linked magnetic field lines. The final map defines a magnetic field which has lines that form a trefoil knot around the region defined by the sphere of radius l, i.e. not all the magnetic field lines are knotted.

5.4 The realisation of topological magnetic fields

We have so far constructed two magnetic fields of a similar form, the synthetic Λ-scheme field of

$$\mathcal{B} = i\hbar \frac{\nabla\zeta \times \nabla\zeta^*}{\left(1 + |\zeta|^2\right)^2}, \tag{5.68}$$

and a magnetic field defined via a map which can encode linked and knotted field lines of

$$\mathbf{B} = \frac{1}{2\pi i} \frac{\nabla f^* \times \nabla f}{\left(1 + |f|^2\right)^2}. \tag{5.69}$$

We have returned to the representation of the complex conjugate of a by a^*. If we identify

$$\zeta \equiv f, \tag{5.70}$$

then the two derived magnetic fields only differ by a scaling. As we are primarily interested in realising the form of linked and knotted magnetic fields, we can neglect the difference in scale. Therefore, to realise topological magnetic fields defined by a map f in an ultracold gas we can drive the internal atomic transitions of a Λ-scheme by two lasers which have spatial and phase profiles such that their ratio forms the map f.

As we are considering the ratio of the two laser beams, we have an amount of freedom in the selection of the form of each laser profile. In principle, the combination of two lasers should be able to realise any link or knot defined from the map. However, we cannot simply take the exact form of the map then equate this to the ratio and claim this can be realised as the lasers must fulfil the Maxwell equations or their paraxial approximations.

5.4.1 General realisation

As already stated, the nodal lines of the polynomial h define the topological form of the magnetic field. As $\zeta = \kappa_1/\kappa_2$, this means that we must realise in κ_2 an optical vortex of the form of the desired topology. Linked and knotted optical vortex lines have already been realised by a suitable superposition of Laguerre-Gaussian (LG) modes [258–260]. These superpositions can be constructed entirely optically and usually utilise spatial light modulators [261–267]. The LG superposition is constructed through optical means and the light beam defined by the superposition is used to drive the relevant internal atomic transition.

LG beams are defined by [268]

$$\begin{aligned}\mathcal{L}_{pn}(\rho,\phi,z) =& \frac{C}{\sqrt{1+\frac{z^2}{z_R^2}}}\left(\frac{\rho\sqrt{2}}{w(z)}\right)^{|n|} L_p^{|n|}\left(\frac{2\rho^2}{w^2(z)}\right)\exp\left[-\frac{\rho^2}{w^2(z)}\right] \\ & \times\exp\left[-\frac{ik\rho^2 z}{2(z^2+z_R^2)} - in\phi + i(2p+|n|+1)\arctan\frac{z}{z_R}\right],\end{aligned} \tag{5.71}$$

with (ρ,ϕ,z) defining the cylindrical coordinate system, n the azimuthal index giving the orbital angular momentum, p the radial index, C a normalisation constant, and $L_p^{|n|}$ the associated Laguerre polynomials. The LG mode is characterised by the p and n indices which must be integers. We will use the usual definitions of the Rayleigh range $z_R = \pi\omega_0^2/\lambda$ and beam waist $w(z) = \omega_0\sqrt{1+(z/z_R)^2}$. It will be useful to write explicitly the LG mode at $z = 0$ in a different notation

$$\mathcal{L}_{pn}(\rho,\phi,0) = \frac{\tilde{C}}{w_0}e^{-\frac{\rho^2}{w_0^2}}L_p^n\left(\frac{2\rho^2}{w_0^2}\right)\left(\frac{x-iy}{w_0}\right)^n, \tag{5.72}$$

where we have utilised the fact that

$$\rho^n \exp(-in\phi) = (x - iy)^n. \tag{5.73}$$

A useful method to characterise the topological magnetic fields considered in this work is to consider the level curves. The level curves are defined by the complex condition $|f| =$ constant or $|\zeta| =$ constant. These level curves define surfaces on which the magnetic field lines must exist. Therefore, these surfaces need to be of the same topology as the magnetic field lines.

We will state here the method of constructing the superposition of LG beams for a general form of the linked and knotted field, and we will motivate this after the fact by utilising it for the three examples. The method employed for constructing the topological magnetic fields via the Λ-scheme is adapted from that of generating linked and knotted optical vortices [258] and consists of the following steps:

1. Start from the map $f = g/h$ defining the topological magnetic field, then restrict the map to the $z = 0$ plane. In this case, z is the propagation direction of the laser beam. This results in a map in terms of a ratio of polynomials g and h in x and y.

2. Expand the restricted polynomials g and h in terms of the complete set of LG modes, note common factors can be neglected when expanding the polynomials

3. Write the new map in terms of the LG mode expansions, and allow the LG modes to take their usual z-dependence. This map in terms of the LG modes then characterises the ratio of the driving laser beams, i.e. ζ.

4. Check numerically that the level curves of ζ (the ratio of the LG modes) have the same topology as the level curves of the original f.

5. If the topology has been retained with the LG mode expansion, then the derived driving can be utilised experimentally to realise the topological magnetic field synthetically with the Λ-scheme.

We will see that this approach works for all three examples considered here. There is no mathematical proof that this method will work in general for all known knots and links.

5.4.2 Realisation of the three example fields

First, we will find it useful to state some of the LG modes utilised for the expansions of the three topological magnetic fields at $z = 0$. These are:

$$\begin{aligned}
\mathcal{L}_{0n} =& \exp\left(-\frac{\rho^2}{\omega_0^2}\right)\left(\frac{x-iy}{\omega_0}\right)^n, \\
\mathcal{L}_{1n} =& \exp\left(-\frac{\rho^2}{\omega_0^2}\right)\left(\frac{x-iy}{\omega_0}\right)^n\left[(n+1)-\frac{2\rho^2}{\omega_0^2}\right], \\
\mathcal{L}_{2n} =& \exp\left(-\frac{\rho^2}{\omega_0^2}\right)\left(\frac{x-iy}{\omega_0}\right)^n\left[\frac{(n+1)(n+2)}{2}-(n+2)\frac{2\rho^2}{\omega_0^2+\frac{2\rho^4}{\omega_0^4}}\right], \\
\mathcal{L}_{3n} =& \exp\left(-\frac{\rho^2}{\omega_0^2}\right)\left(\frac{x-iy}{\omega_0}\right)^n\left[\frac{(n+3)(n+2)(n+1)}{3!}-(n+3)(n+2)\frac{\rho^2}{\omega_0^2}\right. \\
&\left.+(n+3)\frac{2\rho^4}{\omega+0^4}-\frac{4\rho^6}{3\omega_0^3}\right],
\end{aligned} \tag{5.74}$$

note, we have neglected constant factors of normalisation of each term. We can also define a new complex notation in terms of x and y for the polynomials as

$$\begin{aligned}
\tilde{u} =& \frac{2}{l}(x-iy), \\
\tilde{v} =& i\left(\frac{\rho^2}{l^2}-1\right).
\end{aligned} \tag{5.75}$$

With this notation we can write the three considered maps for $z = 0$ as

$$\begin{aligned}
f_H\,|_{z=0} =& \frac{u}{v} = \frac{\bar{\tilde{u}}}{\tilde{v}}, \\
f_L\,|_{z=0} =& \frac{u^2}{u^2-v^2} = \frac{\bar{\tilde{u}}^2}{\bar{\tilde{u}}^2-\tilde{v}^2}, \\
f_T\,|_{z=0} =& \frac{u^3}{u^3+v^2} = \frac{\bar{\tilde{u}}^3}{\bar{\tilde{u}}^3+\left(1+\frac{\rho^2}{l^2}\right)\tilde{v}^2},
\end{aligned} \tag{5.76}$$

where we have used $\bar{a}$ to represent the complex conjugate and the extra factor in front of $\tilde{v}^2$ in the map leading to the trefoil is due to the difference in power in the denominator.

Now, knowing all the powers of $\tilde{u}$ and $\tilde{v}$ we can construct each independently in

terms of LG modes:

$$\begin{aligned}
\tilde{u}^n =& \exp\left(\frac{\rho^2}{\omega_0^2}\right)(2\alpha)^n \mathcal{L}_{0n},\\
\tilde{v} =& i\exp\left(\frac{\rho^2}{\omega_0^2}\right)\left[\left(-1+\frac{\alpha^2}{2}\right)\mathcal{L}_{00}-\frac{\alpha^2}{2}\mathcal{L}_{10}\right],\\
\tilde{v}^2 =& \exp\left(\frac{\rho^2}{\omega_0^2}\right)\left[\left(-1+\alpha^2-\frac{\alpha^4}{2}\right)\mathcal{L}_{00}\left(\alpha^4-\alpha^2\right)\mathcal{L}_{10}-\frac{\alpha^4}{2}\mathcal{L}_{20}\right], \quad (5.77)\\
\left(1+\frac{\rho^2}{l^2}\right)\tilde{v}^2 =& \exp\left(\frac{\rho^2}{\omega_0^2}\right)\left[\left(-1+\frac{\alpha^2}{2}+\frac{\alpha^4}{2}-\frac{3\alpha^6}{4}\right)\mathcal{L}_{00}\right.\\
&\left.+\left(\frac{\alpha^2}{2}-\alpha^4+\frac{9\alpha^6}{4}\right)\mathcal{L}_{10}+\left(\frac{\alpha^4}{2}-\frac{9\alpha^6}{4}\right)\mathcal{L}_{20}+\frac{3\alpha^6}{4}\mathcal{L}_{30}\right],
\end{aligned}$$

where we have defined $\alpha = \omega_0/l$. Therefore, to realise the three topological magnetic fields we only require up to an $\mathcal{L}_{30}$ mode in the superposition.

5.4.2.1 Hopf circles

For the Hopf circles, we have the standard Hopf map, where we have already stated that $f_H\ |_{z=0}= \bar{\tilde{u}}/\tilde{v}$. Therefore, the expansion method finds that for the Hopf circle magnetic fields the lasers should have a profile such that their ratio is

$$\zeta_H = \frac{2\alpha\mathcal{L}_{0-1}}{i\left[\left(\frac{\alpha^2}{2}-1\right)\mathcal{L}_{00}-\frac{\alpha^2}{2}\mathcal{L}_{10}\right]}, \quad (5.78)$$

note, the i factor on the denominator is only a constant phase shift. Therefore, one choice is to generate the two laser beams so that

$$\begin{aligned}
\kappa_1 &= 2\alpha\mathcal{L}_{0-1},\\
\kappa_2 &= e^{3\pi/2}\left[\left(\frac{\alpha^2}{2}-1\right)\mathcal{L}_{00}-\frac{\alpha^2}{2}\mathcal{L}_{10}\right].
\end{aligned} \quad (5.79)$$

5.4.2.2 Linked rings

For the linked rings, we have the quadratic Hopf map, where we have already stated that $f_L\ |_{z=0}= \bar{\tilde{u}}^2/(\bar{\tilde{u}}^2-\tilde{v}^2)$. The expansion method finds that the linked rings magnetic field should be realised if the lasers have profiles such that their ratio is

$$\zeta_L = \frac{(2\alpha)^2\mathcal{L}_{0-2}}{(2\alpha)^2\mathcal{L}_{0-2}-\left(-\frac{\alpha^4}{2}+\alpha^2-1\right)\mathcal{L}_{00}-\left(\alpha^4-\alpha^2\right)\mathcal{L}_{10}+\frac{\alpha^4}{2}\mathcal{L}_{20}}. \quad (5.80)$$

Therefore, one choice is to generate the two laser beams so that

$$\begin{aligned}
\kappa_1 &= (2\alpha)^2\mathcal{L}_{0-2},\\
\kappa_2 &= (2\alpha)^2\mathcal{L}_{0-2}-\left(-\frac{\alpha^4}{2}+\alpha^2-1\right)\mathcal{L}_{00}-\left(\alpha^4-\alpha^2\right)\mathcal{L}_{10}+\frac{\alpha^4}{2}\mathcal{L}_{20}.
\end{aligned} \quad (5.81)$$

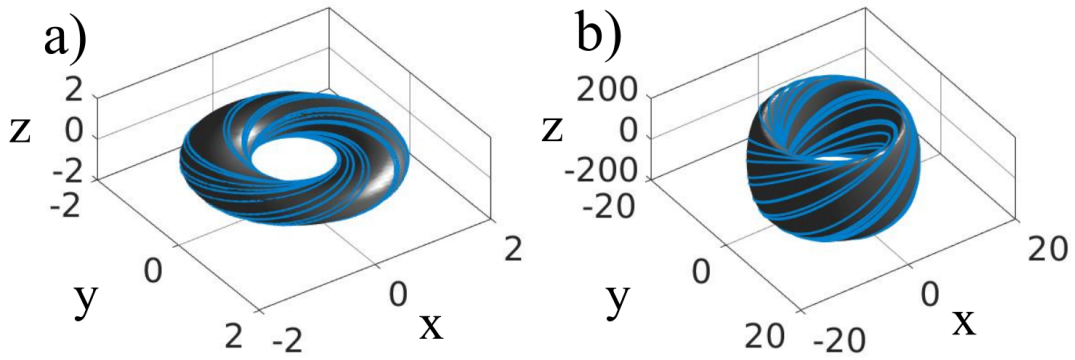

Figure 5.4: Exact and approximated magnetic field lines for Hopf circles. The magnetic field is realised as level curves of the complex field f and its Laguerre-Gauss approximation ζ. We show level surfaces of $|f|$ and $|\zeta|$, and, on each level surface, we show a selection of magnetic field lines in light blue. Magnetic fields for the a) exact Hopf circles (f_H) and b) realised Hopf circles (ζ_H). The unit of length for the exact magnetic fields (a) is l, and for the realised fields (b) it is the laser wavelength λ with $\alpha = 100$.

5.4.2.3 Trefoil knot

For the trefoil knot, we have a map such that

$$f_L\,|_{z=0} = \frac{\bar{\tilde{u}}^3}{\bar{\tilde{u}}^3 + \left(1 + \frac{\rho^2}{l^2}\right)\tilde{v}^2}. \tag{5.82}$$

The expansion method for the trefoil knot gives a ratio for the laser profiles of

$$\zeta = \frac{(2\alpha)^3 \mathcal{L}_{0-3}}{(2\alpha)^3 \mathcal{L}_{0-3} + \frac{1}{4}\left[c_0 \mathcal{L}_{00} + c_1 \mathcal{L}_{10} + \left(2\alpha^4 - 9\alpha^6\right)\mathcal{L}_{20} + 3\alpha^6 \mathcal{L}_{30}\right]}, \tag{5.83}$$

with

$$\begin{aligned} c_0 &= \left(-4 + 2\alpha^2 + 2\alpha^4 - 3\alpha^6\right), \\ c_1 &= \alpha^2\left(-2 - 4\alpha^2 + 9\alpha^4\right). \end{aligned} \tag{5.84}$$

Therefore, one choice is to realise the laser profiles such that

$$\begin{aligned} \kappa_1 &= (2\alpha)^3 \mathcal{L}_{0-3}, \\ \kappa_2 &= (2\alpha)^3 \mathcal{L}_{0-3} + \frac{1}{4}\left[c_0 \mathcal{L}_{00} + c_1 \mathcal{L}_{10} + \left(2\alpha^4 - 9\alpha^6\right)\mathcal{L}_{20} + 3\alpha^6 \mathcal{L}_{30}\right]. \end{aligned} \tag{5.85}$$

5.4.3 Comparison of exact and realised fields

Having utilised the expansion method to obtain the forms of the laser beams, we can now compare these realisable magnetic fields to the exact magnetic fields defined by the corresponding map. In Figs. 5.4, 5.5, and 5.6, we show a comparison between the three example exact and realisable magnetic fields. For all of the realised fields,

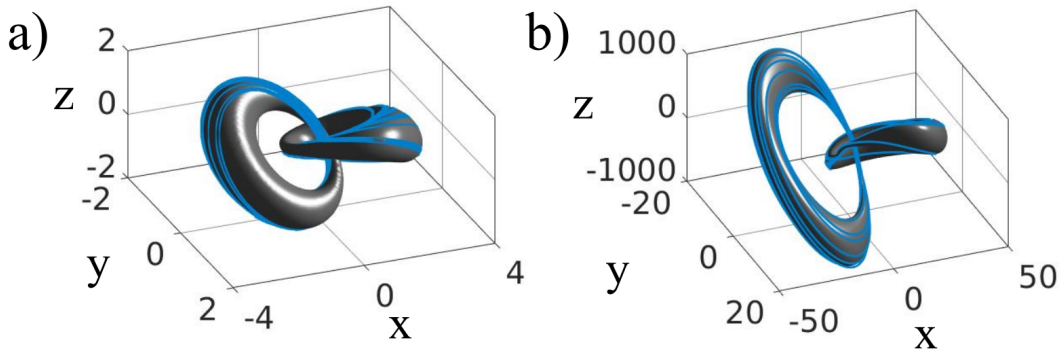

Figure 5.5: Same as Fig. 5.4 but for the case of the linked rings magnetic field lines. Magnetic fields for the a) exact linked rings (f_L) and b) realised linked rings (ζ_L).

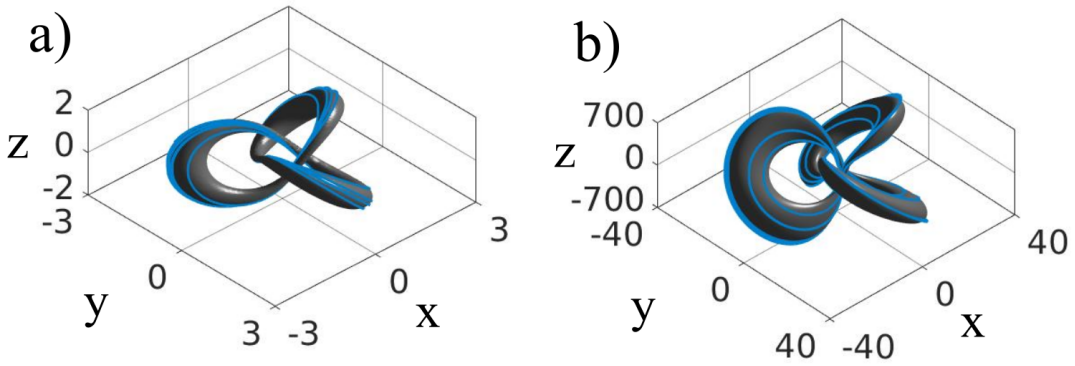

Figure 5.6: Same as Fig. 5.4 but for the case of the trefoil knot magnetic field lines. Magnetic fields for the a) exact trefoil knot (f_K) and b) realised trefoil knot (ζ_K).

we have chosen a beam width of $\alpha = 100\lambda$ and we will work in units of the laser wavelength λ. The exact magnetic fields are shown in units of the S^3 unit of length l.

We find that all three realisable synthetic magnetic fields retain the topology of the exact magnetic fields. However, each magnetic field is stretched out in z in comparison to the exact fields. This stretching is not surprising, as in optics it is easier to construct profile structures perpendicular to the propagation direction than in the direction of propagation. From the level curves, and magnetic field lines, shown in Figs. 5.4, 5.5, and 5.6, it is clear that the topology of the fields is shared.

5.4.4 Comments on experimental implementation of laser profiles

Having constructed laser profiles in terms of LG modes which generate synthetic magnetic fields of the correct topology, we can now discuss the potential experimental realisation of these superpositions briefly.

The atomic transitions of the Λ-scheme are in the optical regime, and thus a limiting factor for the length scales will be the diffraction limit of 0.2 μm− 0.4 μm. Also, the resolution of current beam shaping technology will impose further restrictions on the spatial resolution of the synthetic magnetic field and on its strength (which will be proportional to the beam intensity). The current limits of atomic cloud size are $\sim 100\mu$m [269], which is smaller than the usual beam waists considered of $\sim$ 1mm [270] for the optical vortex knots. However, it is not unusual in optics to focus optical beams down to beam waists of $50 - 200\mu$m in other settings [271, 272]. Therefore, we do not foresee the required beam shaping and focusing discussed here to be beyond the reach of current experimental techniques.

5.5 Ground states of a Bose condensate

We now turn to the behaviour of the ultracold gas under topological synthetic magnetic fields. For this, we consider a three-dimensional non-interacting gas of bosonic atoms, with the Hamiltonian

$$H = \frac{(p - \mathcal{A})^2}{2m} + \mathcal{W} + \frac{1}{2}m\omega^2\mathbf{r}^2, \tag{5.86}$$

where

$$\mathcal{A} = \frac{i\hbar(\kappa_1\nabla\kappa_1^* + \kappa_2\nabla\kappa_2^* - \kappa_1^*\nabla\kappa_1 - \kappa_2^*\nabla\kappa_2)}{2(|\kappa_1|^2 + |\kappa_2|^2)}, \tag{5.87}$$

and

$$\mathcal{W} = \frac{\hbar^2}{2m}\frac{\nabla\zeta^*\cdot\nabla\zeta}{(1+|\zeta|^2)^2}. \tag{5.88}$$

The atoms are trapped in a three-dimensional harmonic trap characterised by the trap frequency ω.

We are interested in obtaining the ground states of the condensate in Hamiltonian (5.86), with the vector and scalar potential being given by each of the three example maps considered. We will solve for the ground state, ψ, using imaginary time propagation [273–275], which is a standard technique in quantum problems. The numerics were performed on a uniform grid of 201^3 points (which is sufficient to consider the detailed properties of the wave function) and for the three exact magnetic fields defined via the maps f_H, f_L, and f_T. Note, the choice to use the exact over the realised magnetic fields is entirely one of convenience, having shown the magnetic fields are topologically the same, and any differences will only be in scale. We will work in the natural units of length of the harmonic potential of $s_0 = \sqrt{\hbar/m\omega}$ and take $l = 1$.

It is not immediately obvious what the properties of the ground states of this system should be. The exact form of the ground state is dependent on the interplay between the strength and geometry of the topologically non-trivial magnetic fields,

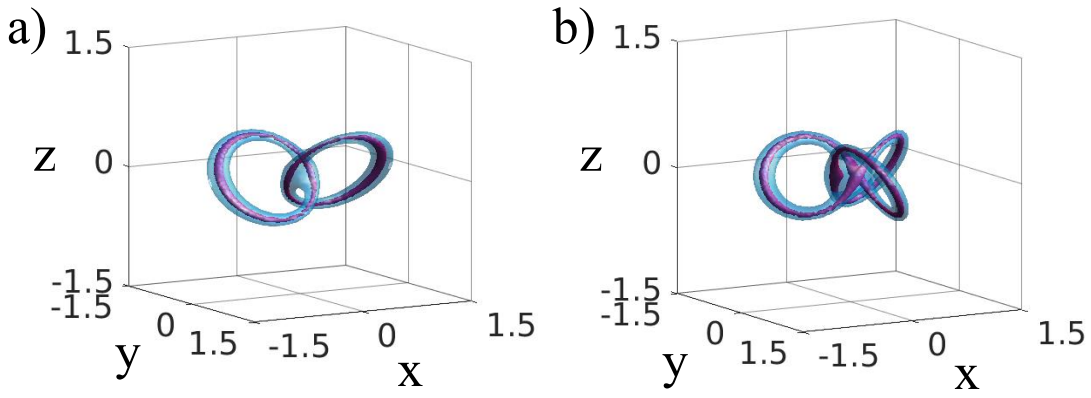

Figure 5.7: Vortex structure of the ground states of a trapped ultracold gas with a vector potential constructed from a) f_L and b) f_T. Shown are level sets of the probability density ($|\psi|^2$ = const.) for two small constants, which visualises the vortex core structure. The vortices form linked rings in a) and a trefoil knot in b), thus replicating the form of the magnetic field lines in both cases. Lengths are in units of s_0.

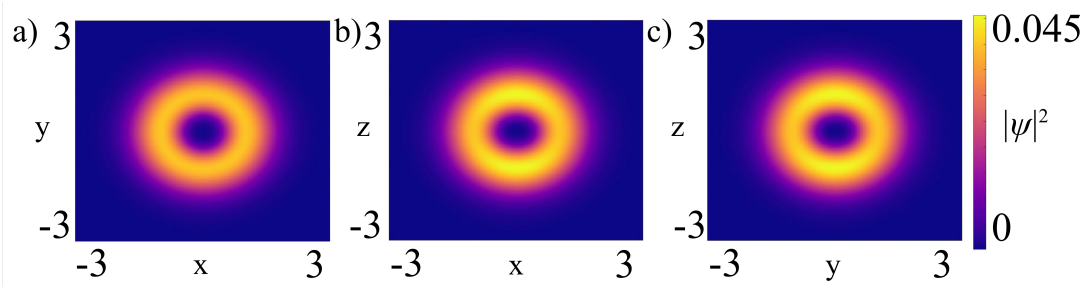

Figure 5.8: Ground state of a trapped ultracold gas with a vector potential constructed from f_H. The probability density is shown in the a) xy-plane ($z = 0$), b) xz-plane ($y = 0$) and c) yz-plane ($x = 0$). The ground state is real-valued and forms a shell structure which is close to spherical but slightly elongated in the z-direction. Note that the geometric potential Φ is spherically symmetric in this case, but the magnetic field is not. Lengths are in units of s_0.

the scalar potential, and the harmonic trap. The ground states shown and discussed here are the result of the choice of the trapping potential and the scale of the magnetic fields.

In the ground states obtained by imaginary time propagation for the linked rings and trefoil knot, we observe the presence of topological vortex structures. This is shown in Fig. 5.7 by the level curves of the probability density, $|\psi|^2$ = constant. However, for the Hopf circles magnetic field, we observe no vortex structure with instead an effective three-dimensional double well ground state, as shown in Fig. 5.8.

Next, we will briefly discuss the robustness of these ground states. The topology exhibited by these ground states is very different to the edge states discussed in the previous two chapters. The maxima of the scalar potential also exhibit level curves for near-maximal values that possess the topological structures of the magnetic fields

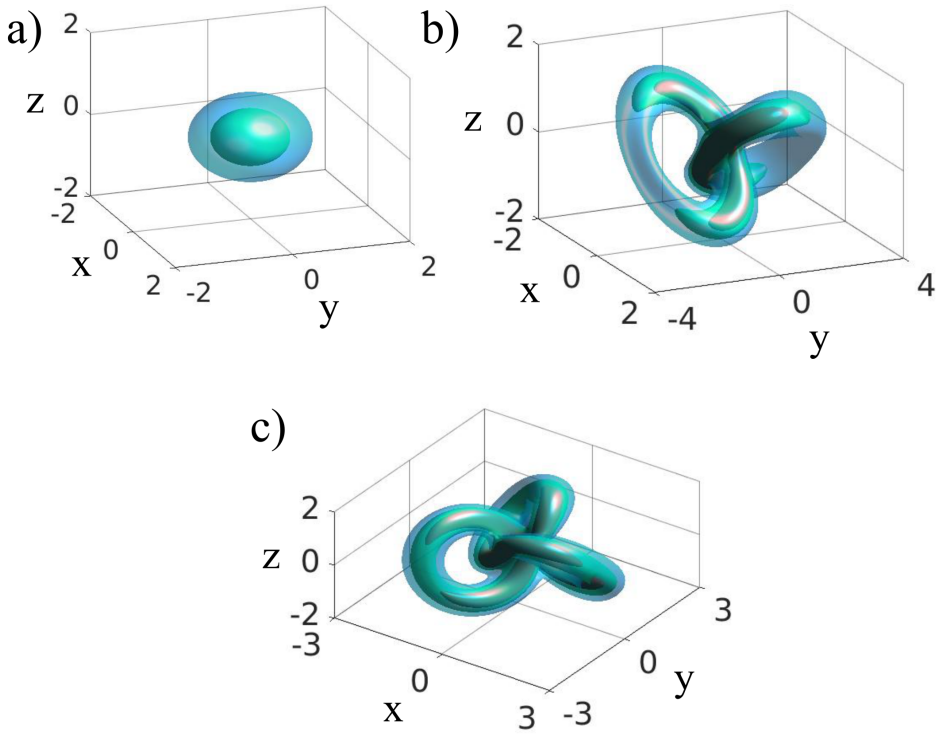

Figure 5.9: Maximal value level curves, $|\mathcal{W}|$ = constant, of the scalar potentials given by Eq. (5.40). For the maps of a) the Hopf circles, b) the linked rings, and c) the trefoil knot. The level curves show that the maximal points of the scalar potential can have a similar form to the topological magnetic fields. Each plot shows level curves for three (two for the Hopf circles) different constants, with the level curves for increasing constant being nested inside each other. Lengths are in units of s_0.

as shown in Fig. 5.9. When small potential impurities relative to the scalar potential are introduced, then we find the ground state to still be of the same form. However, these topological vortex structures depend on the magnetic field being present. If we allow the ground state to form, then turn off the magnetic field, then the vortex structure will be destroyed. This is shown in Fig. 5.10, where the initial state is taken as that of Fig. 5.7b then the state is propagated with the magnetic field switched off. We observe that the vortex structure is destroyed as expected, with the final state after propagation not containing a vortex knot.

5.6 Chapter summary

In this chapter, we have shown that topologically non-trivial synthetic magnetic fields can be realised in ultracold atomic gases. We have detailed a general method for the realisation of such magnetic fields and confirmed that three examples, the Hopf circles, linked rings, and trefoil knot, are realisable via a Λ-scheme of driving internal energy levels. It has also been shown that the pullback of the normal area

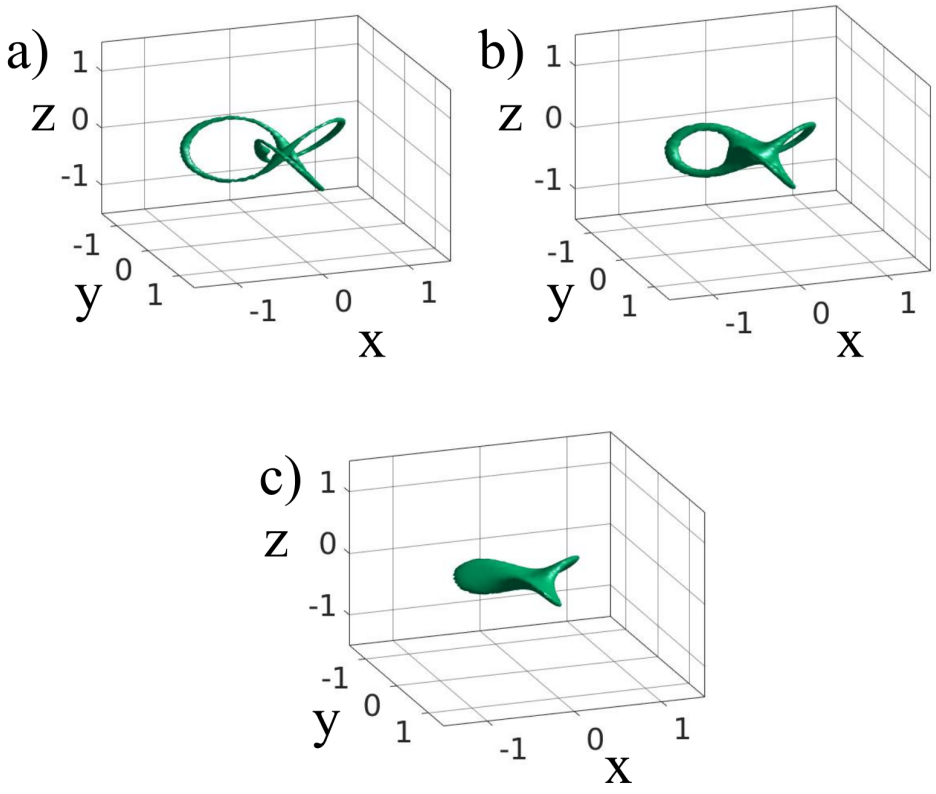

Figure 5.10: Minimal value level curves, $|\psi|^2 =$ constant, of the trefoil ground state wave function, seen in Fig. 5.7b, when the vector potential is removed and the state propagated under the Hamiltonian for a time t. All three plots show the same level curve of $|\psi|^2 = 10^{-4}$. Propagation times are a) $t = 0$, b) $t = 0.025$, and c) $t = 0.05$. Lengths are in units of s_0 and time in units of $1/\omega$.

element of a 2-sphere to three-dimensional Euclidean space is naturally equivalent to the synthetic magnetic field of the Λ-scheme. We have observed that the ground states of atoms in topological synthetic magnetic fields can reflect the topology by forming vortex links and knots. The expansion method utilised is not limited to the three examples considered, and it is possible for there to be other realisable topological magnetic fields of interest.

Chapter 6

Conclusion and outlook

The work contained in this thesis has been centred on the topic of topology in the setting of condensed matter and ultracold gases. In particular, we considered the cases of topological insulators and topologically non-trivial magnetic fields. For topological insulators, we have considered both static and driven models. When considering static topological insulators, we derived the wave functions, including edge states, for one-dimensional non-interacting models with arbitrary tunnelling and on-site energy. For driven topological insulators, we considered the influence of interactions upon both the classical and quantum case of a two-dimensional driven model which exhibits edge states in the non-interacting limit. In the final chapter, we proposed a scheme which realises linked and knotted synthetic magnetic field lines in an ultracold gas.

A large portion of this thesis has been dedicated to the discussion of the robustness of topological states of matter. We have found that for the case of topological insulators, the edge states are only robust up to a moderate perturbation of the model. This is not surprising as it is known that the edge states of topological insulators are robust only against weak perturbations. However, what is surprising is how small these moderate perturbations can be to cause a drastic change in the properties of the edge state. We have seen in Chapter 3 that for single-particle topological insulators, impurities with energies of the order of the band gap can destroy topological edge states. Also, it was observed that the commensurability of a finite lattice can play an important role for the number of edge states exhibited in the system and that the bulk-boundary correspondence is only applicable when there is an integer number of unit cells in the lattice. We also showed that if the system is quenched into one with an impurity the transition probabilities of edge states into the bulk can be significant. For the case of a driven topological insulator model, as considered in Chapter 4, it is simple to see that the edge state will still propagate even when impurities are introduced on the edge of the lattice. However, if interactions are introduced into the system, then the edge state can on average decay into the bulk. This was mainly shown by considering a hardcore interaction

in the classical limit but was confirmed for spinless fermions in small lattices. It is important to note that even for small fillings, the particle will still on average move into the bulk, but on a longer time scale when compared to that of a higher filling. For the case of topologically non-trivial magnetic fields, the linked and knotted vortex structures formed in the ground state are stable as long as the magnetic field is applied. We observed that when the magnetic field is switched off, the topological vortex structures are destroyed quite quickly.

The characterisation of the robustness of topological states of matter should not be viewed as a negative topic. We are not saying that the topological states discussed in this thesis are not robust. We are simply defining the parameter regions where they are robust. We have shown that care must be taken when simulating or fabricating topological insulators to ensure impurities of the order of the band gap are not present. This is especially important at the edge of the system, where impurities for one dimension and edge softening for two dimensions can drastically change the properties of edge states. In addition, the introduction of interactions into topological insulators can result in transport along the edge declining. Therefore, when considering single-particle topological insulators, it is important to avoid the introduction of any interaction terms between the particles.

Each of the first two chapters proposed a new technique which could be useful outside of its application here. In Chapter 3, we derived the exact wave functions for single-particle one-dimensional models. We applied this to study topological insulators and their robustness, but it can be used for any one-dimensional non-interacting lattice model. In Chapter 4, we showed that there exist special points in a driven model where the classical and quantum dynamics are the same and that within certain parameter regions the classical dynamics give a good approximation to the quantum result. Other periodically driven models could possess these special points as well, and their presence can allow for the fast simulation of the quantum model in certain limits.

In the final chapter, we showed a link between the topological magnetic fields derived in geometrical terms and the magnetic field of the Λ-scheme. The full meaning of this link and its physical relevance is still being considered, and it is too early to state if this link could be useful outside of its observation here. However, from this project, there are three main open questions that warrant further study. First, we currently have little understanding of the mechanism that allows the expansion method to work and when (or if) it would break down. As the expansion is not exact, we do not expect the proposed approach to work for all possible linked and knotted structures. However, it is difficult to predict the breakdown of the method without understanding the physical reason why this expansion works. Second, it could also be possible with this technique to start probing the motion group of links or knots [276, 277]. This group is not well understood on a mathematical level, as it

is relatively complicated, but the physical realisation of the group, e.g. pulling two knots through each other, could be useful in its future characterisation. It would be very interesting to consider the potential use of this motion group for topologically protected quantum computing [85]. Finally, the robustness of the topological magnetic field lines to the motion of the particles is not a physically relevant question for the model considered in Chapter 5, as the 'particles' of the system are neutrally charged. However, the stability of these topological magnetic field lines is an interesting question when there are charged particles present and is linked to the field of magnetohydrodynamics [278, 279]. Two examples or relevant settings in magnetohydrodynamics are that of solar physics where flares can be ejected due to the dynamics of magnetic fields [280, 281] and in the possible design of stable thermonuclear fusion reactors where topological magnetic fields could be used to trap the plasma [282]. While the method of Chapter 5 is not currently capable of studying the interaction of the topological magnetic field with charged particles, and the link between this and magnetohydrodynamics, it is a step in this direction for cold gases.

In this thesis, we have characterised the robustness of topological states of matter against impurities and interactions. In the process of considering topological insulators, we have derived the exact analytical wave functions of non-interacting low-dimensional general lattice models and discovered special points where the dynamics of classical and quantum driven models are equivalent. We have also shown that new forms of topology can be realised, with the generation of linked and knotted synthetic magnetic fields by using light-atom interactions. In conclusion, we have investigated topological states of matter in and out of crystalline systems, with a focus on their robustness and their realisation or application to the settings of ultracold atoms and photonic lattices.

Bibliography

[1] M. H. Anderson, J. R. Ensher, M. R. Matthews, C. E. Wieman, and E. A. Cornell, Science **269**, 198 (1995).

[2] K. B. Davis, M. O. Mewes, M. R. Andrews, N. J. van Druten, D. S. Durfee, D. M. Kurn, and W. Ketterle, Phys. Rev. Lett. **75**, 3969 (1995).

[3] C. C. Bradley, C. A. Sackett, J. J. Tollett, and R. G. Hulet, Phys. Rev. Lett. **75**, 1687 (1995).

[4] B. DeMarco and D. S. Jin, Science **285**, 1703 (1999).

[5] T. Lahaye, C. Menotti, L. Santos, M. Lewenstein, and T. Pfau, Rep. Prog. Phys. **72**, 126401 (2009).

[6] C. Trefzger, C. Menotti, B. Capogrosso-Sansone, and M. Lewenstein, J. Phys. B: At. Mol. Opt. **44**, 193001 (2011).

[7] L. D. Carr, D. DeMille, R. V. Krems, and J. Ye, New J. Phys. **11**, 055049 (2009).

[8] T. M. Rvachov, H. Son, A. T. Sommer, S. Ebadi, J. J. Park, M. W. Zwierlein, W. Ketterle, and A. O. Jamison, Phys. Rev. Lett. **119**, 143001 (2017).

[9] C. J. Pethick and H. Smith, *Bose–Einstein condensation in dilute gases* (Cambridge university press, 2008).

[10] M. Lewenstein, A. Sanpera, and V. Ahufinger, *Ultracold Atoms in Optical Lattices: Simulating quantum many-body systems* (Oxford University Press, 2012).

[11] I. Bloch, Nat. Phys. **1**, 23 (2005).

[12] S. Giorgini, L. P. Pitaevskii, and S. Stringari, Rev. Mod. Phys. **80**, 1215 (2008).

[13] I. Bloch, J. Dalibard, and W. Zwerger, Rev. Mod. Phys. **80**, 885 (2008).

[14] I. Bloch, J. Dalibard, and S. Nascimbene, Nat. Phys. **8**, 267 (2012).

[15] L. Pitaevskii and S. Stringari, *Bose-Einstein condensation* (Oxford University Press, 2003).

[16] A. L. Fetter and J. D. Walecka, *Quantum theory of many-particle systems* (Courier Corporation, 2003).

[17] D. Jaksch, C. Bruder, J. I. Cirac, C. W. Gardiner, and P. Zoller, Phys. Rev. Lett. **81**, 3108 (1998).

[18] M. P. A. Fisher, P. B. Weichman, G. Grinstein, and D. S. Fisher, Phys. Rev. B **40**, 546 (1989).

[19] M. Greiner, O. Mandel, T. Esslinger, T. W. Hänsch, and I. Bloch, Nature **415**, 39 (2002).

[20] O. Dutta, M. Gajda, P. Hauke, M. Lewenstein, D.-S. Lühmann, B. A. Malomed, T. Sowiński, and J. Zakrzewski, Rep. Prog. Phys. **78**, 066001 (2015).

[21] T. Sowiński, O. Dutta, P. Hauke, L. Tagliacozzo, and M. Lewenstein, Phys. Rev. Lett. **108**, 115301 (2012).

[22] D. Rossini and R. Fazio, New J. Phys. **14**, 065012 (2012).

[23] T. Ohgoe, T. Suzuki, and N. Kawashima, Phys. Rev. B **86**, 054520 (2012).

[24] M. Maik, P. Hauke, O. Dutta, M. Lewenstein, and J. Zakrzewski, New J. Phys. **15**, 113041 (2013).

[25] H. Mosadeq and R. Asgari, Phys. Rev. B **91**, 085126 (2015).

[26] K. Kawaki, Y. Kuno, and I. Ichinose, Phys. Rev. B **95**, 195101 (2017).

[27] D. Johnstone, N. Westerberg, C. W. Duncan, and P. Öhberg, arXiv preprint arXiv:1905.00027 (2019).

[28] D. Johnstone, P. Öhberg, and C. W. Duncan, arXiv preprint arXiv:1904.12870 (2019).

[29] D. Petrov, D. Gangardt, and G. Shlyapnikov, in *Journal de Physique IV (Proceedings)*, Vol. 116 (EDP sciences, 2004) pp. 5–44.

[30] P. O. Fedichev, Y. Kagan, G. V. Shlyapnikov, and J. T. M. Walraven, Phys. Rev. Lett. **77**, 2913 (1996).

[31] M. Theis, G. Thalhammer, K. Winkler, M. Hellwig, G. Ruff, R. Grimm, and J. H. Denschlag, Phys. Rev. Lett. **93**, 123001 (2004).

[32] C. Menotti, M. Lewenstein, T. Lahaye, and T. Pfau, AIP Conf. Proc. **970**, 332 (2008).

[33] S. F. Caballero-Benitez and I. B. Mekhov, New J. Phys. **18**, 113010 (2016).

[34] N. Dogra, F. Brennecke, S. D. Huber, and T. Donner, Phys. Rev. A **94**, 023632 (2016).

[35] A. E. Niederle, G. Morigi, and H. Rieger, Phys. Rev. A **94**, 033607 (2016).

[36] T. Flottat, L. d. F. de Parny, F. Hébert, V. G. Rousseau, and G. G. Batrouni, Phys. Rev. B **95**, 144501 (2017).

[37] O. Morsch and M. Oberthaler, Rev. Mod. Phys. **78**, 179 (2006).

[38] Q. Beaufils, G. Tackmann, X. Wang, B. Pelle, S. Pelisson, P. Wolf, and F. P. dos Santos, Phys. Rev. Lett. **106**, 213002 (2011).

[39] H. Miyake, G. A. Siviloglou, C. J. Kennedy, W. C. Burton, and W. Ketterle, Phys. Rev. Lett. **111**, 185302 (2013).

[40] D.-W. Zhang, Y.-Q. Zhu, Y. X. Zhao, H. Yan, and S.-L. Zhu, Adv. Phys. **67**, 253 (2018).

[41] N. R. Cooper, J. Dalibard, and I. B. Spielman, Rev. Mod. Phys. **91**, 015005 (2019).

[42] J. Liang, X. Liu, and Y. Duan, Europhys. Lett. **86**, 10008 (2009).

[43] Y.-K. Liu and S.-J. Yang, Phys. Rev. A **87**, 063632 (2013).

[44] Y.-K. Liu, S. Feng, and S.-J. Yang, Europhys. Lett. **106**, 50005 (2014).

[45] D. Proment, M. Onorato, and C. F. Barenghi, J. Phy.: Conf. Ser. **544**, 012022 (2014).

[46] Y. M. Bidasyuk, A. V. Chumachenko, O. O. Prikhodko, S. I. Vilchinskii, M. Weyrauch, and A. I. Yakimenko, Phys. Rev. A **92**, 053603 (2015).

[47] Y. Kawaguchi, M. Nitta, and M. Ueda, Phys. Rev. Lett. **100**, 180403 (2008).

[48] D. S. Hall, M. W. Ray, K. Tiurev, E. Ruokokoski, A. H. Gheorghe, and M. Möttönen, Nat. Phys. **12**, 478 (2016).

[49] R. Shankar, Journal de Physique **38**, 1405 (1977).

[50] W. Lee, A. H. Gheorghe, K. Tiurev, T. Ollikainen, M. Möttönen, and D. S. Hall, Sci. Adv. **4**, eaao3820 (2018).

[51] J. Ruostekoski and Z. Dutton, Phys. Rev. A **72**, 063626 (2005).

[52] F. Maucher, S. A. Gardiner, and I. G. Hughes, New J. Phys. **18**, 063016 (2016).

[53] E. Fradkin, *Field theories of condensed matter physics* (Cambridge University Press, 2013).

[54] H. L. Stormer, D. C. Tsui, and A. C. Gossard, Rev. Mod. Phys. **71**, S298 (1999).

[55] J. Dalibard, F. Gerbier, G. Juzeliūnas, and P. Öhberg, Rev. Mod. Phys. **83**, 1523 (2011).

[56] N. Goldman, G. Juzeliūnas, P. Öhberg, and I. B. Spielman, Rep. Prog. Phys. **77**, 126401 (2014).

[57] D. Jaksch and P. Zoller, New J. Phys. **5**, 56 (2003).

[58] K. Osterloh, M. Baig, L. Santos, P. Zoller, and M. Lewenstein, Phys. Rev. Lett. **95**, 010403 (2005).

[59] N. Goldman and J. Dalibard, Phys. Rev. X **4**, 031027 (2014).

[60] P. Hauke, O. Tieleman, A. Celi, C. Ölschläger, J. Simonet, J. Struck, M. Weinberg, P. Windpassinger, K. Sengstock, M. Lewenstein, and A. Eckardt, Phys. Rev. Lett. **109**, 145301 (2012).

[61] M. Aidelsburger, M. Atala, S. Nascimbène, S. Trotzky, Y.-A. Chen, and I. Bloch, Phys. Rev. Lett. **107**, 255301 (2011).

[62] K. Jiménez-García, L. J. LeBlanc, R. A. Williams, M. C. Beeler, A. R. Perry, and I. B. Spielman, Phys. Rev. Lett. **108**, 225303 (2012).

[63] J. Struck, C. Ölschläger, M. Weinberg, P. Hauke, J. Simonet, A. Eckardt, M. Lewenstein, K. Sengstock, and P. Windpassinger, Phys. Rev. Lett. **108**, 225304 (2012).

[64] M. Aidelsburger, M. Atala, M. Lohse, J. T. Barreiro, B. Paredes, and I. Bloch, Phys. Rev. Lett. **111**, 185301 (2013).

[65] K. W. Madison, F. Chevy, W. Wohlleben, and J. Dalibard, Phys. Rev. Lett. **84**, 806 (2000).

[66] J. Abo-Shaeer, C. Raman, J. Vogels, and W. Ketterle, Science **292**, 476 (2001).

[67] R. Dum and M. Olshanii, Phys. Rev. Lett. **76**, 1788 (1996).

[68] P. M. Visser and G. Nienhuis, Phys. Rev. A **57**, 4581 (1998).

[69] G. Juzeliūnas and P. Öhberg, Phys. Rev. Lett. **93**, 033602 (2004).

[70] G. Juzeliūnas, P. Öhberg, J. Ruseckas, and A. Klein, Phys. Rev. A **71**, 053614 (2005).

[71] G. Juzeliūnas, J. Ruseckas, P. Öhberg, and M. Fleischhauer, Phys. Rev. A **73**, 025602 (2006).

[72] J. Ruseckas, G. Juzeliūnas, P. Öhberg, and M. Fleischhauer, Phys. Rev. Lett. **95**, 010404 (2005).

[73] K. J. Günter, M. Cheneau, T. Yefsah, S. P. Rath, and J. Dalibard, Phys. Rev. A **79**, 011604 (2009).

[74] Y.-J. Lin, R. L. Compton, K. Jimenez-Garcia, J. V. Porto, and I. B. Spielman, Nature **462**, 628 (2009).

[75] Y.-J. Lin, R. L. Compton, A. R. Perry, W. D. Phillips, J. V. Porto, and I. B. Spielman, Phys. Rev. Lett. **102**, 130401 (2009).

[76] L. D. Landau and E. M. Lifshitz, *Quantum mechanics: non-relativistic theory (Course of theoretical physics Vol. 3)*, 1st ed. (Addison-Wesley publishing company, 1958).

[77] P. A. M. Dirac, *The principles of quantum mechanics*, 4th ed., 27 (Oxford university press, 1958).

[78] B. d'Espagnat, *Conceptual foundations of quantum mechanics*, 2nd ed. (Addison-Wiley Publishing Company, 1989).

[79] F. Williams, *Topics in quantum mechanics*, Vol. 27 (Birkhäuser Boston, 2012).

[80] S. Weinberg, *Lectures on quantum mechanics*, 2nd ed. (Cambridge University Press, 2015).

[81] A. Stern, Ann. Phys. **323**, 204 (2008).

[82] C. Nayak, S. H. Simon, A. Stern, M. Freedman, and S. Das Sarma, Rev. Mod. Phys. **80**, 1083 (2008).

[83] A. E. B. Nielsen, Phys. Rev. B **91**, 041106 (2015).

[84] T. H. Hansson, M. Hermanns, S. H. Simon, and S. F. Viefers, Rev. Mod. Phys. **89**, 025005 (2017).

[85] V. Lahtinen and J. Pachos, SciPost Physics **3**, 021 (2017).

[86] S. Weinberg, *The quantum theory of fields. Vol. 1: Foundations* (Cambridge University Press, 1995).

[87] E. P. Gross, Il Nuovo Cimento (1955-1965) **20**, 454 (1961).

[88] L. Pitaevskii, Sov. Phys. JETP **13**, 451 (1961).

[89] R. Grimm, M. Weidemüller, and Y. B. Ovchinnikov, in *Advances In Atomic, Molecular, and Optical Physics*, Vol. 42, edited by B. Bederson and H. Walther (Academic Press, 2000) pp. 95 – 170.

[90] M. V. Cifuentes, *Few quantum particles on one dimensional lattices*, Ph.D. thesis, Humboldt-Universität zu Berlin, Mathematisch-Naturwissenschaftliche Fakultät I (2010).

[91] H. M. Rosenberg, *The Solid State*, 3rd ed. (Oxford University Press, 1992).

[92] S. H. Simon, *The Oxford solid state basics* (Oxford University Press, 2013).

[93] D. Jaksch and P. Zoller, Ann. Phys. **315**, 52 (2005).

[94] N. Marzari, A. A. Mostofi, J. R. Yates, I. Souza, and D. Vanderbilt, Rev. Mod. Phys. **84**, 1419 (2012).

[95] A. Eckardt, Rev. Mod. Phys. **89**, 011004 (2017).

[96] A. Bermudez, T. Schaetz, and D. Porras, Phys. Rev. Lett. **107**, 150501 (2011).

[97] C. E. Creffield, G. Pieplow, F. Sols, and N. Goldman, New J. Phys. **18**, 093013 (2016).

[98] A. Gómez-León and G. Platero, Phys. Rev. Lett. **110**, 200403 (2013).

[99] M. Aidelsburger, M. Lohse, C. Schweizer, M. Atala, J. T. Barreiro, S. Nascimbene, N. Cooper, I. Bloch, and N. Goldman, Nat. Phys. **11**, 162 (2015).

[100] D. V. Else and C. Nayak, Phys. Rev. B **93**, 201103 (2016).

[101] R. Roy and F. Harper, Phys. Rev. B **96**, 155118 (2017).

[102] K. Plekhanov, G. Roux, and K. Le Hur, Phys. Rev. B **95**, 045102 (2017).

[103] Z. Xu, Y. Zhang, and S. Chen, Phys. Rev. A **96**, 013606 (2017).

[104] O. Shtanko and R. Movassagh, Phys. Rev. Lett. **121**, 126803 (2018).

[105] M. Aidelsburger, *Artificial gauge fields with ultracold atoms in optical lattices* (Springer, 2015).

[106] A. Eckardt and E. Anisimovas, New J. Phys. **17**, 093039 (2015).

[107] M. Bukov, M. Heyl, D. A. Huse, and A. Polkovnikov, Phys. Rev. B **93**, 155132 (2016).

[108] M. Reitter, J. Näger, K. Wintersperger, C. Sträter, I. Bloch, A. Eckardt, and U. Schneider, Phys. Rev. Lett. **119**, 200402 (2017).

[109] A. S. Schwarz, *Topology for physicists*, Vol. 308 (Springer-Verlag Berin Heidelberg, 1996).

[110] V. Guillemin and A. Pollack, *Differential topology* (Prentice-Hall, Inc., Englewood Cliffs, New Jersey, 1974).

[111] B. A. Bernevig and T. L. Hughes, *Topological insulators and topological superconductors* (Princeton university press, 2013).

[112] K. von Klitzing, G. Dorda, and M. Pepper, Phys. Rev. Lett. **45**, 494 (1980).

[113] D. J. Thouless, M. Kohmoto, M. P. Nightingale, and M. den Nijs, Phys. Rev. Lett. **49**, 405 (1982).

[114] B. I. Halperin, Phys. Rev. B **25**, 2185 (1982).

[115] A. H. MacDonald and P. Středa, Phys. Rev. B **29**, 1616 (1984).

[116] Y. Hatsugai, Phys. Rev. Lett. **71**, 3697 (1993).

[117] M. Z. Hasan and C. L. Kane, Rev. Mod. Phys. **82**, 3045 (2010).

[118] M. V. Berry, P. Roy. Soc. Lond. A Mat. **392**, 45 (1984).

[119] D. Xiao, M.-C. Chang, and Q. Niu, Rev. Mod. Phys. **82**, 1959 (2010).

[120] J. K. Asbóth, L. Oroszlány, and A. Pályi, *A Short Course on Topological Insulators*, Vol. 919 (Springer, 2016).

[121] G. Juzeliūnas and I. Spielman, Physics **4**, 99 (2011).

[122] L. D. Landau and E. M. Lifshitz, *The classical theory of fields (Course of theoretical physics Vol. 2)*, 1st ed. (Addison-Wesley publishing company, 1951).

[123] D. Husemoller, *Fibre bundles*, 3rd ed., Vol. 5 (Springer-Verlag, 1994).

[124] M. Fruchart and D. Carpentier, Comptes Rendus Physique **14**, 779 (2013).

[125] R. S. K. Mong and V. Shivamoggi, Phys. Rev. B **83**, 125109 (2011).

[126] L. Fidkowski, T. S. Jackson, and I. Klich, Phys. Rev. Lett. **107**, 036601 (2011).

[127] T. Fukui, K. Shiozaki, T. Fujiwara, and S. Fujimoto, J. Phys. Soc. Jpn. **81**, 114602 (2012).

[128] M. G. Silveirinha, Phys. Rev. X **9**, 011037 (2019).

[129] J. Zak, Phys. Rev. Lett. **62**, 2747 (1989).

[130] P. Delplace, D. Ullmo, and G. Montambaux, Phys. Rev. B **84**, 195452 (2011).

[131] P. R. Cromwell, *Knots and links* (Cambridge university press, 2004).

[132] C. Livingston, *Knot theory*, Vol. 24 (The mathematical association of america, 1993).

[133] C. M. Gordon, in *Knot theory* (Springer, 1978) pp. 1–60.

[134] W. Thomson, Philos. Mag. **34**, 15 (1867).

[135] P. G. Tait, *Scientific papers*, Vol. 2 (Cambridge university press, 1900).

[136] T. P. Kirkman and P. G. Tait, Proc. R. Soc. Edinb. **12**, 646 (1884).

[137] J. W. Alexander and G. B. Briggs, Ann. Math. , 562 (1926).

[138] J. W. Alexander, Trans. Am. Math. Soc. **30**, 275 (1928).

[139] J. W. Milnor, Ann. Math. , 248 (1950).

[140] K. A. Perko, P. Am. Math. Soc. **45**, 262 (1974).

[141] L. H. Kauffman, Am. Math. Mon **95**, 195 (1988).

[142] J. Hoste, M. Thistlethwaite, and J. Weeks, Math. Intell. **20**, 33 (1998).

[143] L. H. Kauffman and S. Lambropoulou, arXiv preprint math/0212011 (2002).

[144] H. K. Moffatt, J. Fluid Mech. **35**, 117 (1969).

[145] H. Moffatt and A. Tsinober, Annu. Rev. Fluid Mech. **24**, 281 (1992).

[146] D. Kleckner and W. T. Irvine, Nat. Phys. **9**, 253 (2013).

[147] A. Enciso and D. Peralta-Salas, Proc. IUTAM **7**, 13 (2013).

[148] M. W. Scheeler, D. Kleckner, D. Proment, G. L. Kindlmann, and W. T. M. Irvine, Proc. Natl. Acad. Sci. USA **111**, 15350 (2014).

[149] R. A. Battye and P. M. Sutcliffe, Phys. Rev. Lett. **81**, 4798 (1998).

[150] P. Sutcliffe, in *P. Roy. Soc. Lon. A: Math.*, Vol. 463 (The Royal Society, 2007) pp. 3001–3020.

[151] S. Chandrasekhar and L. Woltjer, Proc. Natl. Acad. Sci. USA **44**, 285 (1958).

[152] M. A. Berger, Plasma Phys. Contr. F. **41**, B167 (1999).

[153] A. Thompson, J. Swearngin, A. Wickes, and D. Bouwmeester, Phys. Rev. E **89**, 043104 (2014).

[154] P. Sutcliffe, Phys. Rev. Lett. **118**, 247203 (2017).

[155] U. Tkalec, M. Ravnik, S. Čopar, S. Žumer, and I. Muševič, Science **333**, 62 (2011).

[156] W. R. Taylor, Nature **406**, 916 (2000).

[157] A. Suma and C. Micheletti, Proc. Natl. Acad. Sci. USA , 201701321 (2017).

[158] W. T. Irvine and D. Bouwmeester, Nat. Phys. **4**, 716 (2008).

[159] W. T. Irvine, J. Phys. A: Math. Theor. **43**, 385203 (2010).

[160] H. Kedia, I. Bialynicki-Birula, D. Peralta-Salas, and W. T. M. Irvine, Phys. Rev. Lett. **111**, 150404 (2013).

[161] H. Kedia, D. Peralta-Salas, and W. T. M. Irvine, J. Phys. A: Math. Theor. **51**, 025204 (2018).

[162] H. Kedia, D. Foster, M. R. Dennis, and W. T. Irvine, Phys. Rev. Lett. **117**, 274501 (2016).

[163] D. Kleckner, L. H. Kauffman, and W. T. Irvine, Nat. Phys. **12**, 650 (2016).

[164] D. Hügel and B. Paredes, Phys. Rev. A **89**, 023619 (2014).

[165] M. König, H. Buhmann, L. W. Molenkamp, T. Hughes, C.-X. Liu, X.-L. Qi, and S.-C. Zhang, J. Phys. Soc. Jpn. **77**, 031007 (2008).

[166] S. Mao, Y. Kuramoto, K.-I. Imura, and A. Yamakage, J. Phys. Soc. Jpn. **79**, 124709 (2010).

[167] S. Mao, A. Yamakage, and Y. Kuramoto, Phys. Rev. B **84**, 115413 (2011).

[168] F. K. Kunst, M. Trescher, and E. J. Bergholtz, Phys. Rev. B **96**, 085443 (2017).

[169] F. K. Kunst, G. van Miert, and E. J. Bergholtz, Phys. Rev. B **97**, 241405 (2018).

[170] Y. Hatsugai, T. Fukui, and H. Aoki, Phys. Rev. B **74**, 205414 (2006).

[171] W. P. Su, J. R. Schrieffer, and A. J. Heeger, Phys. Rev. Lett. **42**, 1698 (1979).

[172] F. Grusdt, M. Höning, and M. Fleischhauer, Phys. Rev. Lett. **110**, 260405 (2013).

[173] L. Li, Z. Xu, and S. Chen, Phys. Rev. B **89**, 085111 (2014).

[174] Z. Yan and S. Wan, Europhys. Lett **107**, 47007 (2014).

[175] B. Zhu, R. Lü, and S. Chen, Phys. Rev. A **89**, 062102 (2014).

[176] M. Di Liberto, A. Recati, I. Carusotto, and C. Menotti, Phys. Rev. A **94**, 062704 (2016).

[177] S. Lieu, Phys. Rev. B **97**, 045106 (2018).

[178] E. J. Meier, F. A. An, and B. Gadway, Nat. Comm. **7**, 13986 (2016).

[179] M. J. Rice and E. J. Mele, Phys. Rev. Lett. **49**, 1455 (1982).

[180] P. G. Harper, Proc. Phys. Soc. A **68**, 879 (1955).

[181] M. Atala, M. Aidelsburger, J. T. Barreiro, D. Abanin, T. Kitagawa, E. Demler, and I. Bloch, Nat. Phys. **9**, 795 (2013).

[182] J.-W. Rhim, J. Behrends, and J. H. Bardarson, Phys. Rev. B **95**, 035421 (2017).

[183] M. Ezawa, Y. Tanaka, and N. Nagaosa, Sci. Rep. **3**, 2790 (2013).

[184] M. Valiente and D. Petrosyan, Europhys. Lett. **83**, 30007 (2008).

[185] M. Valiente and D. Petrosyan, J. Phys. B: At. Mol. Opt. **42**, 121001 (2009).

[186] M. Valiente, Phys. Rev. A **81**, 042102 (2010).

[187] A. Bansil, H. Lin, and T. Das, Rev. Mod. Phys. **88**, 021004 (2016).

[188] W. Shockley, Phys. Rev. **56**, 317 (1939).

[189] Y. Lahini, R. Pugatch, F. Pozzi, M. Sorel, R. Morandotti, N. Davidson, and Y. Silberberg, Phys. Rev. Lett. **103**, 013901 (2009).

[190] Y. E. Kraus, Y. Lahini, Z. Ringel, M. Verbin, and O. Zilberberg, Phys. Rev. Lett. **109**, 106402 (2012).

[191] M. Schreiber, S. S. Hodgman, P. Bordia, H. P. Lüschen, M. H. Fischer, R. Vosk, E. Altman, U. Schneider, and I. Bloch, Science **349**, 842 (2015).

[192] F. Mei, S.-L. Zhu, Z.-M. Zhang, C. H. Oh, and N. Goldman, Phys. Rev. A **85**, 013638 (2012).

[193] N. Goldman, N. Cooper, and J. Dalibard, in *Universal Themes of Bose-Einstein Condensation*, edited by N. P. Proukakis, D. W. Snoke, and P. B. Littlewood (Cambridge University Press, 2017) Chap. 14.

[194] J. R. Rubbmark, M. M. Kash, M. G. Littman, and D. Kleppner, Phys. Rev. A **23**, 3107 (1981).

[195] D. R. Hofstadter, Phys. Rev. B **14**, 2239 (1976).

[196] C. J. Kennedy, W. C. Burton, W. C. Chung, and W. Ketterle, Nat. Phys. **11**, 859 (2015).

[197] M. Hafezi, A. S. Sørensen, E. Demler, and M. D. Lukin, Phys. Rev. A **76**, 023613 (2007).

[198] M. S. Rudner, N. H. Lindner, E. Berg, and M. Levin, Phys. Rev. X **3**, 031005 (2013).

[199] P. Ponte, Z. Papić, F. Huveneers, and D. A. Abanin, Phys. Rev. Lett. **114**, 140401 (2015).

[200] P. Ponte, A. Chandran, Z. Papić, and D. A. Abanin, Ann. Phys. **353**, 196 (2015).

[201] Y. Lumer, M. C. Rechtsman, Y. Plotnik, and M. Segev, Phys. Rev. A **94**, 021801 (2016).

[202] C. Angstmann, I. Donnelly, B. Henry, and J. Nichols, J. Comput. Phys. **293**, 53 (2015).

[203] J. K. Asboth and J. M. Edge, Phys. Rev. A **91**, 022324 (2015).

[204] M. Genske, W. Alt, A. Steffen, A. H. Werner, R. F. Werner, D. Meschede, and A. Alberti, Phys. Rev. Lett. **110**, 190601 (2013).

[205] T. Kitagawa, A. Broome, M. A. ans Fedrizzi, M. S. Rudner, E. Berg, I. Kassal, A. Aspuru-Guzik, D. E., and A. G. White, Nat. Comm. **3**, 882 (2012).

[206] A. M. Childs, E. Farhi, and S. Gutmann, Quantum Inf. Process. **1**, 35 (2002).

[207] S. Boettcher, S. Falkner, and R. Portugal, Phys. Rev. A **91**, 052330 (2015).

[208] T. Kitagawa, E. Berg, M. Rudner, and E. Demler, Phys. Rev. B **82**, 235114 (2010).

[209] J. K. Asbóth and H. Obuse, Phys. Rev. B **88**, 121406 (2013).

[210] S. Mugel, A. Celi, P. Massignan, J. K. Asbóth, M. Lewenstein, and C. Lobo, Phys. Rev. A **94**, 023631 (2016).

[211] X. Wang, L. Xiao, X. Qiu, K. Wang, W. Yi, and P. Xue, Phys. Rev. A **98**, 013835 (2018).

[212] V. Kendon and B. Tregenna, Phys. Rev. A **67**, 042315 (2003).

[213] J. D. Whitfield, C. A. Rodríguez-Rosario, and A. Aspuru-Guzik, Phys. Rev. A **81**, 022323 (2010).

[214] P. M. Preiss, R. Ma, M. E. Tai, A. Lukin, M. Rispoli, P. Zupancic, Y. Lahini, R. Islam, and M. Greiner, Science **347**, 1229 (2015).

[215] M. A. Broome, A. Fedrizzi, B. P. Lanyon, I. Kassal, A. Aspuru-Guzik, and A. G. White, Phys. Rev. Lett. **104**, 153602 (2010).

[216] T. A. Brun, H. A. Carteret, and A. Ambainis, Phys. Rev. Lett. **91**, 130602 (2003).

[217] A. C. Oliveira, R. Portugal, and R. Donangelo, Phys. Rev. A **74**, 012312 (2006).

[218] J. Košík, V. Bužek, and M. Hillery, Phys. Rev. A **74**, 022310 (2006).

[219] C. W. Duncan, P. Öhberg, and M. Valiente, Phys. Rev. B **95**, 125104 (2017).

[220] S. Mukherjee, A. Spracklen, M. Valiente, E. Andersson, P. Öhberg, N. Goldman, and R. R. Thomson, Nat. Comm. **8**, 13918 (2017).

[221] L. J. Maczewsky, J. M. Zeuner, S. Nolte, and A. Szameit, Nat. Comm. **8**, 13756 (2017).

[222] M. D. Reichl and E. J. Mueller, Phys. Rev. A **89**, 063628 (2014).

[223] M. Atala, A. M, M. Lohse, J. Barreiro, B. Peredes, and I. Bloch, Nat. Phys. **10**, 588 (2014).

[224] S. Keßler and F. Marquardt, Phys. Rev. A **89**, 061601 (2014).

[225] D. Chowdhury, L. Santen, and A. Schadschneider, Phys. Rep. **329**, 199 (2000).

[226] A. Schadschneider, Physica A **313**, 153 (2002).

[227] S. Maerivoet and B. D. Moor, Phys. Rep. **419**, 1 (2005).

[228] K. Nagel, Phys. Rev. E **53**, 4655 (1996).

[229] A. Schadschneider, Eur. Phys. J. B **10**, 573 (1999).

[230] Kai Nagel and Michael Schreckenberg, J. Phys. I France **2**, 2221 (1992).

[231] H. Obuse and N. Kawakami, Phys. Rev. B **84**, 195139 (2011).

[232] S. Mukherjee, H. K. Chandrasekharan, P. Öhberg, N. Goldman, and R. R. Thomson, Nat. Comm. **9**, 4209 (2018).

[233] M. Girardeau, J. Math. Phys. **1**, 516 (1960).

[234] F. Crépin, N. Laflorencie, G. Roux, and P. Simon, Phys. Rev. B **84**, 054517 (2011).

[235] M. Rigol and A. Muramatsu, Phys. Rev. Lett. **94**, 240403 (2005).

[236] E. Babaev, L. D. Faddeev, and A. J. Niemi, Phys. Rev. B **65**, 100512 (2002).

[237] E. Babaev, Phys. Rev. Lett. **88**, 177002 (2002).

[238] E. Babaev, Phys. Rev. D **70**, 043001 (2004).

[239] F. N. Rybakov, J. Garaud, and E. Babaev, arXiv preprint arXiv:1807.02509 (2018).

[240] N. Read and D. Green, Phys. Rev. B **61**, 10267 (2000).

[241] S. Das Sarma, C. Nayak, and S. Tewari, Phys. Rev. B **73**, 220502 (2006).

[242] C. W. Duncan, C. Ross, N. Westerberg, M. Valiente, B. J. Schroers, and P. Öhberg, Phys. Rev. A **99**, 063613 (2019).

[243] Y.-J. Lin, R. L. Compton, A. R. Perry, W. D. Phillips, J. V. Porto, and I. B. Spielman, Phys. Rev. Lett. **102**, 130401 (2009).

[244] Y.-J. Lin, R. L. Compton, K. Jimenez-Garcia, W. D. Phillips, J. V. Porto, and I. B. Spielman, Nat. Phys. **7**, 531 (2011).

[245] S.-L. Zhu, H. Fu, C.-J. Wu, S.-C. Zhang, and L.-M. Duan, Phys. Rev. Lett. **97**, 240401 (2006).

[246] M. Born and R. Oppenheimer, Ann. Phys. (Berl.) **389**, 457 (1927).

[247] C. A. Mead, Rev. Mod. Phys. **64**, 51 (1992).

[248] F. Wilczek and A. Shapere, *Geometric phases in physics*, Vol. 5 (World Scientific, 1989).

[249] C. W. Duncan and A. del Campo, New J. Phys. **20**, 085003 (2018).

[250] A. F. Rañada, Lett. Math. Phys. **18**, 97 (1989).

[251] A. F. Ranada, J. Phy. A: Math. Gen. **23**, L815 (1990).

[252] R. Bott and L. W. Tu, *Differential forms in algebraic topology*, Vol. 82 (Springer Science & Business Media, 2013).

[253] H. Flanders, *Differential Forms with Applications to the Phscial Sciences* (Dover Publications, Inc. New York, 1989).

[254] T. Frankel, *The geometry of physics: an introduction* (Cambridge university press, 2001).

[255] I. M. Besieris and A. M. Shaarawi, Opt. Lett. **34**, 3887 (2009).

[256] H. Hopf, in *Selecta Heinz Hopf* (Springer, 1964) pp. 38–63.

[257] C. Ross and B. J. Schroers, Lett. Math. Phys **108**, 949 (2018).

[258] M. R. Dennis, R. P. King, B. Jack, K. O'Holleran, and M. J. Padgett, Nat. Phys. **6**, 118 (2010).

[259] J. Romero, J. Leach, B. Jack, M. R. Dennis, S. Franke-Arnold, S. M. Barnett, and M. J. Padgett, Phys. Rev. Lett. **106**, 100407 (2011).

[260] M. J. Padgett, K. O'Holleran, R. P. King, and M. R. Dennis, Contemp. Phys. **52**, 265 (2011).

[261] D. McGloin, G. Spalding, H. Melville, W. Sibbett, and K. Dholakia, Opt. Express **11**, 158 (2003).

[262] S. Bergamini, B. Darquié, M. Jones, L. Jacubowiez, A. Browaeys, and P. Grangier, J. Opt. Soc. Am. B **21**, 1889 (2004).

[263] V. Boyer, R. Godun, G. Smirne, D. Cassettari, C. Chandrashekar, A. Deb, Z. Laczik, and C. Foot, Phys. Rev. A **73**, 031402 (2006).

[264] S. E. Olson, M. L. Terraciano, M. Bashkansky, and F. K. Fatemi, Phys. Rev. A **76**, 061404 (2007).

[265] A. L. Gaunt, T. F. Schmidutz, I. Gotlibovych, R. P. Smith, and Z. Hadzibabic, Phys. Rev. Lett. **110**, 200406 (2013).

[266] F. Nogrette, H. Labuhn, S. Ravets, D. Barredo, L. Béguin, A. Vernier, T. Lahaye, and A. Browaeys, Phys. Rev. X **4**, 021034 (2014).

[267] R. M. W. van Bijnen, C. Ravensbergen, D. J. Bakker, G. J. Dijk, S. J. J. M. F. Kokkelmans, and E. J. D. Vredenbregt, New J. Phys. **17**, 023045 (2015).

[268] L. Allen, M. W. Beijersbergen, R. J. C. Spreeuw, and J. P. Woerdman, Phys. Rev. A **45**, 8185 (1992).

[269] A. Jaouadi, N. Gaaloul, B. Viaris de Lesegno, M. Telmini, L. Pruvost, and E. Charron, Phys. Rev. A **82**, 023613 (2010).

[270] J. Leach, M. R. Dennis, J. Courtial, and M. J. Padgett, New J. Phys. **7**, 55 (2005).

[271] T. Roger, C. Maitland, K. Wilson, N. Westerberg, D. Vocke, E. M. Wright, and D. Faccio, Nat. Comm. **7**, 13492 (2016).

[272] L. Caspani, R. P. M. Kaipurath, M. Clerici, M. Ferrera, T. Roger, J. Kim, N. Kinsey, M. Pietrzyk, A. Di Falco, V. M. Shalaev, A. Boltasseva, and D. Faccio, Phys. Rev. Lett. **116**, 233901 (2016).

[273] M. L. Chiofalo, S. Succi, and M. P. Tosi, Phys. Rev. E **62**, 7438 (2000).

[274] A. K. Roy, N. Gupta, and B. M. Deb, Phys. Rev. A **65**, 012109 (2001).

[275] P. Bader, S. Blanes, and F. Casas, J. Chem. Phys. **139**, 124117 (2013).

[276] D. L. Goldsmith, Michigan Math. J. **28**, 3 (1981).

[277] C. Aneziris, A. Balachandran, L. Kauffman, and A. Srivastava, Int. J. Mod. Phys. A **06**, 2519 (1991).

[278] H. K. Moffatt, P. Natl. Acad. Sci. USA **111**, 3663 (2014).

[279] C. B. Smiet, S. Candelaresi, A. Thompson, J. Swearngin, J. W. Dalhuisen, and D. Bouwmeester, Phys. Rev. Lett. **115**, 095001 (2015).

[280] B. C. Low, J. Geophys. Res. **106**, 25141 (2001).

[281] S. Candelaresi and A. Brandenburg, Proceedings of the International Astronomical Union **8**, 353 (2012).

[282] T. R. Jarboe, Plasma Physics and Controlled Fusion **36**, 945 (1994).